DELIVERY OF THERAPEUTIC PROTEINS TO THE BRAIN

Dongfen Yuan

A dissertation submitted to the faculty at the University of North Carolina at Chapel Hill in partial fulfillment of the requirements for the degree of Doctor of Philosophy in the Division of Pharmacoengineering and Molecular Pharmaceutics in the UNC Eshelman School of Pharmacy.

Chapel Hill
2017

Approved by:

Alexander V. Kabanov

Shawn Hingtgen

Elena Batrakova

Zhen Gu

William A. Banks

ABSTRACT
Dongfen Yuan: Delivery of Therapeutic Proteins to the Brain
(Under the direction of Alexander V. Kabanov)

Protein therapeutics have tremendous potentials to treat disorders in central nervous system (CNS). However, delivery of therapeutic dose of proteins to the brain is challenging due to the blood-brain barrier (BBB). In Chapter I, I summarize the current strategies applied to enhance the brain delivery of therapeutic proteins, including strategies to open the BBB, penetrate the BBB, or bypass the BBB. The advantages and challenges for each technology are described.

In Chapter II, we explore strategies to improve the brain delivery of leptin for treatment of obesity. Leptin is an adipocyte-secreted hormone that is delivered via a saturable transporter system across the BBB to the brain where it acts on receptors in hypothalamus to control appetite and thermogenesis. Peripheral resistance to leptin due to its impaired brain delivery prevents therapeutic use of leptin in overweight and moderately obese patients. To address this problem, we modify the N-terminal amine of leptin with Pluronic P85 (LepNP85) and administer this conjugate intranasally using the nose-to-brain route to bypass the BBB. We compare this conjugate with the native leptin, the N-terminal leptin conjugate with poly(ethylene glycol) (LepNPEG5K), and two conjugates of leptin with Pluronic P85 attached randomly to the lysine amino groups of the hormone. Our work suggests that selective modification at the N-terminal preserves leptin activity and modification with P85 enhances the nose-to-brain transport of leptin. In conclusion, LepNP85 with optimized conjugation chemistry is a promising candidate for treatment of obesity.

In Chapter III, we demonstrate for the first time that naïve macrophage exosomes interact with intercellular adhesion molecule 1 (ICAM-1) and C-type lectin receptors on brain endothelial cells that form BBB. Upregulation of ICAM-1, a common process in inflammation, promotes macrophage exosomes uptake in the BBB cells. We further demonstrate *in vivo* that naïve macrophage exosomes, after intravenous (IV) administration, cross the BBB and deliver a cargo protein to the brain parenchyma. The delivery is enhanced in the presence of brain inflammation. Taken together, macrophage exosomes are promising nanocarriers for brain delivery of therapeutic proteins.

ACKNOWLEDGEMENTS

TABLE OF CONTENTS

LIST OF TABLES

LIST OF FIGURES

LIST OF SCHEMES

LIST OF ABBREVIATIONS

2PCA   2-Pyridinecarboxaldehyde

AD   Alzherimers's diseases

Alix   Apoptosis-linked-gene-2 interacting protein X

AUC   Area under the curve

Aβ   Amyloid β

BACE1   β-secretase 1

BBB   Blood-brain barrier

BCSFB   Blood-cerebrospinal fluid barrier

BDNF   Brain derived neurotrophic factor

bFGF   Basic fibroblast growth factor

BMI   Body mass index

BSA   Bovine serum albumin

BSA   Bovine serum albumin

CD	Circular dichroism
CDI	1,1'-Carbonyldiimidazole
CED	Convection-enhanced delivery
Cl	Clearance
CNS	Central nervous system
CPM	Counts per minute
CPPs	Cell penetrating peptides
CSF	Cerebrospinal fluid
CTB	Cholera toxin subunit B
DC	Dendritic cells
DIO	Diet-induced obesity
DLS	Dynamic light scattering
DSP	Dithiobis(succinimidyl propionate)
DSS	Disuccinimidyl suberate
EDC	1-Ethyl-3-(3-dimethylaminopropyl)carbodiimide

EDTA	Ethylenediaminetetraacetic acid
EGTA	Ethylene glycol-bis(2-aminoethylether)-N, N, N', N'-tetraacetic acid
EIPA	5-(N-Ethyl-N-isopropyl) amiloride
ELISA	Enzyme-linked immunosorbent assay
FBS	Fetal bovine serum
Fc	The crystallizable fragment of immunoglobulin
FcRn	Neonatal Fc receptor
FDA	US food and drug administration
FUS	Focused ultrasound
G-CSF	Granulocyte colony stimulating factor
GDNF	Glial cell line-derived neurotrophic factor
GI	Gastrointestinal
GLP	Glucagon-like peptide
hCMEC/D3	Human cerebral microvascular endothelial cells

HEPES	4-(2-Hydroxyethyl)-1-piperazineethanesulfonic acid
HIV-1	Human immunodeficiency virus type 1
HLB	Hydrophilic-lipophilic balance
ICAM-1	Intercellular adhesion molecule 1
ICV	Intracerebroventricular
ID	Injected dose
IFN	Interferon
IGF	Insulin-like growth factor
IgG	Immunoglobulin
INB	Nose-to-brain/Intranasal delivery to the brain
IP	Intraperitoneal
IV	Intravenous
JAK	Janus kinases
Ki	Unidirectional brain influx rate
LAMP 2	Lysosome-associated membrane protein 2

LBD	Leptin-binding domain
LDLR	Low density lipoprotein receptor
LFA-1	Lymphocyte function-associated antigen 1
LPS	Lipopolysaccharides
MALDI-TOF	Matrix-assisted laser desorption/ionization-time of flight mass spectrometry
MΦ	Macrophage
MMP	Matrix metalloproteinase
MPS	Mononuclear phagocyte system
MRI	Magnetic resonance imaging
MRT_{inf}	Mean residence time from the time of dosing to infinity
MRT_{last}	Mean residence time from the time of dosing to last detectable concentration
MTr-Cl	4-Methoxytriphenylmethyl chloride
MW	Molecular weights
NCSA	Nasal cavity surface area

NGF	Nerve growth factor
NRMSD	Normalized root mean square deviation
NTA	Nanoparticle tracking analysis
OXM	Oxyntomodulin
P85	Pluronic P85
PAS	Penetration-accelerating sequence
PAsp(DET)	Poly(aspartate diethyltriamine)
PBS	Phosphate buffered saline
PD	Parkinson's disease
PDI	Polydispersity index
PEG	Polyethylene glycol
PEG5K-CHO	O-[2-(6-Oxocaproylamino)ethyl]-O′-methylpolyethylene glycol 5000
PEI	Polyethylenimine
PEO	Poly(ethylene oxide)

PI   Isoelectric point

PK   Pharmacokinetics

PLL   Poly(L-lysine)

PPO   Poly(propylene oxide)

PYY   Peptide YY3-36

Raw Mf   Raw 264.7 Macrophage

RIPA   Radioimmunoprecipitation assay buffer

RP-HPLC   Reverse phase-high performance liquid chromatography

RVG   Rabies virus glycoprotein

SC   Subcutaneous

SDS   Sodium dodecyl sulfate

SDS-PAGE   Sodium dodecyl sulfate polyacrylamide gel electrophoresis

SEC   Size exclusion chromatography

SOD1   Copper/zinc superoxide dismutase

SPECT   Single photon emission computed tomography

SPR	Surface plasmon resonance
STAT3	Signal transducer and activation of transcription 3
sulfo-NHS	N-hydroxysulfosuccinimide sodium salt
TAT	Trans-activator of transcription
TCA	Trichloroacetic acid
TcMRgFUS	Clinical transcranial MRI-guided focused ultrasound system
TEM	Transmission electron microscopy
TFA	Trifluoroacetic acid
TfR	Transferrin receptor
Tm	Midpoint of protein unfolding transition
TMB	Tetramethylbenzidine
TNBSA	2, 4, 6-Trinitrobenzene sulfonic acid
TrkB	Tropomyosin receptor kinase B
Tsg 101	Tumor susceptibility gene 101 protein
UV	Ultraviolet

VEGF   Vascular endothelial growth factor

Vi   Initial volume of brain distribution

Vss   Volume of distribution at steady state

CHAPTER I: CURRENT STRATEGIES FOR DELIVERY OF THERAPEUTIC PROTEINS TO THE CENTRAL NERVOUS SYSTEM[1]

1.1. BBB as a hurdle for brain delivery of therapeutic proteins

It is estimated that 1.5 billion people worldwide are suffering from CNS disorders, a number estimated to reach 1.9 billion by 2020 if curative treatments fail to emerge [1]. However, systemic drug delivery to the brain is hampered by three physiological barriers that separate the brain from the periphery. One is the BBB which restricts drug diffusion from blood circulation to brain parenchyma [2, 3]. Second is the blood-cerebrospinal fluid barrier (BCSFB) located at the choroid plexus and meninges to restrict drug diffusion from blood circulation to the cerebrospinal fluid (CSF) [2, 3]. The third is the ependyma in the ventricles that restricts drug diffusion from CSF to brain parenchyma [2, 3]. However, the high turnover rate of CSF (every 4.39 h in human [4]) and the barrier of ependyma render the drug delivered to the CSF less efficiently transferred to the brain parenchyma [2, 5, 6]. Hence, the BBB is universally considered as the main target for drug delivery to the brain due to its large blood-brain interface (20 m^2), which allows homogenous drug delivery to the brain parenchyma *via* nearby blood vessels [2, 3, 7].

Unlike the fenestrated peripheral blood vessels, the brain endothelial cells, the main component of BBB, are tightly sealed together by tight junctions which are established by intricate interactions between transmembrane proteins (such as occludin and claudin) and

---

[1] This chapter previously appeared as an article soon to be submitted.

cytoplasmic proteins (such as ZO proteins) that link to the actin cytoskeleton [8]. The permeability of tight junctions is tightly regulated by the surrounding neurons, pericytes and astrocytes [9]. Together these cells form a physical barrier that restricts the paracellular transport of soluble compounds larger than the pore size of tight junctions (4 Å) [2, 7, 8, 10]. In addition to being a physical barrier, the brain endothelial cells have low vesicle transport activities, high expression level of efflux transporters, and high activity of metabolic enzymes, limiting the transendothelial transport of drugs across BBB [2, 7]. Generally, only small lipophilic drugs that have molecular weights (MW) less than 500, logP between 1.5 to 2.5, no more than 5 hydrogen bond donor, and no more than 10 hydrogen bond acceptor can cross the BBB (Lipinski's rule of 5) [11]. Hence, 98% of the small molecular drugs are excluded from the brain by the BBB [5, 12].

Beginning with the launch of the first recombinant human protein, insulin, in 1982, protein-based therapeutics have transformed the pharmaceutical industry in the past three decades [13]. Therapeutic proteins may provide treatment for CNS disorders, such as neurotrophic factors for Parkinson's disease (PD) and antibodies for Alzherimers's diseases (AD) [1, 13, 14]. However, it is more challenging for therapeutic proteins to penetrate the BBB *via* the paracellular and transcellular routes due to their macroscopic size and hydrophilic nature. In addition, exogenous proteins are generally cleared rapidly from the blood circulation by enzymatic degradation and renal filtration, limiting the amount available for brain transport. Efficient delivery of intact/active therapeutic proteins across the BBB is critical for full appreciation of their disease-modifying potential in the CNS.

We review here the current strategies used for delivery of therapeutic proteins to the brain. These strategies are categorized into three broad groups: 1) strategies to transitly break down the

BBB, 2) strategies to enhance BBB penetration following systemic delivery, and 3) strategies to bypass the BBB. We focus on the mechanisms, considerations and limitations that one must take into considerations when designing brain delivery strategies for therapeutic proteins. In particular, we discuss here the newly-emerging bioinspired delivery carriers (category 2) and the nose-to-brain direct delivery route (category 3) using published examples and our own examples.

1.2. Current strategies used for delivery of therapeutic proteins to the brain

1.2.1. Strategies to disrupt BBB

To facilitate systemic delivery of therapeutic proteins to the brain, one can transiently disrupt the BBB using biochemical or mechanical methods. One commonly used biochemical method is osmotic shock. Intracarotid perfusion of a hyperosmolar mannitol or arabinose solution can induce shrinkage of endothelial cell and thereby open the tight junctions which allows larger molecules to penetrate [1]. In a rat model, intracarotid perfusion of hyperosmolar mannitol (25%, 0.26 ml/min for 30 sec) 3 to 5 min before the IV or intracarotid administration of a radiolabeled monoclonal antibody increased the brain/blood ratio of the antibody in the contralateral hemisphere (240%-280% increases) and the ipsilateral hemisphere (450%-500% increases) [15]. The elevation persisted for 7 days without significant increase in morbidity and mortality rates when compared to rats perfused with control saline [15]. In patients with melanoma metastasis in brain, osmotic BBB opening increased the penetration of a radiolabeled tumor-specific antibody to the brain tumor [16]. Similarly to the above example in rats, the accumulation of the antibody in the ipsilateral hemisphere of the osmotic shock was more than the contralateral hemisphere in human [16]. In the clinics where hyperosmolar mannitol was used to disrupt BBB and enhance brain delivery of monoclonal antibodies for treatment of glioma, no safety issue has been noted [17]. In addition to osmotic shock, infusion of vasoactive agent, organic solvents (such as

ethanol and dimethyl sulfoxide), detergents (such as sodium dodecyl sulfate (SDS) and polysorbate 80), immune adjuvants, and alkylglycerol were shown to open the BBB [1, 18]. Also, chronic brain local infusion of retinoic acid or phorbol myristate acetate can induce local and reversible cerebrovascular fenestrae possibly *via* induction of plasminogen activator urokinase [19].

In addition to biochemical disruption, the BBB can also be disrupted mechanically using transcranial focused ultrasound (FUS) in conjunction with circulating microbubbles. Unlike osmotic shock, FUS can permeabilize the BBB in a relatively small area guided by magnetic resonance imaging (MRI) [20]. The FUS can act directly on the vessel walls to increase permeability *via* two modes [1, 21]. First, expansion of microbubble in response to the FUC pulse can fill the capillary and mechanically stretch the vessel wall, resulting in opening of the tight junctions [1, 21]. Second, collapsing microbubbles causes highly localized shock waves and fluid jets toward the vessel walls [1, 21]. Furthermore, microbubble oscillation may trigger BBB opening indirectly by changing the local blood flow and pressure and by causing transient ischemia [21]. Indeed, Sheikov et al. showed that FUS opens tight junctions and increases the numbers of vesicles, vacuoles, and transendothelial channels using electron microscopy [21]. Jordao et al. showed that MRI-guided FUS increases the brain penetration of both exogenous antibodies against amyloid-beta peptide (Aβ) [22] and blood-borne endogenous immunoglobulins against Aβ [20]. Interestingly, apart from enhanced drug penetration to the brain, FUS may have some beneficial biological function acting to reduce the Aβ burden: FUS activates the surrounding astrocyte and microglia and thus increases the cell-mediated clearance of Aβ [20]. These cells are likely activated directly by the effect of FUS on the end-feet of these cells that are in contact with the BBB or indirectly by increasing stimulating serum factors [20].

This technique has also been applied to enhance brain delivery of other proteins such as neurotrophic factor [23-25], erythropoietin [26], interleukin-12 [27], and other monoclonal antibodies [28-30] in murine models. In these reports, no neuron damage was observed at the selected settings [20, 23-30]. Using a clinical transcranial MRI-guided FUS system (TcMRgFUS), McDannold et al. observed that focal BBB disruption can be reliably and repeatedly induced in rhesus macaques without observing histological or functional brain damage [31]. However, they also pointed out that clinical translation of this technique is complicated by the variability of BBB disruption from location to location [31]. Patchy and weak disruption of the BBB in the deep, lateral structures such as the hippocampus and lateral geniculate nucleus was observed [31]. The acoustic exposure level differs from location-to-location and is dependent on the incident angles between the transducer elements and the skull as well as the local microbubble concentration which is related to the tissue vascularity.

In general, for the above BBB disruption methods, it is critical to evaluate the BBB integrity in the disease model to predict if additional BBB disruption can further improve brain uptake. For instance, osmotic shock failed to boost the tumor uptake of a epidermal growth factor in a rat glioma model [32]. Indeed, significant tumor uptake of the growth factor (0.34 percentage of injected dose (ID%) per gram of tumor) was observed without osmotic shock [32]. Perhaps the BBB in this model is leaky enough for the penetration of this relatively small growth factor (6 kDa). As these methods destroy the self-defense system for brain and make the brain vulnerable to circulating cells and toxins, concerns of potential side effects such as seizures, brain edema, induction of new neurological disorders, and exacerbation of pre-existing disorders should be addressed [1]. The reversibility and time scale of BBB opening should be characterized.

1.2.2. Strategies to enhance BBB penetration

Several strategies have been developed to enhance brain penetration of systemically delivered therapeutic proteins without disruption of the BBB. One is to prolong the exposure of the therapeutic proteins to the BBB by extending the circulation half-life. Alternatively, one can increase the brain penetration of therapeutic proteins using non-specific or specific targeting modalities. Ultimately, the brain exposure depends on both the rate of BBB penetration and the amount available for BBB penetration [33]. More recently, biomimetic delivery systems using natural carriers such as cells and exosomes are developed to take advantage of their natural brain penetration property and long circulation.

1.2.2.1. Methods to extend circulation

The circulation half-lives of therapeutic proteins can be extended by modification with hydrophilic polymers or by genetic fusion with carrier polypeptides as extensively reviewed by others [13, 34-38]. These methods aim to increase the hydrodynamic size of therapeutic proteins so as to reduce their glomerular filtration.

A. Modification with hydrophilic polymers

The most common hydrophilic polymer used for extension of protein circulation half-life is polyethylene glycol (PEG) [13, 38]. Due to the strong hydration effect of the PEG chain, conjugation with PEG (PEGylation) significantly increases the hydrodynamic size of the proteins leading to reduced renal clearance. In addition, the hydration layer stabilizes the proteins by reducing aggregation and shields the modified proteins from proteolytic enzymes, antibodies, and immune cells [39]. Thus, it is generally believed that PEGylation can increase the protein solubility, colloidal stability, and proteolytic stability as well as mask their immunogenicity [40, 41].

However, chemical modifications with hydrophilic polymers usually negatively affect the biological activity of therapeutic proteins by sterically inhibiting target binding [38, 42]. In addition, in most cases, these polymers are randomly attached to the protein at ε-amino groups of lysines, resulting in a heterogeneous mixture of species modified at different lysines and modified with various numbers of polymer chains [42]. These species may differ substantially in their biological properties including pharmacokinetics (PK) and activity [42]. Unfortunately, isolation of a single species of isomers remains challenging. Therefore, site-specific modification is desirable to improve homogeneity and avoid modification at amino acids that are critical for interaction with the therapeutic target. Site-specific modification can be achieved by adjusting the reaction condition, introducing non-natural amino acids, eliminating potential modification sites *via* genetic manipulation, or utilizing specific enzyme reactions (transglutaminase, GlycoPEGylation[TM]) [42]. In our case, modification of the lysine amines of leptin with Pluronic P85 (P85) of poly(ethylene oxide) (PEO)-poly(propylene oxide) (PPO)-PEO structure using a cleavable disulfide linker generates a mixture of leptin conjugates modified with one or two polymer chains [43]. The modification with P85 significantly decreased the binding affinity of leptin to its receptor, the biological activity *in vitro*, and the brain influx rate *in vivo* [43]. The purified leptin conjugate modified with one chain of P85 (1:1 conjugate) was a mixture of five positional isomers with the polymer attached randomly to five different lysine amines [43]. Based on molecular dynamic simulation, the polymer chains attached at two of the five lysine amines (K6 and K12) sterically hinder the binding of leptin to its receptor [43]. By adjusting the reaction pH to a slight acidic condition, we are able to selectively modify the N-terminal amine of leptin with P85 based on the pKa difference between lysine amines and N-terminal amine

(Chapter II). The leptin N-terminal conjugate has higher binding affinity and brain influx rate when compared to the random lysine 1:1 conjugates.

In addition to site-specific modification, cleavable linkers can be used to release the proteins from the conjugates to recover the biological activity (a concept of prodrug or releasable PEGylation) [38, 42, 44]. We showed that reduction of the disulfide linker in the above leptin random lysine conjugates with P85 partially recovered the binding affinity to leptin receptor [43]. Non-covalent PEGylation has also been used to link PEGs to proteins in a nonpermanent way. The PEGylated proteins are formed *via* hydrophobic interaction, electrostatic interaction, or chelation between proteins and functionalized PEGs, resulting in reduced loss of potency due to chemical modification while retaining the benefit of PEGylation [45]. As summarized by Reichert and Borchard, the majority of these studies showed improved protein colloidal stability and/or thermal stability [46, 47]. However, very little is known for the *in vivo* PK and stability of protein non-covalent PEGylation [45]. Upon IV injection, weak protein-polymer complex may undergo a fast dilution and likely dissociation [45] resulting in limited extension of the circulation half-life. For instance, binding with nitrilotriacetic acid functionalized PEG8-(NTA)8 does not affect the PK profile of granulocyte colony-stimulating factor (G-CSF) [48]. Chelation with cucurbit[7]uril-PEG conjugates does extend the biological function of insulin *in vivo* after subcutaneous (SC) injection [47]. However, this effect is due to delayed absorption of insulin to the lymphatic circulation and improved proteolytic stability instead of prolonged blood circulation given the competition with serum proteins for cucurbit[7]uril-PEG binding [47]. Thus, the *in vivo* stability and circulation half-life of the protein-polymer complex should be investigated to confirm the improvement in protein delivery.

Nonetheless, the covalent protein-polymer conjugate that shows decreased activity *in vitro* may still be superior to the native proteins *in vivo* due to improved stability and reduced elimination [42]. As an example, leptin-P85 conjugates have lower brain influx rate than the native leptin [43] probably due to compromised interaction with leptin transporters on the BBB and slower transcytosis across the BBB due to polymer conjugation. However, the conjugates have higher brain uptake than unmodified leptin due to extended circulation half-life and improved *in vivo* stability, which prolong the exposure to the BBB thus nullifying the lower brain influx rate.

Although the adverse effects of PEGylated therapeutics seen in clinics are mainly related to the active drug molecules, pre-existing and treatment-induced anti-PEG antibodies are concerns for life-long application of PEGylated proteins [42, 49]. These antibodies have been correlated with accelerated clearance, loss of therapeutic efficacy, and hypersensitivity in clinics [49]. It is found that the anti-PEG immunogenicity increases with the original immunogenicity of the therapeutic protein and the hydrophobicity of the PEG end group, and decreases with polymer coverage [49]. In addition to immunogenicity problem, chronic intracellular accumulation of large PEGs (MW $\geq$ 30 kDa) in kidney and other organs such as liver and choroid plexus causes cell vacuolization in these organs, posing safety concerns [50]. It is still unclear if the cell vacuolization is an adaptive or a toxic response [50]. The finding of anti-PEG antibodies and vacuolization toxicity has stimulated the development of alternative polymers such as polyoxazoline, polyzwitterions, and polysaccharides [13, 37, 49, 51-53].

B. Modification with polypeptides

Alternatively, genetic fusion or chemical conjugation with naturally occurring long-circulating proteins has been used to prolong the circulation of therapeutic proteins. Such carrier

proteins include transferrin (Tf, circulates 7-17 days), the fragment crystallizable region (Fc) of immunoglobulin (IgG) (circulates 2-3 weeks), and human serum albumin (circulates 19 days) [34, 35, 54]. In addition to reduced renal elimination by increasing the size, Fc and albumin extend the circulation half-life by recycling the protein back into the vasculatures *via* the neonatal Fc receptor (FcRn) expressed on endothelial cells [34, 35, 54]. Using leptin (MW 16 kDa) as an example, fusion with Fc at the N-terminal (MW 98 kDa) extends the circulation half-life of leptin from 18 min to 9 h [55]. As a result, although the Fc-leptin fusion protein has 2- to 4-fold lower affinity *in vitro*, the fusion protein has higher potency *in vivo* [55].

In addition to natural proteins, conjugation with unstructured polypeptides are also used to extend circulation half-lives of therapeutic proteins [35, 49], including polypeptides consisting of alanine, glutamic acid, glycine, proline, serine and threonine in XTEN technology [36], proline, alanine, and serine in PASylation [56, 57], and elastin-like peptide [58]. The XTEN technology and PASylation demonstrate lower immunogenicity than PEGs [49]. Compared to synthetic polymers, the sequence and length of these polypeptides can be easily tuned to target desired MW and circulation half-life. Using leptin as an example, PASylation at the N-terminal dramatically increases the hydrodynamic size of leptin as measured by size exclusion chromatography (SEC) and dynamic light scattering (DLS) in a polypeptide length-dependent manner [56]. Accordingly, the circulation half-life of leptin can be extended from 26 min to 3.3 h, 7.0 h or 19.6 h in mice depending on the length of the PAS polypeptide. Similarly, the prolonged circulation of PASylated leptin offsets the loss of potency *in vitro*, resulting in extended receptor activation and anti-obesity efficacy in healthy mice after a single intraperitoneal (IP) injection [56]. Furthermore, compared to post-production polymer conjugation, genetic fusion with polypeptides bypasses the technical challenges in purification of different isomers of protein-

polymer conjugates [35]. Note that genetic fusion with carrier proteins or inert polypeptides may negatively or positively affect the expression of the therapeutic proteins. For instance, it is reported that fusion with Fc facilitates the expression of a soluble form of leptin in high yield [55].

In general, conjugation with hydrophilic synthetic polymers or polypeptides can offset the *in vitro* loss of potency due to conjugation as a result of prolonged circulation and thereby exposure to the BBB, and prolong efficacy, obviating the need for high dosing and high dosing frequency. However, such modifications further increase the hydrodynamic volume of therapeutic proteins, which may hinder the interaction with BBB transporters, resulting in impaired brain transport. It is shown that PEGylation (MW 20 kDa) of a leptin antagonist blocks its transport across the BBB [54]. Below are strategies aimed to directly enhance the penetration of therapeutic proteins across the BBB, which can be combined with techniques that extend circulation half-lives.

1.2.2.2. Non-specific strategies to enhance BBB penetration

The brain penetration of therapeutic proteins can be enhanced by means to enhance the protein interaction with the negatively charged lipid membrane of brain endothelial cells to initiate brain transport, including modification with amphiphilic polymers or cationic compounds. As dictated by the nature of the interactions, these strategies are not specific to brain.

A. Modification to increase lipophilicity

It is generally believed that hydrophobic molecules penetrate lipid membranes such as the BBB better than hydrophilic molecules. For small peptides, the more hydrophobic analogues penetrate the BBB more readily [1, 59, 60]. Chemical modifications that aim to reduce the hydrogen bonding potential or to introduce lipophilic groups have been used to increase the lipophilicity of small peptides, such as acetylation of the N-terminal amine, amidation of the C-

terminal carboxy group, esterification, and halogenation [1]. For large hydrophilic proteins, modification with highly lipophilic moieties is commonly used [61]. For this specific topic, Yi and Kabanov have recently published a retrospective overview on their own work since 1980s and the industrial development of such strategies, focusing on protein modification with fatty acids and amphiphilic polymers to enhance the transmembrane transport of proteins [62]. One problem with lipid modification is the partial retention of the conjugated proteins in the cell membranes. This could be solved by introducing cleavable linkers between the lipids and the proteins to allow dissociation of the proteins from the membrane [61]. More importantly, lipid modification enhances serum protein binding and sequestration by peripheral tissues, leaving fewer proteins available to be transported to the brain and eventually compromising the brain uptake of proteins [61]. Hence, a delicate balance in hydrophilicity-lipophilicity of the modified proteins should be targeted to allow sufficient hydrophobic interaction with the lipid membranes of brain endothelial cells while retaining high solubility in the blood circulation [61, 62]. Similar to PEGylation, the challenges of loss of potency, technical difficulties of purification, and the regulatory challenge of generating new chemical entities also apply here.

B. Modification to introduce positive charge

The luminal and abluminal sides of the brain endothelial cells as well as the basement membrane continuous to the abluminal side are covered by anionic glycocalx, thus presenting an overall negative charge, which allows interaction with cationized proteins to initiate adsorptive mediated transcytosis across the BBB [63]. A simple way to cationize a protein is amidation of its C-terminal or side chain carboxylic acid groups with diamines or polyamines such as putrescine and spermidine [63]. Similar to the above chemical modification method, cationization may compromise the protein activity and produce a heterogeneous product of

positional isomers and isomers with different modification degrees [63]. More importantly, due to its nonspecific adsorptive property towards anionic plasma membrane, cationization can negatively affect the PK and result in off-target organ distribution of the modified proteins [1, 63]. Cationized rat albumin with an isoelectric point (PI) around 8 after modification enables penetration to the brain, but has a shorter serum half-life (2.5 h) compared to unmodified albumin (4.8 h) [64]. Further cationization results in faster elimination. Bickel et al concluded that mildly cationized albumin with PI between 8 and 9 displays favorable PK properties and a greater selectivity to brain as compared to peripheral organs [33]. Similarly, coupling with hexamethylenediamine increases transcytosis of IgG across the capillary wall and into the brain interstitial space [65]. Toxicity issues such as endothelial damage and nephropathy are concerns at high doses due to the widespread deposit of the cationic species on blood vessel membranes [1, 33, 63, 66, 67].

Instead of direct cationization of the therapeutic proteins, covalent conjugation, genetic fusion, or physical complexation with cell penetrating peptides (CPPs) are often used to facilitate the permeation of therapeutic proteins across cell membranes [37, 68]. CPPs are a class of cationic peptides consisting of 5-30 amino acids that are capable of delivering cargo molecules across the plasma membrane [69, 70]. The CPPs that have been used for BBB permeation include trans-activator of transcription (TAT), penetratin, angiopep, rabies virus glycoprotein (RVG), and synB [70]. One of the most cited example is that TAT facilitates the transport of β-galactosidase (MW 116 kDa) to the brain along with other organs [71].

Similar to cationized proteins, it is generally believed that the cell uptake of CPPs is initiated by the interaction between CPPs and the cell-surface constituents such as the anionic lipids and proteoglycans *via* electrostatic interaction, hydrophobic interaction, or hydrogen bonding [68,

69]. Several determinants of the cell-penetrating efficiency of CPPs have been pointed out. Because the guanidinium head groups of arginine residues enable bidentate binding with cell-surface anionic components and offer stronger interaction than lysine residues, CPPs consisting of arginine residues are generally preferred over CPPs consisting of lysine residues [68, 72]. In addition, inclusion of hydrophobic residues such as tryptophan and the positioning of the hydrophobic residues can also affect the cell uptake [73]. Loss of the cell-penetrating efficiency after covalent conjugation or genetic fusion with therapeutic proteins has been observed, and this can be overcome by physical complexing of the CPPs with the protein cargo [68, 69]. However, the feasibility and stability of the complex largely depend on the protein cargo, the CPPs, and their ratio [74].

To date, most mechanic studies deals with the internalization process of CPPs into cells [68]. Depending on the concentration/type of the CPPs, type/size of the cargo, cell type, and experimental conditions, CPPs and CPP conjugates may utilize distinct pathways to enter the cells, including energy-independent direct translocation and energy-dependent endocytosis mediated by clathrin, caveolae, and macropinocytosis [68-70]. The functions of CPPs on the exocytosis process subsequent to cellular uptake in the case of transendothelical transport across the BBB are still unclear [68]. In addition to a cellular pathway, CPPs can enhance the brain uptake *via* modulation of the tight junctions [68]. Internalization into brain-infiltrating immune cells may also contribute to the increased brain uptake of CPP therapeutics. Gotanda et al. reported that poly-arginine (11 residues) accumulates to a greater extent and is retained longer in the mouse ischemic brain than in normal brain, especially in the ipsilateral side [75], showing a pattern similar to infilation of immune cells. In a separate study, enhanced infiltration of Mϕs along the infarct border has been observed in a rat ischemic model [76]. The enhanced brain

36

uptake and retention cannot be explained by a leaky BBB since poly-glutamate (11 residues) cannot penetrate the ischemic brain [75]. Indeed in another study, Schwarze et al. found TAT peptides and TAT fused β-galactosidase in the blood cells after IP injection [71]. Taken together, these likely suggest that CPP therapeutics can be transported to the brain by brain-infiltrating immune cells. Future studies detailing the BBB penetration mechanism of CPP therapeutics are needed.

Several limitations impede the clinical translation of CPP therapeutics. Due to their cationic nature, non-specificity is one of the major limiting factors [69]. CPPs therapeutics tend to distribute to sites close to the injection site and to well-perfused tissues such as liver, kidney, lung, and spleen [69]. Toxicity issues such as respiratory failure, neurotoxic cell death, and recruitment of inflammatory cells in brain as well as immunological responses have been reported [69]. Instability of the CPPs in blood circulation and extracellular/intracellular fluids is another limiting factor for the intracellular transduction efficiency [68, 69, 73]. Substituting L-amino acid with D-analogs [73] and inclusion of β-amino acids, γ-amino acids, or unnatural amino acids [69] have been applied to increase the stability of CPPs *in vivo*.

In addition to cationic polypeptides, therapeutic proteins can also be cationized by condensation with cationic polymers. Kabanov's group showed that negatively charged copper/zinc superoxide dismutase (SOD1) can be complexed with cationic polymers PEG-b-poly(L-lysine) (PEG-PLL) and PEG-b-poly(aspartate diethyltriamine) (PEG-PAsp(DET)) [77]. These polyionic complexes extend the circulation half-life of SOD1 and significantly enhance the protein brain uptake after IV injection [77].

1.2.2.3. Specific targeting strategies to enhance BBB penetration

Genetic fusion or chemical conjugation with targeting ligands recognized by the receptors highly expressed on the brain endothelial cells is another strategy to increase the brain permeability of therapeutic proteins. Compared to the above non-specific strategies, this brain targeted strategy could potentially lower the dose necessary to achieve therapeutically relevant concentrations in the brain and decrease potential peripheral toxicity. Upon binding to the receptors expressed on the brain endothelial cells, the targeted cargo is transferred across the endothelial cells *via* transcytosis, a transendothelial transport process which involves formation of membrane-bound vesicles on the luminal membrane and subsequent fusion with abluminal membrane to release the cargo to the brain interstitial fluids [78]. The best studied transcytosis receptors on the BBB are Tf receptor (TfR), insulin receptor, low density lipoprotein receptor (LDLR), and LDLR-related proteins 1 and 2 [63, 78]. Some detailed examples for each of these receptors as well as alternative targeting ligands such as FC5 antibody and RVG are reviewed elsewhere [78-80]. Most often, the therapeutic protein is genetically fused to or chemically coupled to the targeting vector [78, 81-85]. Noncovalent association between biotinylated therapeutic proteins and avidin/streptavidin-modified targeting vector has also been achieved [78-80, 86].

A wealth of information regarding the determinants of transcytosis capacity has been gathered for TfR. Researchers from Genentech, Inc. showed that TfR mediated transcytosis was capable to deliver therapeutic dose of TfR/ β-secretase 1 (BACE1) bispecific antibodies to the brain and lower the Aβ burden in mice [81]. The amount of TfR antibodies reach the brain parenchyma depends on the binding affinity to TfR [81]. At trace doses, brain uptake of TfR antibodies positively correlates with the binding affinity, with higher-affinity antibodies showing

higher brain uptake [81]. Counterintuitively, at therapeutic doses of TfR antibodies, the lower affinity species have higher brain uptake and penetrate better to the brain parenchyma than the higher affinity species [81]. The authors speculate that at therapeutic doses, the high peripheral concentration compensates for the low binding affinity and as a result, the TfR antibodies of low affinity display comparable binding to the luminal TfR receptors to the antibodies of high affinity. However, the antibodies of lower affinity are more likely to dissociate from the receptors on the brain side and less likely to be eliminated by receptor-mediated efflux from the brain, thus allowing higher brain uptake. In a subsequent study [82], they unraveled the cellular basis showing that when compared to low-affinity binding, high-affinity binding to TfR alters the subsequent intracellular trafficking, moving more TfR and TfR antibodies to the lysosome for degradation, resulting in a dose-dependent reduction of brain TfR levels, which further limits the amount of antibody penetrating the brain parenchyma. Note that high dosing of low affinity TfR antibodies also causes modest reduction of the brain TfR level. In another paper, they reported that reduced affinity to TfR also reduces serum clearance and thus improves brain uptake [83]. In addition to binding affinity, the valency of TfR antibodies affects the transcytosis efficiency across the BBB. A group of researchers from Hoffmann-La Roche showed that the monovalent form TfR antibodies better mimics the transcytosis trafficking of endogenous Tf, whereas the divalent form promotes lysosomal sorting and degradation perhaps by dimerizing the TfR [84]. Similarly, gold nanoparticle with high coating of Tf and hence high avidity are sequestrated in the brain endothelial cells instead of entering the brain parenchyma [87]. Moreover, it is reported that reduced binding affinity at endosomal pH 5.5 correlates with higher transcytosis efficiency [85]. Taken together, this suggests that understanding the transcytosis pathway subsequent to

TfR binding and releasing of the antibody on the brain side are important for the optimization of brain shuttle targeting TfR [88].

Currently, translation of TfR antibodies to clinic is impeded by safety concerns. In addition to brain endothelial cells, TfR is expressed on other cells such as circulating reticulocytes in mice, monkey, and humans [83]. Researchers from Genentech, Inc. reported that TfR/BACE1 bispecific antibodies cause reversible but severe acute clinical toxicity and reduction of circulating reticulocytes in mice [83]. The toxicity is linked to the effector function of the antibodies and complement-dependent cytotoxicity [83]. The authors speculate that primates will be less susceptible to the reticulocyte depletion seen in mice, due to less TfR+ circulating reticulocytes [83]. In addition, the authors propose that the toxicity can be ameliorated using the following strategies [83]. 1) Increase the affinity of the therapeutic arm to lower the dose and dose frequency of the TfR bispecific antibodies. 2) Reduce the TfR binding affinity. However, if the TfR binding affinity is too low, brain uptake is limited. 3) Eliminate Fc effector function by genetic mutation [89]. In addition to the acute toxicity, chronic toxicity of anti-TfR therapeutics should be investigated as well. While in most cases, the TfR antibodies are raised against a different epitope than endogenous Tf, concerns for interfering with endogenous iron transport still exist [81]. Gradual loss of the TfR receptor caused by high affinity antibodies or low affinity antibodies at high dose, especially in the clinical setting of chronic dosing, may potentially limit the amount of the therapeutics as well as endogenous ligands reaching the brain [81, 82]. For instance, pretreatment of rats with OX26, a mouse monoclonal antibody raised against rat TfR that binds to TfR without affecting the binding of iron-bound Tf [79, 88], inhibits iron uptake into the spleen and to the brain [90].

1.2.2.4. Bioinspired protein delivery system

In view of the complexity of BBB, it is intriguing to use natural delivery carriers with intrinsic brain penetration features to shuttle therapeutics to the brain.

A. Cell-mediated delivery

The intrinsic homing property of immune cells and stem cells to inflamed brain has been widely explored to shuttle therapeutics across the BBB [91, 92]. In particular, macrophages (Mϕs) are the most studied cell carriers for brain delivery likely due to their ability to engulf materials and release the materials at the disease site *via* exocytosis [92]. Mϕs are recruited to the brain for replenishment of the perivascular Mϕs [92, 93] and to a greater extent to the inflamed brain for tissue repair [92, 94, 95]. The recruitment is triggered by a cytokine gradient and upregulation of certain cell surface proteins in the injured sites and nearby blood vessels [96]. The cells can migrate across the BBB through the junctional complexes [97] or through elongated transendothelial channel-like structures formed by fusion of vesicles [96, 98, 99]. Selenica et al. transfected endogenous bone marrow derived Mϕs *in vivo* with green fluorescence protein and tracked these cells in murine models of acute and subchronic neuroinflammation [100]. The transfected Mϕs extravasate into the brain parenchyma in both neuroinflammation models, but not at detectable levels into healthy brains. Notably, the infiltrated Mϕs were primarily found in the brain parenchyma near the intoxication injection sites and more in the subchronic model which had higher levels of chemokines, displaying a disease homing pattern in response to the chemoattractant [100]. In a murine middle cerebral artery occlusion ischemic model, infiltrating Mϕs remain detectable in the brain at least for 14 days [101]. The disease homing property of Mϕs rationalizes the application of Mϕs for delivery of therapeutics to inflamed brain.

The brain homing property of Mφs has been explored for brain delivery of small molecules, therapeutic proteins, and DNA [102-107]. Batrakova's group loaded Mφs *ex vivo* with nanoformulated catalase (nanozyme) and showed that Mφs facilitate brain penetration of nanozyme [104-108]. In addition, they showed *in vitro* that upon reaching the brain, Mφs can transfer the catalase cargo to contiguous brain endothelial cells and neurons *via* bridging conduits, filopodia, and elongated lamellipodia [105, 109]. Interestingly, activation of Mφs using lipopolysaccharides (LPS) and interferon (IFN)-γ enhances the trafficking of nanozyme from the endocytotic compartments into the bridging conduit, suggesting triggered cargo release in response to inflammation [105]. Also, they showed *in vitro* that Mφs release exosomes that contain catalase, and these exosomes can transfer the cargo to distant cells [105, 109]. In another study from the same group, Mφs were transfected *ex vivo* with a plasmid DNA encoding catalase [102]. A single IV injection of these transfected Mφs produces a month-long expression of catalase in the brain and complete neuroprotection in a murine model of PD [102]. Exosomes released from these Mφs were found to contain the catalase plasmid DNA, mRNA, active protein, and a transcription factor, enabling expression of catalase in recipient cells [102]. Similarly, Mφs transfected *ex vivo* with a plasmid DNA encoding glial cell-line derived neurotrophic factor (GDNF) decrease inflammation in murine models of PD in two different studies [108, 110]. Release of GDNF in exosomes was observed [108]. All these studies indicate that Mφs can infiltrate the inflamed brain and upon reaching the brain, Mφs have means such as cell-cell contact or exosomes to transfer the therapeutic cargo to the brain cells.

Several considerations should be taken into account when designing such cell-mediated brain delivery system. From the cargo perspective, high drug loading is desirable to reduce the

required cell carrier number. The protein cargo can be loaded through three strategies. First, the cells can be transfected to express the therapeutic proteins [92]. Second, the cargo can be loaded into Mϕs *via* endocytosis. Third, the cargo can be attached to the cell surface without getting internalized (cellular backpack strategy) [111, 112].

In the loading by cell uptake strategy, it is critical to achieve high drug loading and at the meanwhile, protect the drugs from degradation by the cell carriers as well as killing the cell carriers. This can be achieved by incorporating the drugs into micro- or nanoparticles [113]. The particle geometry, surface properties, and plasticity affect cell uptake and thus loading efficiency [113-117]. Particles of relatively large size (0.3-1.1 μm), positively charge, and higher stiffness accumulate in Mϕs to a greater extent than particles of smaller size, negatively/neutral charge, and high softness [92, 113-117]. Batrakova's group showed that complex catalase with oppositely charged PEG-PLL or PEG-polyethylenimine (PEI) block copolymers increases uptake of catalase into Mϕs [104]. Furthermore, the cationic polymers preserve the protein cargo from lysosomal degradation *via* several mechanisms, including reduced sorting into lysosomes, enhanced endosomal escape, and delayed endosomal acidification [104, 105, 107, 118]. Also, the PEG block may shield catalase from attacking proteases [104, 105, 107]. However, compared to negatively charged copolymers, cationic polymers are more toxic to the cell carriers [118]. Introduction of the PEG block can partially shield the toxicity, but limits cell uptake [113, 118]. A balance between maximum cell uptake and minimum cell toxicity should be pursued.

In the cellular backpack strategy, the cargo can be attached to the plasma membrane through ligand-receptor interaction, biotinylation, or chemical conjugation [116]. The foremost challenge for this strategy is to avoid phagocytosis by Mϕs and avoid impairment of the cell migration

43

functions. Toward this goal, elongated and flat disk-shaped particles with high mechanical flexibility have been developed [111, 112] and exhibit no influence on the migration of monocytes across endothelial barriers and homing to inflamed tissues [112]. Compared to the cellular uptake strategy, the backpack strategy reduces cargo disintegration inside Mϕs and thereby reduces cell toxicity. The backpack strategy also opens up possibility of controlled drug release by external triggers. However, this strategy may have problems of premature drug release, detachment of backpacks [112], and immunogenicity [113].

From the carrier perspective, it is critical to evaluate if the brain homing efficiency of the cell carriers is sufficient to deliver a therapeutic dose to the brain. Increasing the injected cell number can reduce the competition from endogenous Mϕs and increase the carrier number present in the brain [119]. However, infiltrating immune cells may exacerbate the diseases. It is more desirable to optimize the brain homing efficiency of the cell carriers. The phenotype and *ex vivo* manipulation have been reported to affect the brain homing properties of Mϕs. In a murine acute brain inflammation model, freshly isolated bone-marrow derived monocytes penetrate the brain better than the monocytes cultured in the presence of Mϕ colony stimulating factor [119]. Cargo loading may also affect the cell brain homing efficiency. Loading with superparamagnetic iron oxide nanoparticles differentiates monocyte to Mϕs and reduces cell penetration to inflamed brain [120]. In addition, elongated *in vitro* cultivation and shear stress such as centrifugation are suspected to reduce the brain homing efficiency of monocytes/Mϕs [119].

It is also important to take into account the biological functions of the cell carriers, which may vary by phenotypes [92] and drug loading [120]. Zhao et al. selectively polarized Mϕs into anti-inflammatory M2 phenotype to avoid the proinflammatory effects of M1 Mϕs [108]. They

showed that empty M2 Mφs improve (although not significantly) neuronal survival in a murine

PD model [108], suggesting that appropriate differentiation of Mφs might provide additional

neuroprotective effects [92, 107, 108]. Notably, drug loading can alter the biological functions of

the cell carriers. Loading with superparamagnetic iron oxide nanoparticles has been shown to

alter cytokine secretion from Mφs and can shift the cytokine response toward either

inflammatory or anti-inflammatory response [120]. Different particles may have varied effect on

Mφ cytokine secretion [115]. For instance, poly(lactide-co-glycolide) particles trigger less

inflammatory response than polystyrene latex particles [115]. Taken together, the cell carriers

and conditions of *ex vivo* manipulation such as cell cultivation and drug loading should be

carefully selected based on the brain homing efficiency and biological functions of the cell

carriers.

Most importantly, successful application of cell-mediated brain delivery depends on the

extent and stage of brain inflammation, which may vary by disease type and disease progression

[91]. In addition, peripheral inflammation may divert the cell carriers away from the brain and

decrease the brain homing efficiency [92]. To enhance the migration of monocytes to the brain,

IV injection of hypertonic mannitol, bradykinin, and serotonin that can transiently disrupt the

BBB has been used [119, 121].

B. Exosomes

Exosomes are another promising type of natural delivery carriers. Exosomes are 40-200 nm

membrane-bound vesicles secreted by many cells *via* fusion of multivesicular bodies with

plasma membrane [122-124]. They were first discovered in the cell culture supernatant of rat

glioma C6 cells by Trams et al. in 1981 [125]. Subsequently in 1987, they were found to be

functional, serving to dispose membrane proteins such as transferrin receptors during reticulocyte maturation to red blood cells [126]. A breakthrough finding was published in 2007 where Valadi et al. showed that exosomes shuttled RNAs to other cells and modulated the function of the recipient cells [127]. Now, exosomes are widely recognized as natural nanocarriers delivering proteins, nucleic acids, and lipids to mediate intercellular communication locally or at distance [124, 128, 129]. This stimulates the exploration of using exosomes as drug delivery nanocarriers [130, 131].

Exosomes are suggested to mediate spreading of pathological proteins inside the brain and from the brain into CSF and peripheral circulation [132, 133]. These proteins include prions in prions diseases, Aβ and phosphorylated tau in AD, mutant superoxide dismutase in amyotrophic lateral sclerosis, and α-synuclein in PD [132, 133]. Viruses can also hijack exosomes for spreading over the body including the immune privileged brain [124, 129]. It is also shown that exosomes mediate the protein and gene cargo transfer from loaded/transfected Mϕs to brain endothelial cells and neurons [105, 108, 109]. Owing to the specific surface protein and lipid compositions, exosomes demonstrate greater cell uptake than artificial liposomes [134, 135]. Taken together, these studies suggest that exosomes are advantageous in facilitating cargo distribution within the CNS. It is intriguing to explore if exosomes could help conquer the BBB for brain delivery.

Several studies have investigated exosomes as brain delivery nanocarriers. Alvarez-Erviti et al. transfected bone marrow derived dendritic cells with a plasmid expressing a fusion protein of lysosome-associated membrane protein 2 (LAMP2b), an exosomal transmembrane protein, and RVG peptide that binds to neuron acetylcholine receptor [136]. As a result, the released exosomes were decorated with brain targeting RVG peptides. Following IV injection, these

modified exosomes delivered a therapeutic siRNA to the brain and caused brain-specific knockdown of the targeted BACE1. Zhuang et al. showed that various types of tumor exosomes reach the brain when administered intranasally and deliver sufficient curcumin and JSI24 to brain microglial cells to inhibit neuroinflammation and growth of implanted brain tumors [137]. Similarly, Haney et al showed that catalase loaded-Mφ exosomes demonstrate therapeutic efficacy in a murine model of PD by intranasal administration [138]. The laborious modification of exosomes with brain targeting ligands and the use of intranasal delivery which bypasses the BBB entirely raise the question whether naïve exosomes can penetrate the BBB.

In zebrafish embryos, Yang et al. showed that exosomes released from mouse brain endothelial cells can deliver a fluorescent marker to the brain, penetrating the BBB [139]. Furthermore in a zebrafish brain tumor model, they showed that these exosomes can deliver a chemotherapeutic agent doxorubicin to the brain at a therapeutic dose to suppress the growth of implanted brain tumor [139]. Considering that Zebrafish are phylogenetically further removed from humans when compared to preclinical animal models [140], it would be interesting to see if naïve exosomes could penetrate the BBB in other models such as rodents and primates.

Hwang et al. demonstrated in BALB/c mice that technetium-radiolabeled naïve exosomes from Raw 264.7 Mφs (Raw Mφs) and the exosome-mimetic nanovesicles extruded from plasma membranes of Raw Mφs and human neural stem cells show no significant brain uptake as detected by single photon emission computed tomography (SPECT) [141]. On the contrary, we showed *in vitro* that human brain endothelial cells can internalize naïve exosomes released from Raw Mφs through endothelial ICAM-1- and lectin receptors-mediated endocytosis (Chapter III). *In vivo*, we showed that iodinated Mφ exosomes slowly enter the brain in healthy CD-1 mice and

enter the brain faster and to a greater extent in brain-inflamed CD-1 mice. The contradiction between our study and the SPECT study can be explained by the difference in detection sensitivity and exosome size distribution. Specifically, they mentioned that the SPECT image of naïve exosomes in their study has poor quality and sensitivity due to low yield of exosomes. Their Mϕ exosome-mimetic nanovesicles have larger average diameter (218 nm) than ours (130 nm) using the same technique. The increased aggregation in their case may lead to increased sequestration by organs of the mononuclear phagocyte system (MPS) and lower brain uptake. In another study by a third group, fluorescently labeled exosomes released from autologous dendritic cells are detected in the mouse brains 24 h after IV injection [142]. These suggest that naïve exosomes can penetrate the BBB to some extent.

One challenge of using exosomes as nanocarriers for brain delivery is their limited circulation half-lives (within minutes [143, 144] or hours (Chapter III and [145])) when compared to cell-mediated delivery (in days). Such short circulation limits the amount of exosomes available for brain uptake. Due to their existence in a variety of biological fluids and their "self" nature, exosomes are assumed to be stable and circulating for a long time *in vivo*. However, recent publications demonstrate that exosomes from different species (human, rat, or mouse) and even murine exosomes from different mouse strains all show rapid clearance (from minutes to few hours) and sequestration by MPS organs such as liver, spleen and lung in mice [135, 141-145]. These data indicate that exosomes may not readily avoid the MPS sequestration. Smyth et al. showed that the blood clearance of exosomes is faster in healthy mice (the mean residence time from the time of dosing to infinity (MRT_{inf}) < 1 h) than in a mouse strain with impaired innate immunity and complement activity (MRT_{inf} 3.6 h), suggesting that the complement system contributes to the removal of exosomes from the circulation [135]. In terms

of the cellular mechanism for MPS sequestration, Saunderson et al. showed that CD169 expressed on Mϕs in lymph node and spleen can recognize the carbohydrate coating on exosomes and mediate the cell uptake of exosomes [146]. It is also assumed that Mϕs can recognize the phosphatidylserine enriched on the exosomal surface by their phosphatidylserine receptors [134]. We showed that Mϕ exosomes can interact with ICAM-1 and lectin receptors (Chapter III) and these receptors are expressed on immune cells [147, 148]. It would be interesting to see if brain uptake could be improved by engineering exosomes to exhibit stealth effects such as insertion of PEG modified lipids to shield them from the MPS.

Similar to cell-mediated delivery, exosomes released from different types of cells and cells at different stages may differ in their intrinsic targeting properties and biological effects, which can be either beneficial or detrimental to the desired therapy [130, 142]. Therefore, it is critical to characterize exosome compositions, PK, distribution, and long-term effects under normal and abnormal conditions to guide proper exosome selection.

1.2.3. Strategies to bypass the BBB

1.2.3.1. Intraparenchymal injection

Given the stability issues of macromolecules in blood circulation, their rapid elimination and the challenges of the BBB, therapeutic proteins have been administered directly into the brain to bypass the BBB and avoid peripheral clearance. Intraparenchymal injection directly introduces the proteins into the brain parenchyma [59]. The injected proteins can then spread to other brain regions *via* passive diffusion in the brain interstitial fluid, pulsatile movement along the perivascular channels, and/or transport *via* the cytoplasmic route mediated by glial cells [6, 149]. However, brain distribution of proteins following intraparenchymal injection is generally restricted to a few mm [59]. For example, it takes 2 h for nerve growth factor (NGF) to diffuse a

distance of 2 mm [59]. The migration of proteins through extracellular space is greatly retarded by their macroscopic size, the tortuous extracellular space, and protein binding to extracelluar matrix and cell surface components such as receptors and glycocalyx [150]. Due to the limited brain diffusion, precise positioning of the catheter at the target region is required [59].

Convection-enhanced delivery (CED), a high-flow microinfusion technique using an external pump connected to the catheters, has been implemented to enhance brain diffusion [151, 152]. CED is used in clinic to improve the spatial diffusion of immunotoxin (peptide toxins fused to tumor targeting peptides/proteins) [151-153] and radioimmunotherapeutics (radioisotope conjugated to tumor targeting peptides/proteins) [154, 155] to tumors and the surrounding brain infiltrated by tumor cells. Optimization to improve coverage of the tumor invasion zone and avoid leakage of the infusate back along the catheter can be achieved by tuning the number of catheters, their diameter, their trajectory, the infusion volume, and the infusion rate [152, 155-157]. This process is complicated by the brain geography and the difficulty of controlling catheter positioning, resulting in high rate of ineffective delivery [155]. Real time imaging of the convection process was proposed to identify and interrupt ineffective delivery [155].

1.2.3.2. Intra-CSF injection

Intracerebroventricular (ICV) injection and intrathecal injection directly introduces the proteins into the CSF [59]. Compared to intraparenchymal injection, administration into the CSF may allow distribution to larger brain regions *via* the immersion of CSF [59]. Leptin administered by intrathecal injection reaches the brain hypothalamus in amounts known to be biologically active for obesity in Baboons [158] and dogs [159]. Compared to SC injection, intrathecal injection of leptin achieves similar effects on body weight at a 500- to 1000-fold lower weekly dose in a dog model [159]. The driving force in the caudal movement of leptin

from the spine to the brain was suggested to depend on the rate of CSF reabsorption at the arachnoid villi [158]. Other successful protein brain delivery examples using ICV or intrathecal administration include antibodies and lysosomal enzymes as summarized by Calias et al. [4]. The authors suggest that lysosomal enzymes may be particularly feasible for ICV and intrathecal delivery as these enzymes can spread to distant brain regions *via* axonal transport [4].

Naturally, intra-CSF delivery has some limitations. Some proteins in the CSF of the subarachnoid space or ventricles may not readily penetrate the barrier of the pia matter or the ependyma to enter the brain parenchyma [59]. For example, diffusion of brain derived neurotrophic factor (BDNF) from CSF to the surrounding brain parenchyma was limited due to high expression of BDNF receptors on cells of the ependyma and pia matter [59]. Additionally, the rapid clearance of CSF to the venous and lymphatic circulation may outcompete the slow diffusion of CSF proteins across the cellular barriers [4, 59]. For instance, after a bolus injection into one lateral ventricle, insulin-like growth factor (IGF)-1 is rapidly cleared from the CSF with a half-life of 10 min in normal rats [160]. Three hours after the injection, less than 10% of the injected dose remains in the brain and CSF, and the IGF-1 penetrates less than 1.25 mm into the periventricular brain tissue and mostly remains at the brain-CSF interface [160]. Similarly, ICV-administered GDNF minimally penetrates the parenchyma and fails to improve Parkinsonism in patients [161]. For proteins to reach the parenchyma at therapeutic amounts after intra-CSF administration, the proteins should have the following characteristics as summarized by Calias et al. 1) the protein has slow brain clearance, 2) the protein is resistant to enzymatic degradation within the CSF, 3) the target brain region is within the diffusible distance of a CSF-contacting area, and 4) the protein can distribute to deep brain tissues *via* receptor-mediated cellular uptake or *via* intercellular transfer (such as lysosomal enzymes as mentioned above) [4]. In addition to

limited parenchyma penetration, considerable inter-individual variance and species difference in brain parenchyma penetration after ICV and intrathecal delivery have been observed [158, 161], and can be further complicated with unreliable catheter placement and stability [4]. Furthermore, as with the case of intraparenchymal delivery, intra-CSF delivery is impeded by the invasiveness of reaching the administration site, surgery/catheter-associated infection risks, and difficulties of repeated dosing that is required for chronic diseases [4, 59]. Thus, non-invasive intranasal administration that bypasses the BBB and delivers drugs directly to the brain (INB delivery) is attractive.

1.2.3.3. INB delivery

A. Mechanisms of INB delivery

The BBB can be circumvented entirely by INB delivery. Intranasally administered drugs can reach the CNS *via* the olfactory nerves and trigeminal nerves which directly connect the nose to the brain [6, 162]. The olfactory sensory neurons are exposed to the olfactory epithelium located at the upper posterior segments of the nasal cavity [163]. Their dendrites converge into olfactory nerves, enter the brain through the cribriform plate, and terminate in the olfactory bulb [162, 163]. The trigeminal nerve innervates the olfactory epithelium and respiratory epithelium, and enters the brain through the pons and the cribriform plate [162, 163]. Thus intranasal drugs can travel along the olfactory and trigeminal nerves to the olfactory bulb and rostral brain regions or along the trigeminal nerves to the caudal brain regions such as the brainstem and spinal cord [6, 162, 164]. Throne et al. use a rat model to show that following intranasal administration, the olfactory and trigeminal regions possess the highest concentrations of radiolabeled IGF-1 and display a decreasing intensity gradient with distance from the nasal passages [164].

The transport along the olfactory nerves and trigeminal nerves occurs *via* endocytosis and subsequent intracellular transport or *via* bulk flow along the ensheathing channels around these nerve bundles and associated blood vessels following epithelium penetration [6, 163-166]. The rapid nature (in minutes) of intranasal drugs reaching the brain is often interpreted as evidence for the extracellular bulk flow process [162, 164, 167]. Theoretically, the intracellular process requires at least several hours to several days to reach the brain based on the transport rate in cultured neurons *in vitro* [162]. Intraaxonal transport to the olfactory bulb has been observed after intranasal administration of lectin wheat germ agglutinin-horseradish peroxidase conjugates in mice at 6 h [168]. However, the relative contribution of each pathway *in vivo* is unclear. Upon entering the brain, bulk flow driven by the pulsation of cerebral blood vessels [162, 169] and mixing with CSF and brain interstitial fluid [163] can facilitate the spreading of intranasal tracers in the brain. In addition, the rostral migratory stream embedded in the olfactory nerves provides another neuroanatomical connection for intranasal proteins to distribute from the olfactory bulb to the periventricular regions [170, 171].

B. INB delivery of therapeutic proteins in animals and humans

Functional delivery of therapeutic proteins to the brain following INB administration has been shown in many cases. Intranasally delivered IGF-1 was biologically active as evidenced by the activation of its signaling pathway in the olfactory bulb, spinal cord, and cerebellum [164]. Other therapeutic proteins that exert CNS functions following INB delivery in preclinical species include but are not limited to Orexin-A peptide [172], vascular endothelial growth factor (VEGF) [173], IFN-β [174], G-CSF [175], erythropoietin [176], interleukin-1 receptor antagonist [167], nerve growth factor [177], full length antibody [170], osteopontin [178], and polypeptide fusion protein [179].

The utility of using preclinical animal data to predict intranasal delivery efficiency in human remains controversial due to the interspecies differences [6, 163, 166]. Anatomically, the relative coverage of olfactory epithelium in the nasal cavity of human is lower than the most common preclinical animal models (**Table 1.1**) [163, 166]. Furthermore, human and monkeys use both nose and mouth to breathe at rest, while mice and rats are obligatory nose breather [166]. The inspiratory airflow in human is close to the floor of nasal passage, while in rat is upward and laterally [166]. The nasal secretion movement in human is mostly posteriorly to nasopharynx, while in rat is mostly anteriorly [166]. In addition to anatomical differences, the metabolic enzymes are different and the mucociliary clearance rate is slower in humans [6, 180]. While these differences most likely yield different patterns in drug deposition, residence time, and absorption efficiency, study of the brain distribution pattern and mechanism post INB delivery in human is impeded by ethical and practical limitations, including lack of a good indicator of drug concentration in the target brain site [6, 163]. Drug concentration in CSF is not a good indicator of drug concentration in brain parenchyma and brain subregion [6, 163]. Nonetheless, intranasal insulin is active in humans, exhibiting efficacy in improvement of memory function [162, 181-183], reduction of body weight [162], and regulation of stress and emotions [162]. Intranasal oxytocin demonstrates pro-social effects in humans and is currently under clinical investigation to examine its anti-obesity effects [162]. Intranasal orexin A has shown promising results in restoration of olfactory dysfunction and regulation of sleep in narcolepsy patients [162]. In conclusion, INB delivery is a viable method to deliver protein therapeutics to the brain. Progress in understanding the PK and INB transport mechanisms in preclinical animals may help predict the feasibility in human [163].

Table 1.1. Anatomical difference between the nasal cavity of preclinical animal models and human*

Parameter	Mice	Rats	Rabbits	Rhesus monkey	Human
Body weight (kg)	0.03	0.25	3	7	70
Nasal cavity volume (cm^3)	0.03	0.26	6	8	25
Nasal cavity surface area (NCSA, cm^2)	2.89	13.4	61	62	160
Relative surface area (cm^{-1})	96.3	51.5	10.2	7.75	6.4
Olfactory epithelium (% of NCSA)	47	50	10	10-15	8
Olfactory epithelium (cm^2)	1.37	6.75	6	6-9	12.5

*Data are from reference [163, 166].

It is critical to identify if the intranasal therapeutics have direct access from the nose to the brain. Alternatively, the protein can enter the brain *via* nasal absorption into the systemic circulation and subsequent blood-to-brain transport, which makes intranasal administration a detour. Intranasal insulin increases CSF insulin levels and improves memory in human without modulating blood glucose and insulin levels [181-184], suggesting that intranasal insulin has direct access to the brain and poses minimal if any risk of hypoglycemia [181]. Intranasal Orexin-A peptide [172], VEGF [173], IFN-β [174], G-CSF [175], IGF-1 [164], erythropoietin [176], and interleukin-1 receptor antagonist [167] all show enhanced brain accumulation and in some cases, improved CNS functions at similar or much lower doses than the doses required by systemic delivery routes (IV, IP, or SC administration). Notably, leptin is another example which clearly excludes the blood-to-brain pathway as the main pathway for brain uptake of the hormone following intranasal administration. Intranasal leptin effectively reduces feeding and body weight in a diet-induced obesity (DIO) rat model where the transport of leptin across the BBB is impaired [185, 186]. These data suggest that many therapeutic proteins have direct access to the brain following intranasal administration.

C. Formulation strategies to improve INB delivery

Formulation strategies using absorption enhancers, bioadhesive polymers, enzyme inhibitors, and nanoparticles have been studied [187-191], aiming to improve the stability, prolong the residence time, create a local drug depot, and enhance absorption across the mucosa epithelium.

The primary obstacle for intranasal administered drugs is penetrating the mucosa epithelium. Notably, delivery to the brain decreases as the molecular weight increases [192]. Note that no clear correlation between other physicochemical properties and the efficiency of INB delivery has been found [193]. The nasal epithelial tight junctions limit paracellular transport of

56

molecules with a diameter larger than 3.6 Å [192]. The diameter for a small peptide such as octreotide (MW 991 Da) is estimated to be on the order of 10 Å [192], suggesting that paracellular diffusion is restricted for macromolecules such as proteins. Lochhead et al. find it necessary to apply a nasal absorption enhancer matrix metalloproteinase (MMP)-9 to enable the fluorescence detection of Texas Red-labeled dextran (MW 10 kDa) in the brain following intranasal delivery, while dextran (MW 3 kDa) does not require the absorption enhancer [169]. MMP-9 can transiently down regulate the tight junction protein claudin-1 [191]. MMP-9 pretreatment also enhances intranasal delivery of chloramphenicol acetyltransferase (MW 75 kDa) to the brain [190]. Chemical conjugation with CPPs has also been shown to increase brain delivery of the conjugated proteins following intranasal administration [194, 195]. It is suggested that the CPPs act by overcoming the epithelial tight junction and facilitating cellular uptake into the epithelium supporting cells and intra-tissue diffusion [194, 196]. Addition of a penetration-accelerating sequence (PAS) to CPPs-conjugated glucagon-like peptide (GLP) -2 further promotes INB delivery of the conjugated protein [197]. The exact mechanism for the improvement made by PAS remains unclear, but PAS can promote endosomal escape [197], which likely suggests an intracellular pathway for the epithelium penetration process. In addition to chemical conjugation, coadministration with CPPs such as penetratin has been shown to enhance INB delivery of insulin [196, 198]. Compared to chemical conjugation, higher concentration of CPPs (in mM) is needed to form the physical complex with the protein *via* hydrophobic/electrostatic interaction [199], raising safety concerns. However, one-month twice daily administration of such high concentration of CPPs in rat shows no damage of nasal epithelial membrane and no elevation of inflammatory cytokines [200].

However, many of the absorption enhancers and tight junction modulators are used to enhance nose-to-blood absorption as well [192, 201]. Often in such studies aiming to enhance systemic delivery, the effect of nasal excipients on brain level of drugs is neglected. Mixing with penetratin as mentioned above for brain delivery of insulin also increases the systemic absorption of insulin, GLP-1, exendin-4, and IFN-β following intranasal administration [198, 202]. In Chapter II, we explore whether modifying leptin with P85 could improve INB delivery of the hormone. The hydrophobic PPO block in P85 can facilitate the conjugated leptin penetrate across the epithelial layers to reach the underneath olfactory and trigeminal neurons *via* which the protein can enter the brain. We show that compared to unmodified leptin, leptin-P85 conjugates increase leptin accumulation in brain hypothalamus and hippocampus as well as the systemic absorption. The hydrophobic PPO block is necessary. Leptin modified with a chain of PEG which only consists of the hydrophilic PEO block has lower brain accumulation and systemic absorption than leptin-P85 conjugates. This suggests that methods aiming to enhance the penetration across the epithelial barriers likely increase brain delivery and systemic delivery simultaneously. Furthermore in another case, coadministration with a nasal absorption enhancer lysophosphatidylcholine only enhances the systemic absorption but not the brain delivery of leptin [203]. In one case, simultaneous improvement in brain delivery and inhibition of systemic absorption is achieved by inclusion of a vasoconstrictor phenylephrine in the intranasal administration of a neuropeptide orexin [204]. The rationale is to reduce systemic absorption so as to have more peptides available for brain delivery [204]. Therefore, for drugs that display intolerable peripheral toxicity, it is critical to characterize the effect of nasal absorption enhancers/excipients on both INB delivery and systemic absorption.

Notably, inclusion of nasal absorption enhancers/excipients may also affect the drug distribution pattern in the brain. Inclusion of phenylephrine increases distribution of orexin to brain regions associated with the olfactory pathway but not brain regions associated with the trigeminal nerve [204]. This is likely due to reduced cerebral blood flow and thus suppressed perivascular transport to the caudal brain [204], which is of longer transport distance [163, 166]. Other excipients such as bovine serum albumin (BSA) [205] and cyclodextrins [206, 207] have been reported to improve brain uptake of some proteins and affect their pattern of brain distribution. Therefore, the effect of nasal excipient on drug brain distribution pattern need to be characterized especially when targeting a specific brain region is desired.

In addition to nasal absorption enhances, strategies that enable prolonged residence time and sustained release enhance INB delivery. Compared to the naked protein solution of a vasoactive intestinal peptide, a PEG-poly(lactic acid) nanoparticle formulation significantly increases the brain accumulation and reduces the peripheral exposure of the peptide following intranasal delivery [189]. The increased brain exposure is due to improved stability and sustained release of the peptide in the nasal cavity which result in longer presentation of the intact peptide [189]. Modifying the nanoparticle surface with wheat germ agglutinin further enhances the retention in the nasal cavity and brain uptake [189]. Similarly in another case, modifying the particle surface with bioadhesive chitosan is superior to bare nanoparticles in INB delivery [188]. These studies indicate that extended nasal residence time and sustained release of the intact protein benefit INB delivery.

D. Optimization of drug deposition in the nasal cavity

The drug deposition pattern in the nasal cavity is critical for the efficiency of both CNS and systemic delivery [6]. The olfactory pathway is suggested to be the main target for INB delivery

for several reasons [162, 163]. First, the olfactory epithelium lacks cilia mobility and hence has slower mucociliary clearance than the ciliated respiratory epithelium [163]. Second, the travel distance from olfactory epithelium to the olfactory bulb (around 4 to 5 mm) is much shorter than the distance from nasal epithelium to the brainstem (around 20 to 30 mm) [163, 166]. Third, the olfactory sensory neurons penetrate deeper to the mucosa epithelium (to the level of tight junction) than the trigeminal nerve [163]. Additionally, the olfactory sensory neurons regenerate every 3-4 weeks, creating a leaky window for drug absorption [163]. For these reasons, the olfactory epithelium is the target for INB delivery. On the contrary, the respiratory epithelium, due to its greater surface area, is the main target for systemic delivery [208].

However, the ideal intranasal dosing technology for INB delivery remains to be identified. In murine models, the dose (in 10-100 μl) is generally given under anesthesia at supine position in liquid drops at the edge of the nares [164, 167, 173, 177, 178] or *via* a tube inserted into the nares [175, 176, 209]. By changing the tube insertion depth from 7 mm to 15 mm to increase drug deposition in the posterior olfactory epithelium and decrease the deposition in the respiratory epithelium, Charlton et al. show that the brain uptake of a small molecule is increased while the systemic exposure is reduced in an anesthetized rat model [210]. It is reported that brain uptake and systemic absorption of hydrocortisone are higher when the dose is given at head position of supine-90° angel position than at head position of upright-90° angel position in rats [211]. Furthermore, anesthesia that allows mice lie on their backs for long time increases the drug contact time with the mucosa epithelium, leading to increased brain uptake when compared to conscious condition [212]. In addition, the status of consciousness and the type of anesthetics may affect the rate of mucociliary clearance and therefore the residence time of intranasal medications [213]. Taken together, the dosing volume, tube insertion depth, head position, and

anesthesia procedures can be tuned to optimize drug deposition pattern in the nasal cavity and brain uptake in preclinical murine models.

Targeting the olfactory epithelium is more challenging in humans than in preclinical murine models, which have higher coverage of olfactory epithelium [6]. Specifically in humans, the drug should pass through the narrow triangular shaped nasal valve to reach the posterior olfactory epithelium [6]. Drug deposited inferiorly tends to pass along the nasal floor to the base of the tongue and be swallowed [6]. Djupesland et al. review in detail the currently available intranasal devices [6]. In general, the best intranasal device intended for INB delivery has not been identified, given that the nasal deposition pattern in humans and preclinical animal models using these devices is largely missing [6]. Comprehensive characterization of drug deposition pattern using each intranasal device is needed for the selection and further optimization of the device.

Currently, the ID% reaching the brain following INB delivery is usually lower than 1% and can be as low as 0.1% or even less [6]. Given the limited volume of the nasal cavity, INB delivery is only suitable for very potent drugs [6]. Understanding the transport mechanism and optimization of the formulation and device can help improve the efficiency of INB delivery. Notably, changes of nasal epithelium structure and the olfactory function caused by toxicity of drugs/excipients or mechanical force by the use of nasal device should also be studied in repeated dosing.

1.3. Summary and future directions

In summary, the current strategies used to deliver therapeutic proteins to the brain are reviewed here. The *pros* and *cons* of each strategy and considerations for further optimizations are described. All of the delivery strategies presented here focus on increasing the amount of

drug reaching the brain. Strategies to increase drug distribution to specific brain resident cells and strategies to prolong drug retention in the brain are also needed but beyond the scope of this review. The brain delivery strategies should also take into account that the brain undergoes dynamic changes during disease progression and drug treatments, which may affect the delivery efficiency and brain distribution [94].

CHAPTER II: INTRANASAL DELIVERY OF N-TERMINAL MODIFIED LEPTIN-PLURONIC CONJUGATES FOR TREATMENT OF OBESITY[2]

2.1. Introduction

According to World Health Organization, 39% of worldwide adults are overweight with body mass index (BMIs) 25.0–29.9 kg/m^2 and 13% are obese with BMIs at or above 30 kg/m^2. These subjects have higher risk of developing type 2 diabetes, cardiovascular diseases, musculoskeletal disorders, and cancers [214]. Dietary restriction and physical exercise are rarely effective in lasting weight loss [214]. Yet, there are very limited obesity pharmacotherapies available. Safety and toxicity issues have plagued development of small-molecule obesity drugs. Several weight-loss drugs (e.g., sibutramine, rimonabant) were approved but later withdrawn from the market due to unacceptable safety profiles. Currently, Contrav® (naltrexone/bupropion), Xenical® (orlistat), Qsymia® (phentermine/topiramate), and Belviq® (lorcaserin) are the only US food and drug administration (FDA)-approved drugs for long-term treatment of obesity [215]. However, these drugs have low compliance and limited weight-loss efficacy due to significant toxicity issues such as suicide risk (buproprion), unpleasant gastrointestinal (GI) side effects (Xenical), birth defect (topiramate), and heart valvulopathy (lorcaserin) [214-216]. In view of the safety setbacks associated with small-molecule obesity drugs, hormonal therapy has attracted

---

significant attention. Specifically, GI hormones (e.g., leptin, GLP-1, oxyntomodulin (OXM), peptide YY_{3-36} (PYY), ghrelin, pancreatic polypeptide) have been tested in clinics as treatments for obesity. Although the clinical trials of these hormones have generally shown satisfactory toxicity profiles, they each have drug delivery issues including short blood half-lives, and their efficacy performance so far has been disappointing [217-219].

Leptin (16 kDa) is secreted by fat cells and then acts in the brain hypothalamus to regulate appetite and thermogenesis [220-222]. It reaches the brain via a saturable transporter system located at the BBB and choroid plexus [186, 221]. Although Amgen terminated efforts to develop leptin as a treatment for obesity [218, 223], their studies and those of many others have yielded a wealth of information regarding both the biology and pharmacodynamics of the hormone. For example, it is now appreciated that earlier attempts of leptin monotherapy were not successful due to the phenomenon of leptin resistance in obese patients [186]. Nonetheless, leptin was well tolerated and effective in leptin-deficient obese patients [224]. Recent studies have shown that leptin resistance can occur via three mechanisms depending in large part to the degree of obesity present. These mechanisms include: 1) defective transport at the BBB, 2) impaired leptin receptor function in the hypothalamus, and 3) disruption of anorectic downstream neuronal circuitries [225-227]. The latter mechanism of resistance appears to be less important in humans than the first two. In contrast, the ability of clinically relevant amounts of the hormone to cross the BBB (peripheral resistance) and receptor dysfunction (central resistance) are critical considerations in any attempt to develop a leptin-based drug. It is well known that peripheral resistance due to leptin transporter defects predominate over brain receptor defects early on in outbred DIO rodent models with milder forms of obesity; whereas, both the BBB and receptor are largely dysfunctional in severe obesity [226]. Modeling based on CSF and serum

levels of leptin indicates that in advanced obesity in humans (BMI > 30 kg/m^2, leptin serum levels about 40 ng/ml), transporter defects account for almost two-thirds of resistance to peripherally administered leptin [228]. Thus, just as in the rodent and canine models [159, 229, 230], it is expected that moderately obese humans who show a poor response to leptin would respond better to a form of leptin that could reach brain receptors [231]. Indeed, leptin entry to the brain is greatly complicated by obesity, triglycerides, fasting, hyperglycemia, insulin, and inflammation [54, 232, 233]. An impaired BBB transport is important in the maintenance and probably in the progression of obesity [226, 229, 234]. Therefore, we believe that improved delivery of leptin to the brain could significantly improve its therapeutic effect when administered to subjects that are at increased risk for disease [235]. Specifically, the target patient population is overweight or mildly obese as it is in these individuals where one would expect peripheral resistance to be the most critical determinant of efficacy (as opposed to severe obese individuals in which central resistance predominates).

To improve the delivery of leptin to the brain, we previously modified leptin randomly at five lysine amines via a degradable crosslinker with P85, an amphiphilic triblock copolymer of PEO-PPO-PEO [43, 236]. Modification with a single chain of P85 (1:1 conjugate) or two chains of P85 (1:2 conjugate) prolonged the circulation of leptin in the blood and resulted in increased brain accumulation of leptin after IV administration. While 1:1 conjugate relied on the leptin transporter to enter the brain, the 1:2 conjugate was independent of the transporter [43]. Both random conjugates, however, represented a heterogeneous mixture consisting of several positional isomers and displayed a significant loss of activity [43]. Here, we propose to selectively modify the N-terminal amine of leptin with P85 (LepNP85) to improve the homogeneity of the conjugate and minimize the steric hindrance of the polymer chain upon

binding of leptin to its receptor. Additionally, we evaluate the nose-to-brain (INB) administration route to deliver the conjugates directly to the brain, thereby minimizing their exposure to peripheral clearance and bypassing the BBB. We determined here whether the P85 modification of leptin facilitates INB delivery of the hormone by improving its transport across the epithelial barriers.

2.2. Materials and methods

2.2.1. Materials

Pluronic P85 (P85, lot no.WPYE537B, average M.W. 4600) was a gift from BASF Corp. (Parspany, NJ). Disuccinimidyl suberate (DSS) linker, dithiobissuccinimidyl propionate (DSP), radioimmunoprecipitation assay buffer (RIPA buffer), 5% 2,4,6-trinitrobenzene sulfonic acid (TNBSA) solution, Corning^TM high binding polystyrene 96-well plate, SureBlue Reserve^TM tetramethylbenzidine (TMB) peroxidase substrate, and 100 x protease and phosphatase inhibitor cocktail were all purchased from ThermoFisher Scientific (Rockford, IL). Sephadex LH-20, PD-10, and Illustra Nap columns were purchased from GE Healthcare Life Sciences (Pittsburgh, PA). 4-15% Mini-PROTEAN® TGX^TM Precast Gel, ProteOn^TM GLC sensor chip, 1 M ethanolamine·HCl, 1-ethyl-3-(3-dimethylaminopropyl)carbodiimide (EDC), and N-hydroxysulfosuccinimide sodium salt (sulfo-NHS) were purchased from Bio-Rad Laboratories (Hercules, CA). Recombinant mouse leptin and recombinant human leptin receptor-Fc chimeras were purchased from R&D Systems (Minneapolis, MN). Na^{125}I and Na^{131}I were purchased from PerkinElmer (Waltham, MA). Signal transducer and activation of transcription 3 (STAT3) rabbit monoclonal antibodies and 66rimethy-STAT3 (Tyr705) rabbit monoclonal antibodies were purchased from cell signaling (Danvers, MA). O-[2-(6-Oxocaproylamino)ethyl]-O′-methylpolyethylene glycol 5000 (PEG5K-CHO, lot no.BCBM0003V, average molecular mass

5000 Da), 4-methoxytriphenylmethyl chloride (MTr-Cl), 1,1'-carbonyldiimidazole (CDI), sinapinic acid, BSA, protein G, Amicon ultra centrifugal filter units (MW cut-off (MWCO), 10 kDa), 4-(2-hydroxyethyl)-1-piperazineethanesulfonic acid (HEPES), and all other chemicals were purchased from Sigma-Aldrich (St-Louis, MO).

2.2.2. Synthesis of leptin conjugates

2.2.2.1. Random lysine conjugate

Leptin random lysine conjugates were synthesized as previously reported (**Scheme 2.1a**) [237]. Briefly, mono-amine-P85 was prepared from P85 in three steps (**Scheme 2.1b**). First, P85 (**1**) was reacted with MTr-Cl (1.1 molar equivalent) in anhydrous pyridine for 5 days at 23 °C. Unreacted MTr-Cl, bis-MTr-P85, mono-MTr-P85 (**2**), and unreacted P85 were then eluted sequentially from silica gel column in dichloromethane with stepwise increase of methanol (2%, 5%, and 10%). Second, **2** was reacted with CDI (5 molar equivalents) in anhydrous acetonitrile for 2 h at 23 °C, quenched with 0.2 ml of water for 20 min, and then mixed with ethylenediamine (20 molar equivalents) to obtain MTr-P85-amine (**3**). **3** was purified on a Sephadex LH-20 column in methanol and dried in vacuo. Third, **3** was dissolved in dichloromethane and mixed with 2 ml of trifluoroacetic acid (TFA) for 1 h at 23 °C to remove the MTr group and obtain mono-amine-P85 (**4**). The reaction mixture was dried in vacuo, dissolved in methanol and then neutralized by 67rimethylamine. The product **4** was also purified on a Sephadex LH-20 column in methanol (37 wt% yield).

To attach mono-amine-P85 to leptin, mono-amine-P85 was activated with 20 molar equivalents of DSS or DSP (**Scheme 2.1c**) in dimethylformamide / 0.1 M sodium borate, pH 8.0 for 30 min, and then purified on an Illustra Nap-25 column in 20% ethanol. Five molar

equivalents of P85-DSP or P85-DSS polymers were immediately mixed with leptin in 20% ethanol/0.1 M sodium borate, pH 8.0 and incubated overnight at 4 °C.
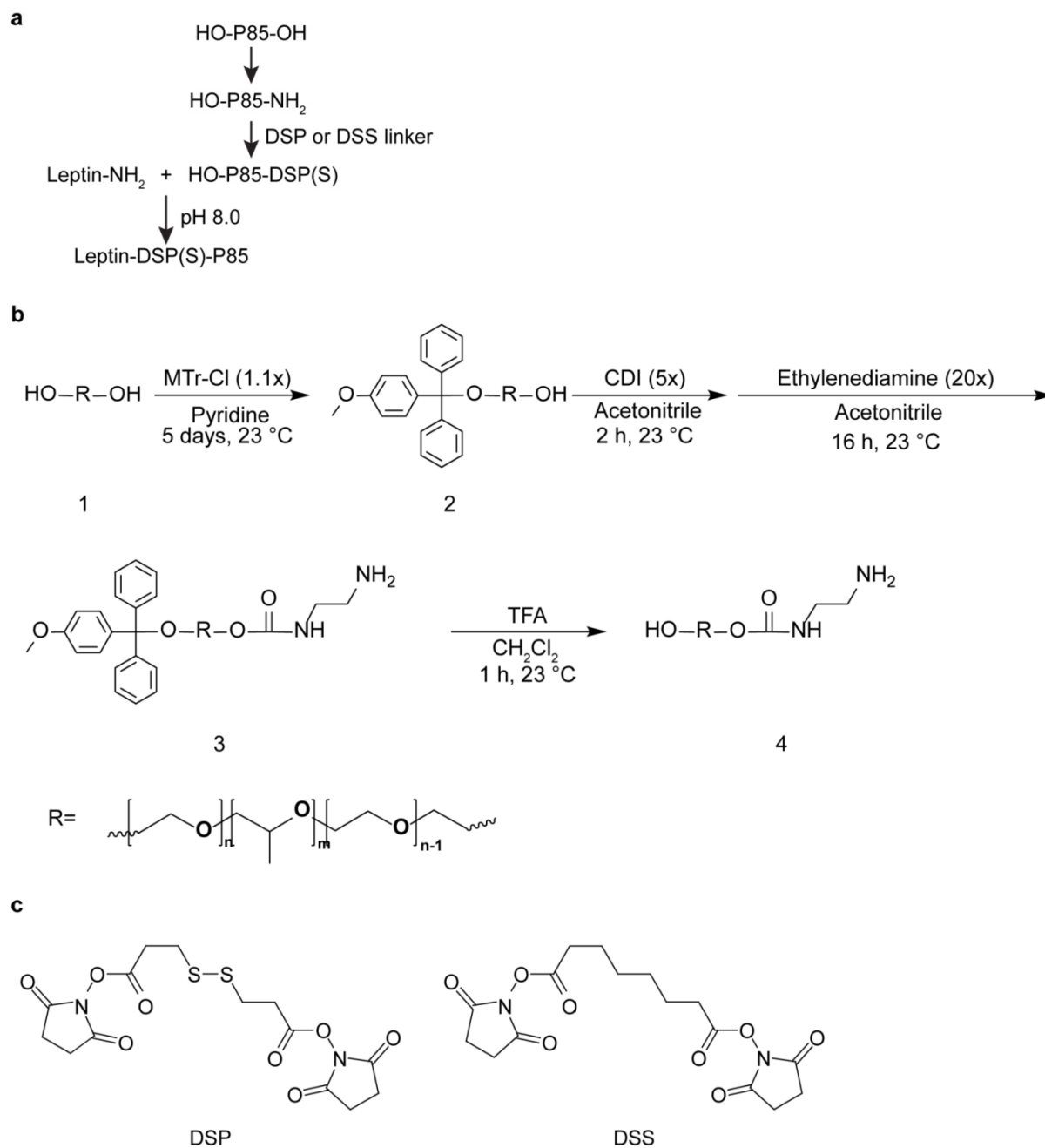
Scheme 2.1. Synthesis of leptin-P85 random lysine conjugates. (a) Synthesis scheme for leptin-P85 random lysine conjugates using DSP and DSS linkers. **(b)** Synthesis scheme for mono-amine-P85. **(c)** Chemical structures of DSP and DSS linkers.

2.2.2.2. N-terminal conjugate

Leptin N-terminal amine was selectively conjugated with in house synthesized mono-aldehyde-P85 (CHO-P85-OH) via reductive amination (**Scheme 2.2a**). Mono-propanediol-P85 was first synthesized and purified similarly to mono-amine-P85 but using 3-amino-1,2-propanediol instead of ethylenediamine (**Scheme 2.2b**, 46 wt% yield). CHO-P85-OH was synthesized from mono-propanediol-P85 by oxidation with sodium periodate in methanol/50 mM sodium acetate, pH 5.5 in the dark for 0.5 h at 4 °C, and then purified using Illustra Nap-25 column in 20% ethanol. To synthesize LepNP85, leptin was mixed with CHO-P85-OH (20 molar equivalents) in 20% ethanol/50 mM sodium acetate, pH 5.5 at 4 °C for 3 h, and then reduced by NaBH$_3$CN (final concentration 20 mM) at 4 °C overnight. The PEGylated analog of leptin N-terminal conjugate (LepNPEG5K) was synthesized similarly using commercial PEG5K-CHO at 5 molar equivalents.

Scheme 2.2. Synthesis of leptin- P85 N-terminal conjugate. (a) Synthesis scheme for leptin-P85 N-terminal conjugate by reductive amination. **(b)** Synthesis scheme for CHO-P85-OH.

2.2.3. Purification of leptin conjugates

After the conjugation, leptin conjugates were precipitated in cold acetone to remove excess of polymers. Singly modified leptin conjugate was then purified by SEC using ÄKTA FPLC system equipped with a ultraviolet (UV) detector at 254 nm (GE Healthcare Life Sciences). Large hydrodynamic size-protein aggregates, leptin conjugates, and free leptin were eluted sequentially from Superdex 75 100/300 GL column in 10% methanol/0.25 M sodium phosphate, pH 7.5 at 0.5 ml/min. Peaks were collected and characterized by sodium dodecyl sulfate polyacrylamide gel electrophoresis (SDS-PAGE) and matrix-assisted laser desorption/ionization-time of flight mass spectrometry (MALDI-TOF). The pooled fractions were buffer exchanged into 10 mM sodium phosphate buffer, pH 7.5 using Amicon ultra-15 centrifugal filter units (MWCO 10 kDa) and stored at -80 °C for further analysis. The yield of 1:1 modified leptin conjugates after FPLC purification was about 10% based on protein amount.

2.2.4. N-terminal amino group protection assay

The N-terminal amine of leptin was protected with 2-pyridinecarboxaldehyde (2PCA) as reported [238]. In brief, leptin was mixed with 400 molar equivalents of 2PCA in 0.1 M sodium borate buffer, pH 8 at 37 °C for 24 h, and then purified by PD-10 columns in 10 mM sodium phosphate, pH 7.5. The modification degree was determined by TNBSA assay following product protocol. Briefly, 50 µl of leptin or 2PCA protected leptin (Leptin-2PCA) (100-300 µg/ml) was mixed with 25 µl of 0.01% TNBSA in 0.1 M sodium bicarbonate, pH 8.5 at 37 °C for 2 h. Absorbance at 335 nm was read on a microplate reader SpectraMax M5 (Molecular devices). The modification degree (S) was calculated according to the following equation [239]: $S = 8 \times \frac{\left(\frac{A_{native}}{C_{native}} - \frac{A_{modified}}{C_{modified}}\right)}{A_{native}/C_{native}}$ where A and C are the absorbance and concentration of native leptin ($native$)

or Leptin-2PCA (*modified*), and 8 is the total number of primary amines in leptin monomer. Leptin and Leptin-2PCA was then mixed with CHO-P85-OH or P85-DSP as described in 2.2. The reaction mixtures were characterized by SDS-PAGE and MALDI-TOF.

2.2.5. Characterization of leptin conjugates

2.2.5.1. MALDI-TOF

Protein samples were prepared using the sandwich method and matrix of saturated sinapinic acid in acetonitrile/0.1% TFA (50/50, *v/v*). Briefly, 0.5 µl of matrix was deposited on an Opti-TOF™ 384-well target, air dried, followed by 0.5 µl of protein sample and another 0.5 µl of matrix. The target was then air dried. Mass spectra were collected on a 5800 MALDI-TOF/TOF system (Applied Biosystems/MDS SCIEX) in positive linear mode as previously reported [43].

2.2.5.2. SDS-PAGE

Five µg of protein samples (as determined by microBCA) were mixed with Laemmli sample buffer without reducing agents, denatured at 95 °C for 5 min, and then resolved on 4-15% Mini-PROTEAN® TGX™ Precast Gel at 120 v for 50 min. The gel was stained with coomassie blue G250 and imaged by FluorChem E System (ProteinSimple).

2.2.5.3. Far UV-circular dichroism (CD)

The secondary structures of leptin and leptin conjugates were characterized by far UV-CD. The proteins were diluted with 10 mM sodium phosphate, pH 7.5 to 0.1 mg/ml. CD spectra from 190 to 260 nm were recorded using Chirascan™-Plus CD Spectrometer (AppliedPhotophysics, Beverly, MA) at the following settings: cell pathlength 10 mm, bandwidth 1.0 nm, step 0.5 nm, time-per-point of 1.25 s (50,000 repeats per point), and temperature 20 °C. For each sample, three repeated scans were recorded, averaged, subtracted the buffer background, smoothed, and

then normalized by ellipticity at 222 nm to adjust for minor difference in protein concentrations.

Mean residue molar ellipticity (degrees·M^{-1}·m^{-1}) was calculated using equation $[\boldsymbol{\theta}] = \frac{\theta \times 100 \times M}{C \times l \times n}$

where $\boldsymbol{\theta}$ is the recorded ellipticity in degrees, $\boldsymbol{M}$ the molecular mass (16,140 g/mol), $\boldsymbol{C}$ the

protein concentration in mg/ml (0.1 mg/ml), $\boldsymbol{l}$ the cell pathlength in cm (0.1 cm), and $\boldsymbol{n}$ the

number of amino acid residues in leptin (147) [240]. The composition of secondary structures

and the goodness-of-fit parameter normalized root mean square deviation (NRMSD) were

obtained using online DichroWeb program CDSSTR and protein reference set 7 [241, 242].

2.2.5.4. Reverse phase-high performance liquid chromatography (RP-HPLC)

The relative hydrophobicity of leptin and leptin conjugates were compared by RP-HPLC: the

hydrophobic proteins were eluted later than the hydrophilic proteins. The proteins were eluted

from Jupiter C4 column (particle diameter 5 µm, pore diameter 300 Å, 4.6 x 100 mm) by

gradient elution at 1 ml/min and 25 °C, and monitored by absorption at 220 nm. Mobile phase A:

water + 0.1% TFA; mobile phase B: acetonitrile + 0.1% TFA: isopropanol 50:50 (*v/v*). The

elution started from 5% B for 5 min, then linearly increased to 95% B at 1%/min, and stayed at

95% B till 100 min.

2.2.5.5. DLS

The proteins were filtered through 0.2 µm PVDF membrane filter and then diluted to protein

concentration of 1 mg/ml with 10 mM sodium phosphate, pH 7.5. The size measurements were

carried out using Zetasizer Nano-ZS instrument (Malvern, UK) at the default scattering angle of

173° at 25 °C. Three repeated measurements indicated by gradient colors were shown for each

protein.

2.2.5.6. Surface plasmon resonance (SPR)

The binding affinity of leptin and leptin conjugates to leptin receptor was determined by ProteOn^{TM} XPR protein interaction array system (BioRad Laboratories) similarly as previous reports using BiaCore 2000 system [243] or BiaCore 3000 system [43]. Protein G was covalently immobilized on GLC sensor chip to allow capture of leptin receptor-Fc chimeras. In detail, 1600 resonance units (RU) of leptin receptor was captured by sequential injection of the following compounds to the vertical ligand channels at 30 µl/min: 1) 1:1 (*v/v*) mixture of 40 mM EDC/10 mM sulfo-NHS for 300 s, 2) 75 µg/ml of protein G in 10 mM sodium acetate, pH 4 for 120 s, 3) 1 M ethanolamine for 300 s, and 4) 10 µg/ml of leptin receptor in running buffer (10 mM HEPES, pH 7.4/150 mM NaCl/0.005% Tween 20) for 60 s. After 180 s equilibration at 50 µl/min, a serial dilution of leptin or leptin conjugates in running buffer was simultaneously injected to the horizontal analyte rows. A 150 s binding phase and a 1200 s dissociation phase were recorded at 100 µl/min. The protein G surface was then regenerated by injection of 10 mM glycine buffer, pH 2 at 100 µl/min for 18 s. The sensorgrams were auto-processed (injection alignment, baseline alignment and artifact removal), referenced to a ligand channel that had no leptin receptor for non-specific binding, and double referenced to a buffer analyte row for baseline shift (resulted from dissociation of leptin receptors). The equilibrium dissociation constants K_D (nM) were obtained by fitting the sensorgrams to a Langmuir 1:1 binding model using the instrument software.

2.2.6. Animal studies

All animal experiments were approved by the University of North Carolina Institutional Animal Care and Use Committee. 6-8 weeks male CD-1 mice were purchased from Charles River Laboratories (Wilmington, MA).

2.2.6.1. Leptin receptor activation in hypothalamus after ICV injection and INB delivery

The mice were anesthetized by IP injection of 40% urethane (4 mg/kg), and then injected with leptin or leptin conjugates in 4 μl of phosphate buffered saline (PBS) by ICV administration (0.2 mm caudal to bregma, 1 mm lateral to sagittal suture, and 3.5 mm in depth). Alternatively, the mice were injected intranasally with 8 μl of protein samples in PBS using a gel loading tip attached to a 10 μl pipette. The tip was inserted 4 mm deep to the depth of the cribriform plate [205] (2 μl per injection, alternate nostril between injections with 1 min apart). 30 min after ICV injection or 1 h after INB delivery, the mice were sacrificed. The brains were removed and dissected on ice to sample hypothalamus and hippocampus according to published procedure [244]. The tissue was homogenized in 100 μl of RIPA buffer supplemented with 1 x protease and phosphatase inhibitor cocktail. For ICV samples, 50 μg of homogenate proteins were analyzed by western blotting for phosphorylation of STAT3 at Tyr 705 (pSTAT3) and then total STAT3 after stripping. The band densitometry was quantified using Image J. For intranasal samples, 1 mg/ml of the hypothalamus lysates were analyzed using Wes instrument (ProteinSimple). The activity of leptin and leptin conjugate was reported as densitometric ratio of pSTAT3 to STAT3.

2.2.6.2. Pharmacokinetic study

A. Radioactive labeling

Leptin and leptin conjugates were labeled with iodine by chloramine T method [43]. Briefly, 10 μg of proteins were mixed with 1 mCi of $Na^{125}I$ or $Na^{131}I$ and 10 μg of chloramine T in 100 μl of 0.25 M sodium phosphate, pH 7.5 for 60 s. The proteins were then eluted from Illustra Nap-5 columns in PBS, collected in tubes pretreated with 1% BSA to prevent nonspecific adsorption, and concentrated to around 80 μl using Amicon ultra-0.5 ml centrifugal filter units (MWCO 10 kDa). The percentage of iodine associated with proteins in the final concentrated

samples was determined by trichloroacetic acid (TCA) precipitation [245]. Briefly, 1 µl of the concentrated samples was mixed with 0.5 ml of 1% BSA in PBS and 0.5 ml of 30% TCA by brief vortex followed by centrifugation at 5400g for 10 min. The radioactivity of the resulting protein pellet and supernatant was counted on r-counter (PerkinElmer). The percentage of iodine associated with protein was calculated as the percentage of pellet radioactivity in total radioactivity. Protein samples with percentage of iodine association higher than 95% were used.

B. Serum clearance and brain influx rate after IV injection

The mice were anesthetized by IP injection of 40% urethane (4 mg/kg). 4 x 10^5 counts per minute (CPM) of ^{125}I- and ^{131}I-labeled compounds in 0.2 ml of lactated ringer's buffer supplemented with 1% BSA were co-injected to the left jugular vein. At defined time points (1 to 180 min), blood was sampled from the right carotid artery, allowed to clot at 23 °C, and then centrifuged at 5400g for 10 min to collect serum. Immediately after blood sampling, the mice were sacrificed. The whole brains were removed and weighed. The brain/serum samples and four injection checks representing ID (CPM per mouse) were counted on r-counter simultaneously.

The CPM in brain/serum samples was divided by ID and multiplied by 100 to get %ID, and then normalized by weight for brain samples (Am, %ID/g) or by volume for serum samples (Cpt, %ID/ml). Ln(Cpt) was plotted against time (t, min) using Prism 5.0 software (GraphPad, San Diego, CA). The serum clearance rate (k, min^{-1}), half-life ($t_{1/2}$, min), and volume of distribution (V, ml) were calculated from the slope and y-intercept of the linear regression using the following equations [43].

$$Ln(Cpt) = k \times t + V$$

$$t_{1/2} = 0.693/k$$

The unidirectional brain influx rate (Ki, ml/g·min) and initial volume of brain distribution (Vi, ml/g) were determined by multiple-time regression analysis using the following equation [246]

$$Am/Cpt = Ki \frac{\int Cpt \cdot dt}{Cpt} + Vi$$

where Am/Cpt is the brain/serum ratios (ml/g), and $\frac{\int Cpt \cdot dt}{Cpt}$ the exposure time, which is the integral area under the curve (AUC) of serum concentration Cpt from time 0 to time t divided by Cpt at time t.

C. Serum absorption and brain regional distribution after intranasal administration

The mice were anesthetized by IP injection of 40% urethane (4 mg/kg). 2 x 10^6 CPM of [125]I- and ^{131}I-labeled samples in 2 μl of PBS were co-injected intranasally into the upper nasal area near cribriform plate by inserting a gel loading pipette tip 4 mm into the left nostril of each mouse [205]. The mice were laid naturally on their backs on a heating pad after injection. 5, 10, 20, 30 and 60 min later, serum was collected as mentioned above. The olfactory bulb, hypothalamus, hippocampus, and the rest of brain were sampled on ice following published procedure [244] and weighed. Radioactivity in serum and brain samples was counted. Six injection checks representing ID were counted simultaneously. Radioactivity in serum and brain samples were presented as %ID/ml and %ID/g, respectively as mentioned above. Note that the mice were not perfused. It is reported that the radioactivity in perfused brain was comparable to non-perfused brain after intranasal delivery of leptin, due to negligible material entering the blood [247].

D. Stability of iodinated proteins in serum and brain samples

The mice were dosed intranasally with 2×10^6 CPM of ^{125}I- and ^{131}I-labeled samples in 2 μl of PBS as mentioned above. 10 and 60 min later, blood was sampled by cardiac puncture and allowed to clot at 23 °C to collect serum. The mice were immediately perfused with ice-cold PBS. The brain was removed, homogenized in 2 ml of ice-cold PBS, and then centrifuged at 5400g for 10 min. 50 μl of serum and 1 ml of brain homogenate supernatant were precipitated with 1 ml of 30% TCA as mentioned above. Process controls that evaluate process-induced degradation were made by spiking untreated mice serum and brain samples with iodinated proteins and then being treated similarly as dosed animal samples. The stability of iodinated samples in serum and brain samples was evaluated as the percentage of radioactivity in the protein pellet [43].

E. Blood absorption and brain clearance after ICV injection

To study the clearance of leptin and LepNP85 from the brain, leptin and LepNP85 were labeled with biotin to distinguish from endogenous leptin. Briefly, the proteins were mixed with 40 molar equivalents of Sulfo-NHS-biotin in 10 mM sodium phosphate, pH 7.5 on ice for 2 h, and then purified by PD-10 column. 1 μg of biotin-labeled leptin or LepNP85 in 1 μl of PBS were injected locally into brain by ICV injection. At each time point, blood was sampled from carotid artery into heparinized tubes and centrifuged at 2000g for 15 min to collect plasma. The whole brain was removed and homogenized in 1 ml of RIPA buffer supplemented with 1 x protease inhibitor cocktail. The concentration of biotin-labeled protein in brain lysate and plasma were analyzed by enzyme-linked immunosorbent assay (ELISA). Briefly, a high binding polystyrene 96-well plate was coated with 1 μg/ml of recombinant leptin receptor-Fc chimera in

PBS overnight at 4 °C (0.1 ml per well). After trice wash with PBS, each well was blocked with 0.2 ml of 3% BSA/PBS at 23 °C for 1 h, and then incubated with 0.1 ml of biotin-labeled protein standards or brain/plasma samples diluted with 3% BSA/PBS for 2 h. After another trice wash with 0.2 ml of 0.05% Tween-20/PBS, each well was incubated with 0.1 ml of high sensitivity streptavidin-horseradish peroxidase (Pierce, 1:250 dilution) in 3% BSA/PBS for another 1.5 h followed by four washes with 0.05% Tween-20/PBS. Each well was then incubated with 0.1 ml of TMB peroxidase substrate for 15 min. The reaction was stopped by adding 0.1 ml of 2 M H_2SO_4 and detected at 450 nm.

2.3. Results

2.3.1. Synthesis and purification of leptin conjugates

The two leptin-P85 conjugates with the block copolymer attached to the protein's lysine amino groups via DSP linker (LepDSPP85) or DSS linker (LepDSSP85) were synthesized and purified as previously reported [43] (**Scheme 2.1** and **Figure 2.1**).
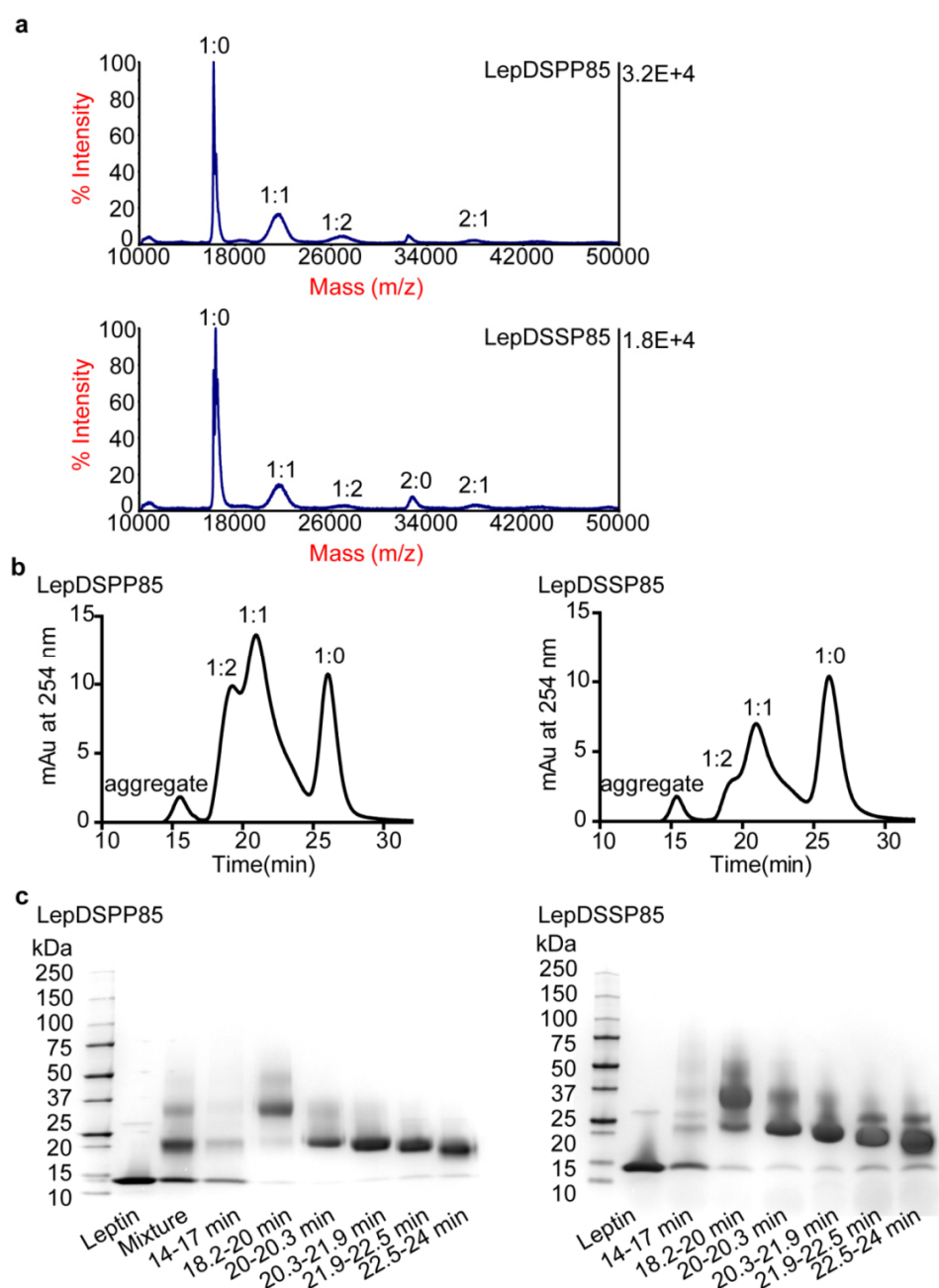
Figure 2.1. Purification and characterization of LepDSPP85 and LepDSSP85 conjugates. (a) MALDI-TOF spectra of the reaction mixture. The ratio denotes the molar ratio of leptin monomer to polymer. **(b)** SEC of acetone precipitated leptin conjugates eluted from Superdex75 100/300 GL column in 10% MeOH/0.25 M sodium phosphate, pH 7.5 at 0.5 ml/min. **(c)** SDS-PAGE of pooled fractions in SEC denoted by time. Pooled fractions of 20.3-21.9 min were relatively pure 1:1 conjugates.

Leptin N-terminal conjugation was accomplished via reductive amination based on the pKa difference between N-terminal amine (7.6-8.0) and lysine amine (9.3-9.5) [248]. Under acidic conditions, the lysine amines were preferentially protonated, leaving the unprotonated N-terminal amine reacting with aldehyde to form Schiff base, which was then reduced to a stable secondary amine by sodium cyanoborohydride (**Scheme 2.2a**). By this method, we synthesized leptin N-terminal conjugate modified with P85-aldehyde (CHO-P85-OH, prepared as shown in **Scheme 2.2b**) (LepNP85) or with commercial PEG5K-CHO of similar molecular mass (LepNPEG5K) at pH 5.5. The appearance in the MALDI-TOF spectra of a 21 kDa peak representing leptin monomer modified with a polymer chain (molar ratio of leptin monomer: polymer 1:1) and a 37 kDa peak representing leptin dimer modified with a polymer chain (2:1) in the reaction mixture (**Figure 2.2a**) indicated successful conjugation of leptin with CHO-P85-OH and PEG5K-CHO.

LepNP85 and LepNPEG5K were purified by SEC (**Figure 2.2b**). The fractions were characterized by MALDI-TOF (**Figure 2.3**) and SDS-PAGE (**Figure 2.2c**). Leptin conjugates and unmodified leptin were eluted sequentially based on their hydrodynamic size. The aggregates of large hydrodynamic size eluted in 14 to 17 min consisted of unmodified leptin (1:0, 16 kDa), singly modified leptin conjugate (1:1, 21 kDa), doubly modified leptin conjugate (1:2, 26 kDa), and heavily modified leptin conjugates (as indicated by the smear in SDS-PAGE [249]). Mixture of 1:2 and 1:1 conjugates was eluted in 18.2 to 20.3 min. A relatively pure fraction of 1:1 conjugate was eluted in 20.3 to 21.9 min. Mixture of 1:1 conjugate, leptin monomer modified by the diblock PEO-PPO (1:1*, 18 kDa), and unmodified leptin was eluted in 21.9 to 24 min. Lastly, unmodified leptin was eluted in 25 to 27 min. Commercial Pluronics including P85 from BASF typically contain about 10-25 *wt*% diblock PEO-PPO impurities [250]. We detected in

mono-amine-P85 synthesized from commercial P85 the presence of low-molecular mass

impurities (**Figure 2.4**), which should be separated prior to conjugation in subsequent improved

procedures. Compared to LepNP85, LepNPEG5K 1:1 conjugate had similar molecular mass (21

kDa) but was eluted earlier (18.5 vs. 21 min) in SEC, indicating their larger hydrodynamic size.

This is possibly due to greater swelling of the PEO chain attached to leptin in LepNPEG5K

compared to the P85 in LepNP85 in which a hydrophobic PPO block should form a more

condense structure. We carried out a molecular dynamics simulation and showed that the PEG

chain (5 kDa) in LepNPEG5K is loosely wrapped around leptin whereas P85 in LepNP85 is

compressed on the surface of leptin (**Figure 2.5**). In the following studies, we used purified 1:1

conjugates of LepDSPP85, LepDSSP85, LepNP85, and LepNPEG5K (**Figure 2.6**, chemical

structures are shown in **Scheme 2.3**).
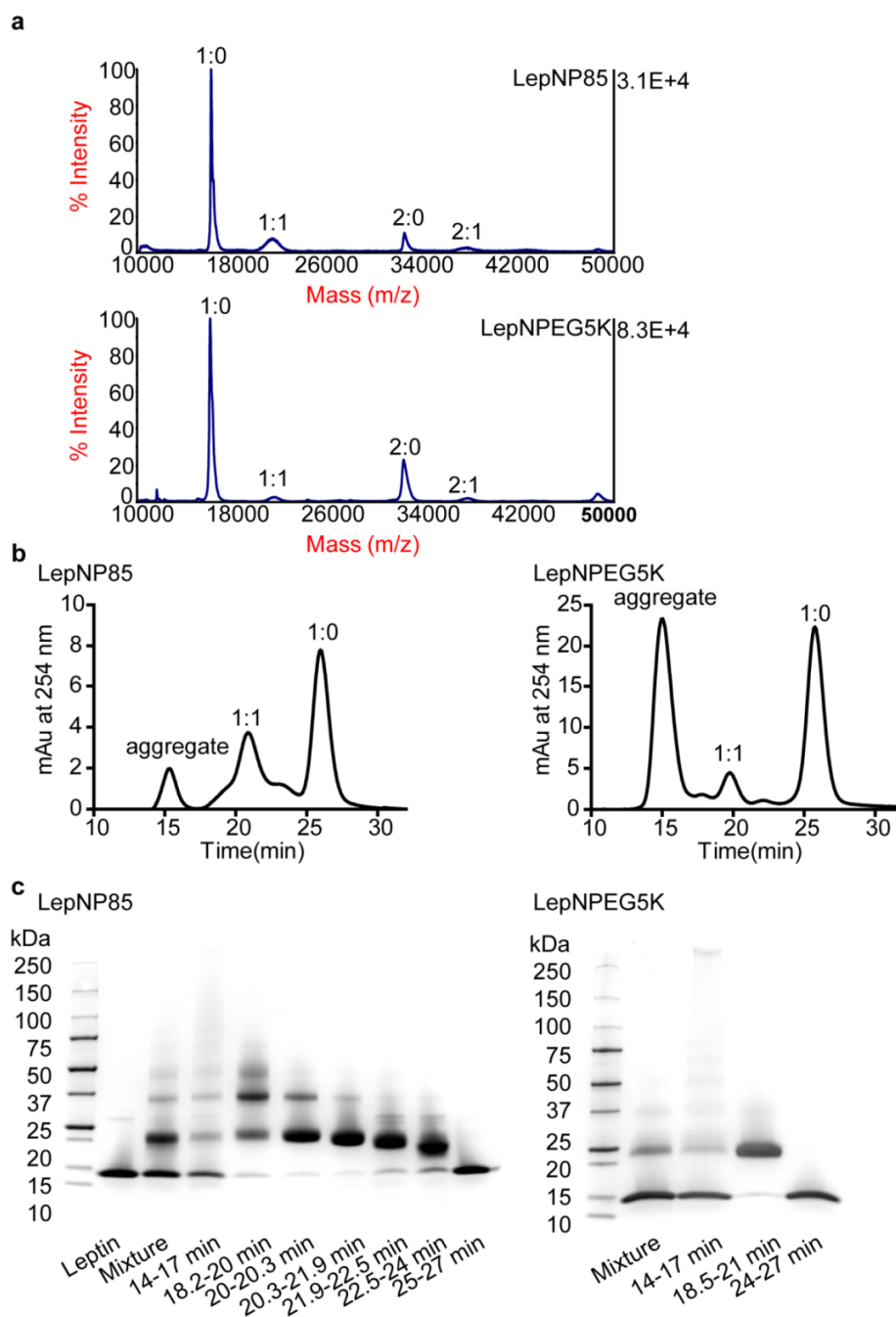
Figure 2.2. Synthesis, purification, and composition characterization of LepNP85 and LepNPEG5K. (a) MALDI-TOF spectra of reaction mixture. The ratio denotes the molar ratio of leptin monomer to polymer. **(b)** SEC of leptin conjugates eluted from Superdex75 100/300 GL column in 10% MeOH/0.25 M sodium phosphate, pH 7.5 at 0.5 ml/min. **(c)** SDS-PAGE of pooled fractions in SEC denoted by elution time. Fraction of 20.3-21.9 min in LepNP85 and fraction of 18.5-21 min in LepNPEG5K were used.
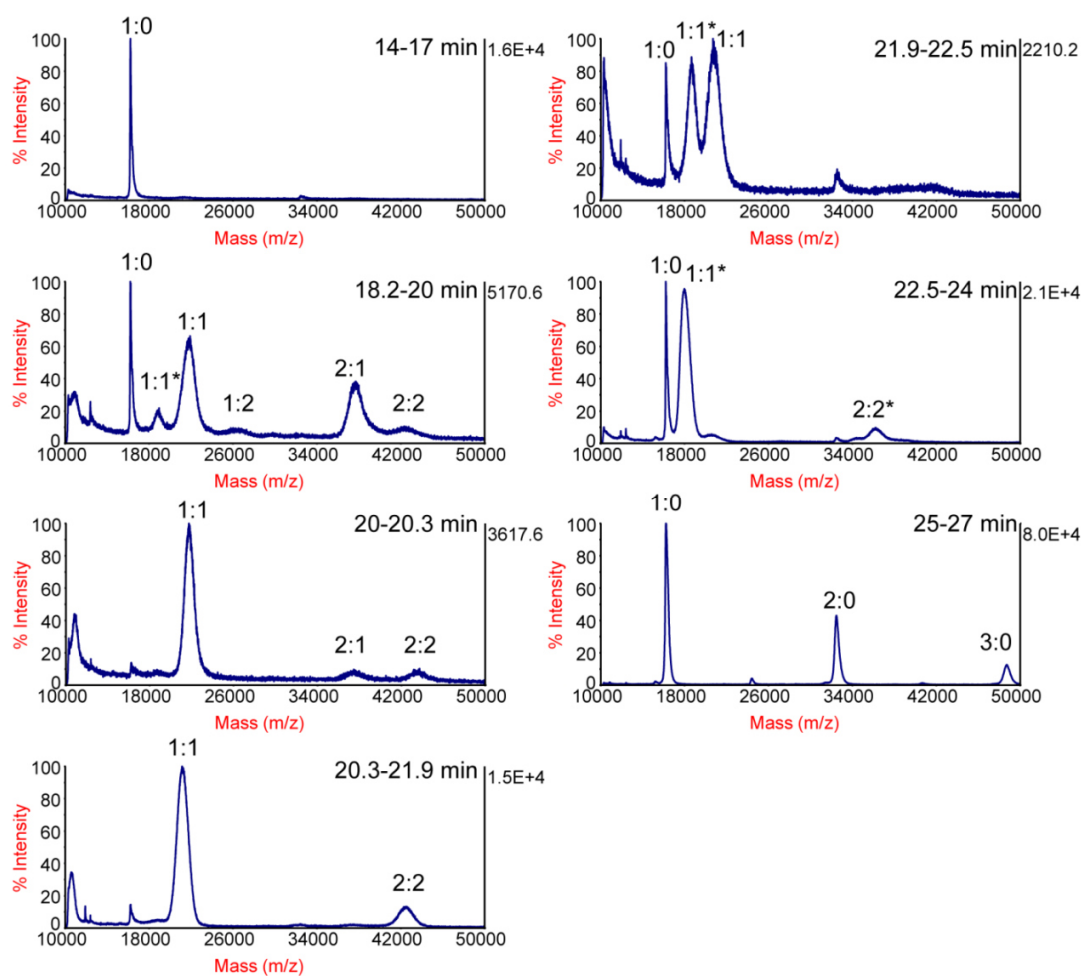
Figure 2.3. MALDI-TOF spectra of pooled fractions in the SEC of LepNP85. The ratio denotes molar ratio of leptin monomer to P85. * denotes modification by the P85 diblock impurity.
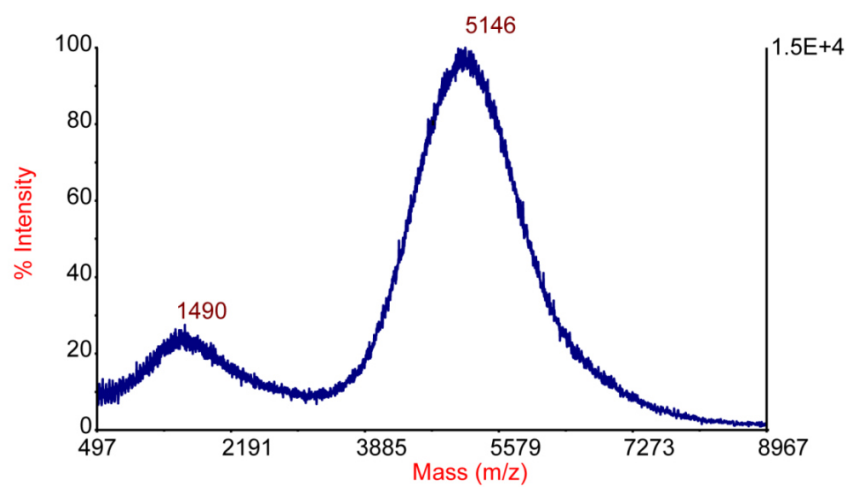
Figure 2.4. MALDI-TOF spectrum of mono-amine-P85. Mono-amine-P85 is a mixture of a triblock of MW ~5 kDa and a diblock of MW ~2 kDa.

LepNP85
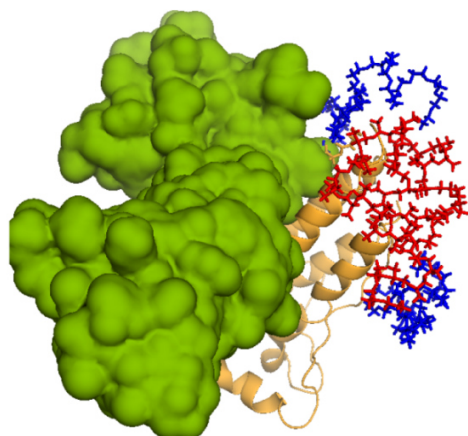
LepNPEG5K
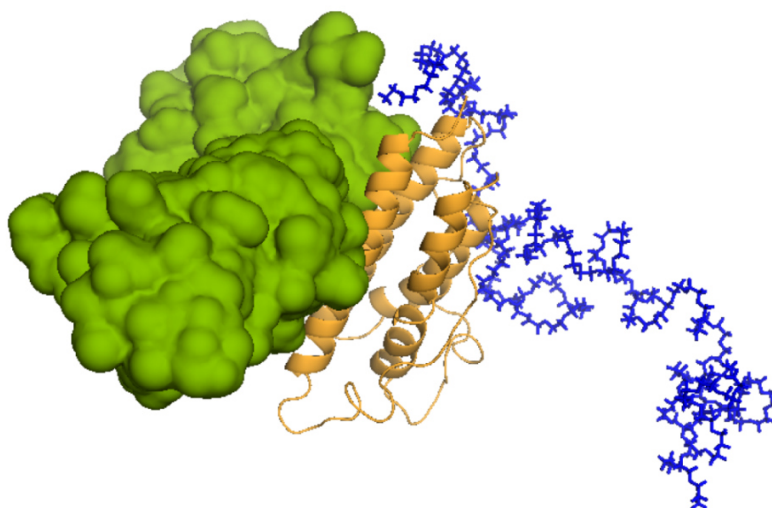
Figure 2.5. Structure of LepNP85 and LepNPEG5K and their alignment with leptin-binding domain (LBD). Green: LBD; gold: leptin; Blue: PEO block; Red: PPO block. The structure of LepNP85 and LBD was reproduced from [43] by molecular dynamics simulations (100 ns). The structure of LepNPEG5K and LBD was obtained similarly. The modeling results show that the P85 copolymer in LepNP85 and the PEG chain in LepNPEG5K do not sterically hinder the binding of leptin to LBD. The PEG chain (5 kDa) in LepNPEG5K is loosely wrapped around leptin whereas P85 in LepNP85 is compressed on the surface of leptin.
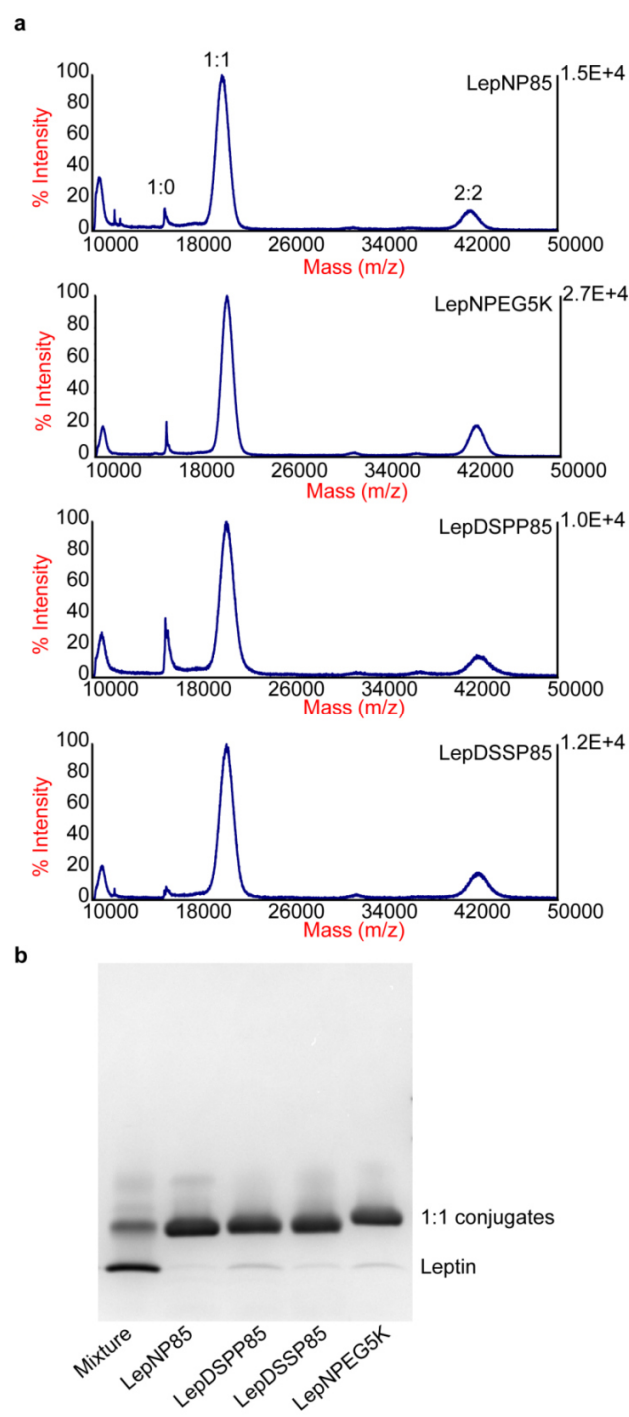
Figure 2.6. Mass spectra (a) and SDS-PAGE (b) of purified singly modified leptin conjugates.

LepNP85
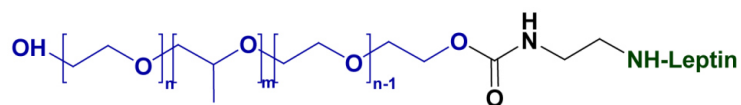
LepNPEG5K
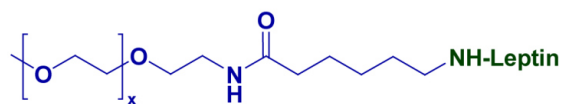
LepDSPP85
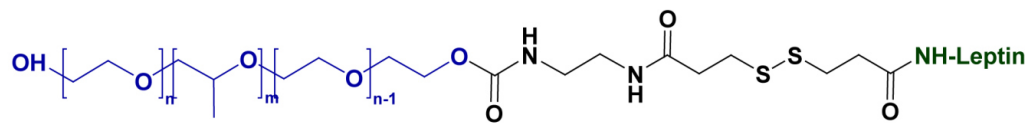
LepDSSP85
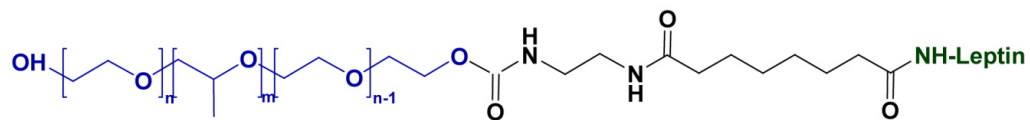
Scheme 2.3. Chemical structures of leptin conjugates.

2.3.2. N-terminal amino group protection analysis

To confirm that the CHO-P85-OH was attached at the N-terminal amino group of leptin, we protected this group with 2PCA [238] and then examined if the conjugation of leptin with CHO-P85-OH is affected. On average, each leptin molecule was modified with 0.76 ± 0.06 2PCA as determined by TNBSA assay. The modification resulted in an incremental increase of the molecular mass of the leptin monomer, dimer, and trimer by 129, 232, and 311 Da respectively, as determined by MALDI-TOF (**Figure 2.7**). This increase appears to be higher than expected (89, 178, and 267 Da respectively), which is due to the low accuracy of our MALDI-TOF analysis for the species with the mass-to-charge ratio exceeding 4000. Based on MALDI-TOF (**Figure 2.8**), the protection of the N-terminal amine nearly abolished the formation of LepNP85 1:1 conjugate, but did not impede the reaction of the protein with P85-DSP, which modifies leptin at multiple lysine amines [43]. This conclusion was reinforced by the SDS-PAGE (**Figure 2.9**), suggesting that the protection of the N-terminal amine greatly diminished the formation of 1:1 conjugate in the reaction of leptin with CHO-P85-OH, but did not affect the yield of such conjugate in the reaction with P85-DSP. This provides strong evidence of modification of N-terminal amine of leptin with CHO-P85-OH in LepNP85.
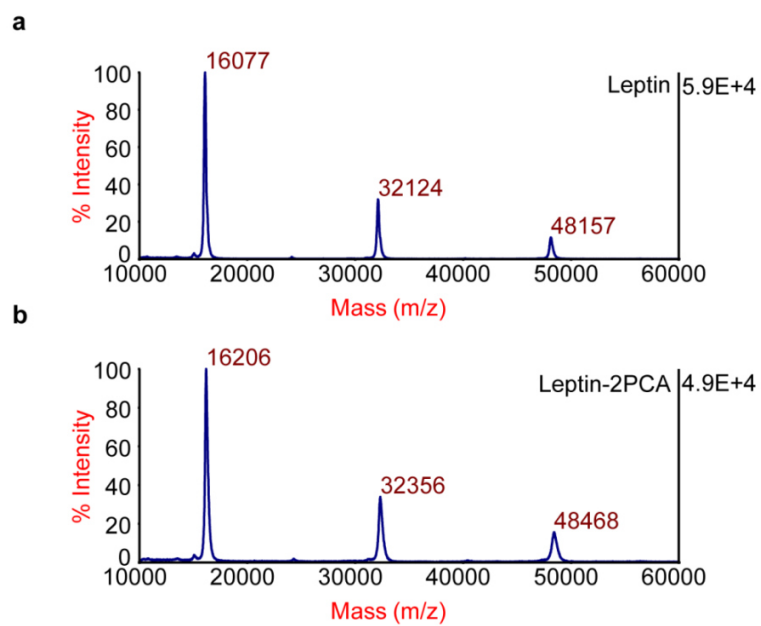
Figure 2.7. MALDI-TOF spectra of leptin before (a) and after (b) mixing with 2PCA. The proteins were mixed with excess of 2PCA in 0.1 M sodium borate, pH 8 at 37 °C for 24 h.
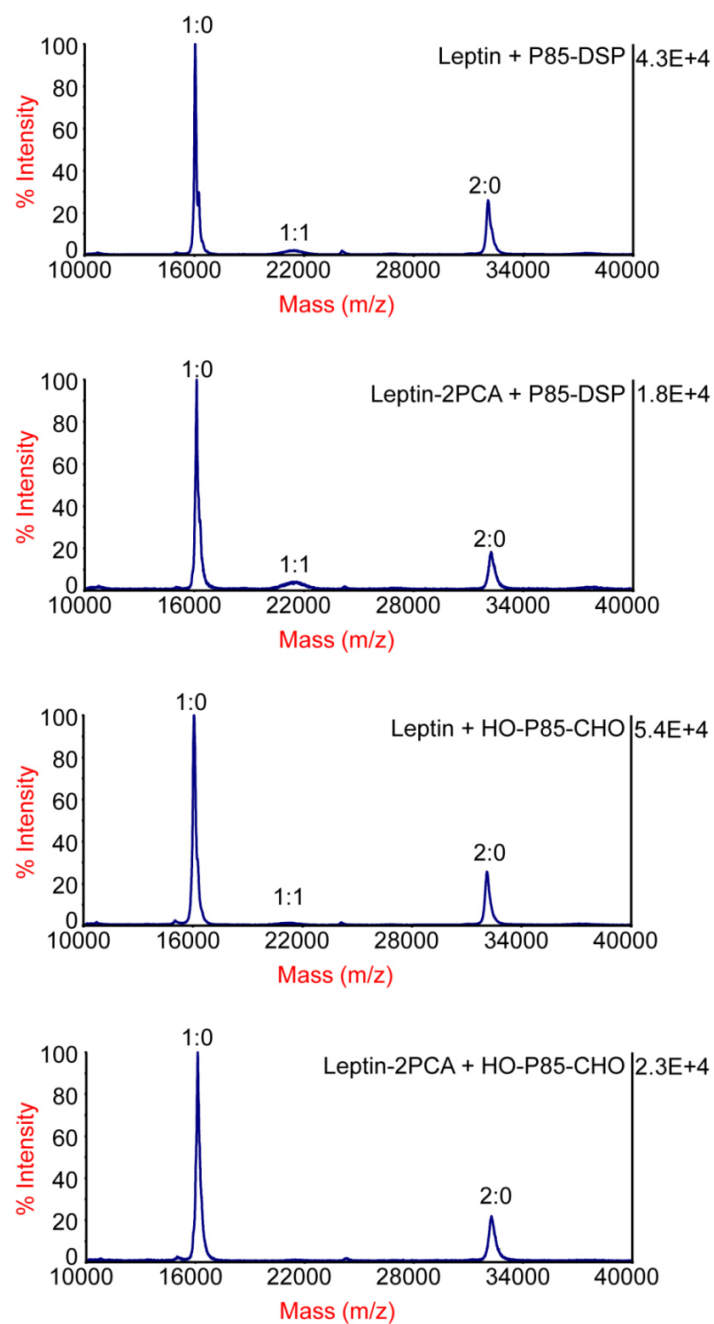
Figure 2.8. MALDI-TOF spectra of the reaction mixture of leptin and leptin-2PCA with P85-functionalized polymers.
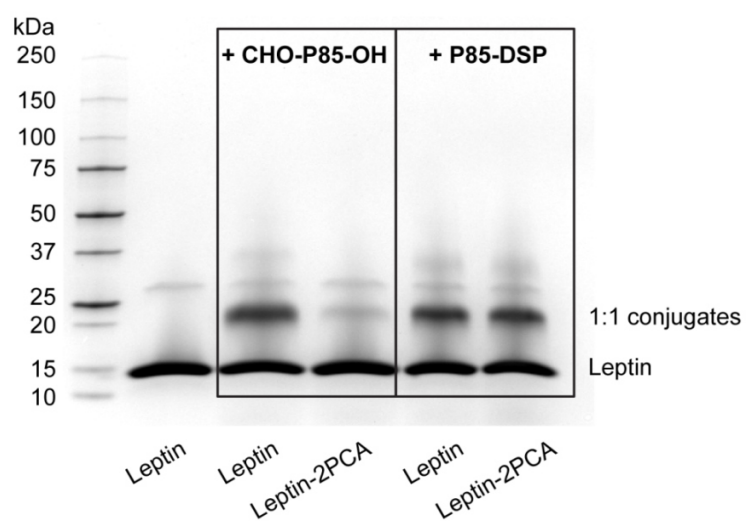
Figure 2.9. SDS-PAGE of the reaction mixture of leptin and Leptin-2PCA with CHO-P85-OH or with P85-DSP.

2.3.3. Secondary structures of the conjugates by CD

The secondary structures of leptin and leptin conjugates were characterized by far UV-CD (**Figure 2.10**). We also examined the CD spectra of the physical mixtures of native leptin with P85 or PEG5K to see if these polymers can have any effect on the conformation of the hormone *via* non-covalent interaction. The native leptin displayed a dominant α-helical structure (63%) as reported elsewhere [43, 251, 252]: two minima at 208 and 222 nm, and one maximum around 190 nm. The CD spectra of leptin in 1:1 physical mixture of leptin with P85 or PEG5K or covalent conjugates of leptin with these polymers were superimposed to that of native leptin. The results suggest that neither the physical mixture nor the covalent conjugation of the polymers perturb the secondary structure of leptin (see **Table 2.1** for compositions of secondary structure).
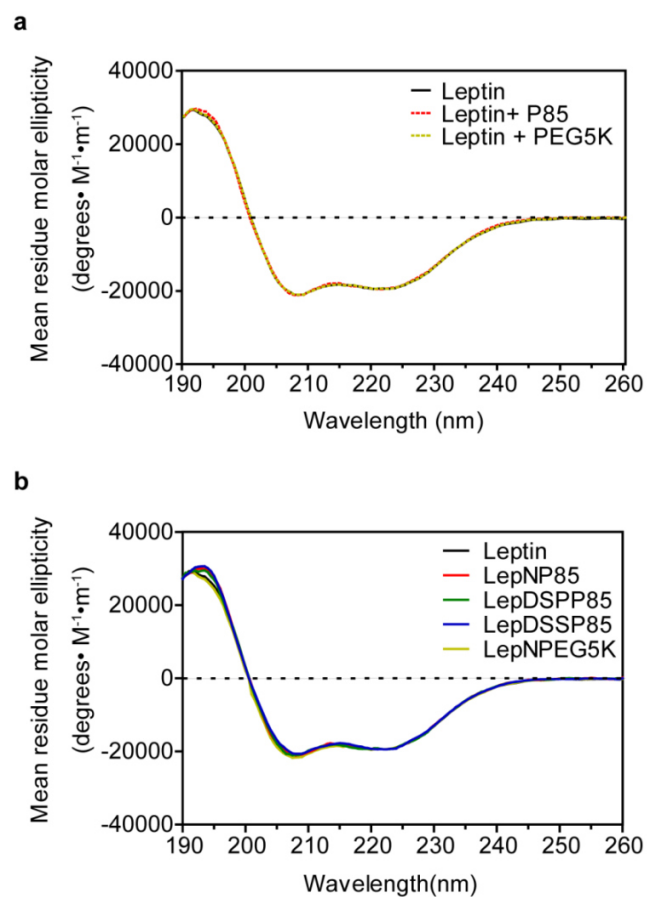
Figure 2.10. Far UV-CD spectra of leptin and leptin conjugates. (a) Leptin 1:1 physical mixture with P85 or PEG5K. **(b)** Leptin 1:1 conjugates.

Table 2.1. Secondary structures of leptin and leptin conjugates by CD.

Secondary Structures[a]	Leptin	Leptin + P85	Leptin + PEG5K	LepNP85	LepDSPP85	LepDSSP85	LepNPEG5K
a-helix	0.63	0.63	0.63	0.64	0.63	0.64	0.65
β-strand	0.06	0.06	0.04	0.04	0.04	0.04	0.06
Turns	0.11	0.12	0.12	0.13	0.13	0.11	0.09
Unordered	0.21	0.20	0.21	0.20	0.19	0.21	0.20
Total	1.01	1.01	1	1.01	0.99	1	1
NRMSD[b]	0.006	0.008	0.006	0.008	0.008	0.012	0.007

[a] Compositions of secondary structures were calculated by online DichroWeb CDSSTR program using protein reference set 7.
[b] NRSMD should be less than 0.1 [242, 253].

2.3.4. Relative hydrophobicity of the conjugates by RP-HPLC

The relative hydrophobicity of leptin and leptin conjugates was compared by RP-HPLC using a gradient of acetonitrile + 0.1% TFA: isopropanol 50:50 (*v/v*) (**Figure 2.11**). As seen in the figure, leptin modified with a single chain of PEG5K (LepNPEG5K) was eluted at nearly the same concentration of organic solvents as the unmodified leptin, suggesting that this conjugate had similar hydrophobicity to the native protein. As expected, leptin modified with a single chain of P85 (both LepNP85 and LepDSPP85) were eluted at higher concentration of organic solvents than the unmodified leptin and PEGylated analog, which was consistent with their increased hydrophobicity due to incorporation of the hydrophobic PPO block. Notably, despite the increased hydrophobicity of the leptin-P85 conjugates, we did not observe aggregation or formation of micelle-like structures of the conjugates in aqueous solution. We characterized the intensity-based size distribution of leptin and LepNP85 at protein concentration of 1 mg/ml (**Figure 2.12**). Interestingly, LepNP85 had lower polydispersity index (PDI) and less aggregation than native leptin. Each sample exhibited a main fraction of small particles with an effective diameter of 5.3 nm for leptin and 8.2 nm for LepNP85, which is much smaller than the typical diameter of P85 micelles (around 16 nm [254]).
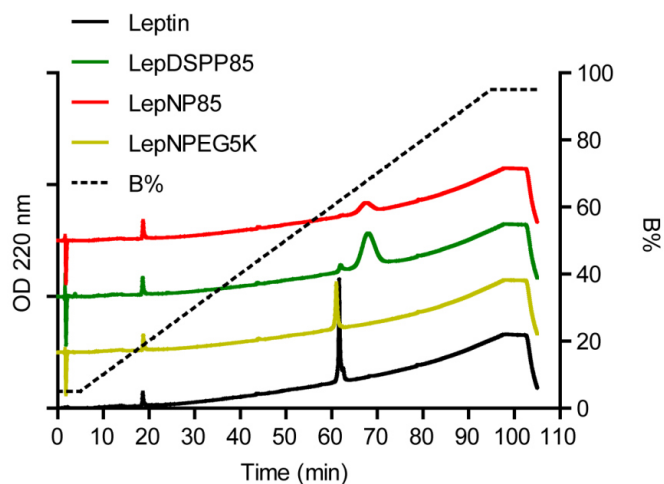
Figure 2.11. RP-HPLC analysis of leptin and leptin conjugates. Leptin and leptin 1:1 conjugates were eluted from Jupiter C4 column (particle diameter 5 μm, pore diameter 300 Å, 4.6 x 100 mm) by gradient elution at 1 ml/min and 25 °C, and monitored by absorption at 220 nm. Mobile phase A: water + 0.1% TFA; mobile phase B: acetonitrile + 0.1% TFA: isopropanol 50:50 (*v/v*). The elution started from 5% B for 5 min, then linearly increased to 95% B at 1%/min, and stayed at 95% B till 100 min.
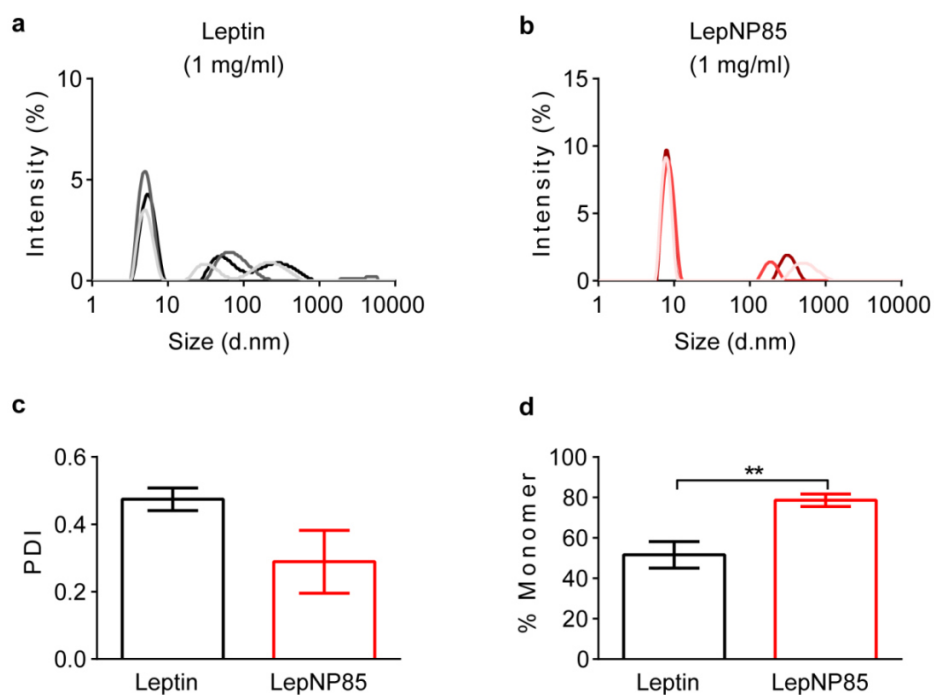
Figure 2.12. Size distribution of leptin and LepNP85 by DLS. The size measurements were carried out at protein concentration of 1 mg/ml at 25°C. Three repeated measurements are shown in gradient colors for each protein. Data are mean ± SD, n = 3, ** $p < 0.01$ by unpaired two-sided t-test.

2.3.5. Binding affinity of the conjugates by SPR

Next, we characterized the binding of leptin and leptin conjugates to leptin receptor by SPR (**Figure 2.13**). Native leptin displayed the fast binding and slow dissociation and had a dissociation constant (K_D) of 0.089 ± 0.046 nM, which was similar to the previously reported value (0.12 ± 0.08 nM) [243]. Leptin N-terminal conjugates LepNP85 and LepNPEG5K had similar sensorgrams and dissociation constants (0.20 ± 0.13 nM for LepNP85 and 0.28 ± 0.15 nM for LepNPEG5K). These K_D values were numerically (~2 to 3 times) higher but not statistically different compared to that of the native leptin. In contrast, the random lysine conjugates LepDSPP85 and LepDSSP85 displayed much faster dissociation rates and over ten times higher dissociation constants (1.09 ± 0.23 nM for LepDSPP85 and 1.08 ± 0.24 nM for LepDSSP85). These K_D values were significantly different compared to that of the native leptin. Therefore, consistent with the molecular dynamics prediction [43], the binding affinity (inverse to K_D) determined by SPR was only marginally affected in leptin N-terminal conjugates, but greatly decreased in the random lysine conjugates. Since we determined that the conjugation did not affect the conformation of leptin, the observed changes in binding of the leptin conjugates to the receptor are most likely due to steric hindrance of such binding by the attached polymer chains.
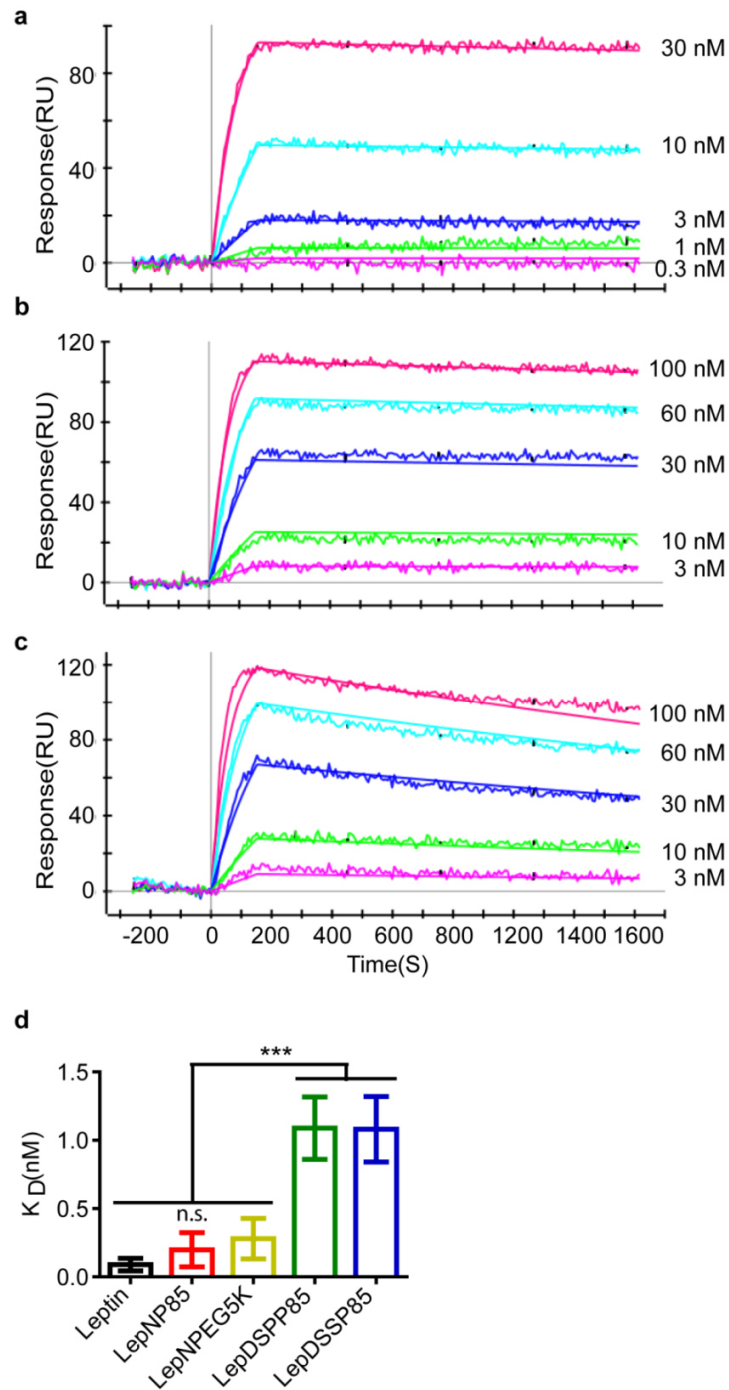
Figure 2.13. Binding affinity of leptin and leptin conjugates to leptin receptor by SPR. (a) Representative sensorgram for native leptin. **(b)** Representative sensorgram for LepNP85 1:1 conjugates. **(c)** Representative sensorgram for LepDSSP85 1:1 conjugates. **(d)** Dissociation constants (K_D) of leptin and leptin 1:1 conjugates. Data are mean ± SD, n = 5-12. *** $p < 0.001$ and n.s. not significant by One-way ANOVA and post Newman-Keuls Multiple Comparison Test.

2.3.6. Leptin receptor activation in hypothalamus after ICV injection

Leptin regulates appetite mainly by binding to its receptor in the hypothalamus and activating the downstream janus kinases-STAT3 (JAK-STAT3) pathway [221, 255]. To determine if leptin conjugates are active *in vivo*, we injected the leptin and leptin conjugates to the brain by ICV administration, and then sampled hypothalamus for western blotting (**Figure 2.14**). The pSTAT3 to total STAT3 ratio (pSTAT3/STAT3) served as a measure of leptin receptor activation [203, 256]. 30 min after ICV administration of native leptin at a dose of 100 ng/mouse, this ratio was significantly higher than the one observed after the injection of the vehicle (**Figure 2.14a**). Further increase of leptin dose to 500 and 1000 ng/mouse did not produce any significant change in pSTAT3/STAT3 ratio. LepNP85 displayed essentially the same activity as native leptin, producing nearly the same pSTAT3/STAT3 ratios at the same doses of 100, 500, and 1000 ng/mouse (**Figure 2.14a**), suggesting signal saturation at the dose of at least 100 ng/mouse. Next, we compared all leptin conjugates to native leptin at a dose of 100 ng/mouse and concluded that they all have similar activities as the native leptin (**Figure 2.14b**). It is likely that we cannot detect the differences between these forms as seen in SPR due to signal saturation at this dose and the large animal variability such as receptor expression on plasma membrane, downstream signaling, and diffusion of proteins from injection sites to hypothalamus [257], which reduce the experimental space for us to detect the difference at lower doses. Nonetheless, these data suggest that all leptin conjugations produced in this study were active in live brain.
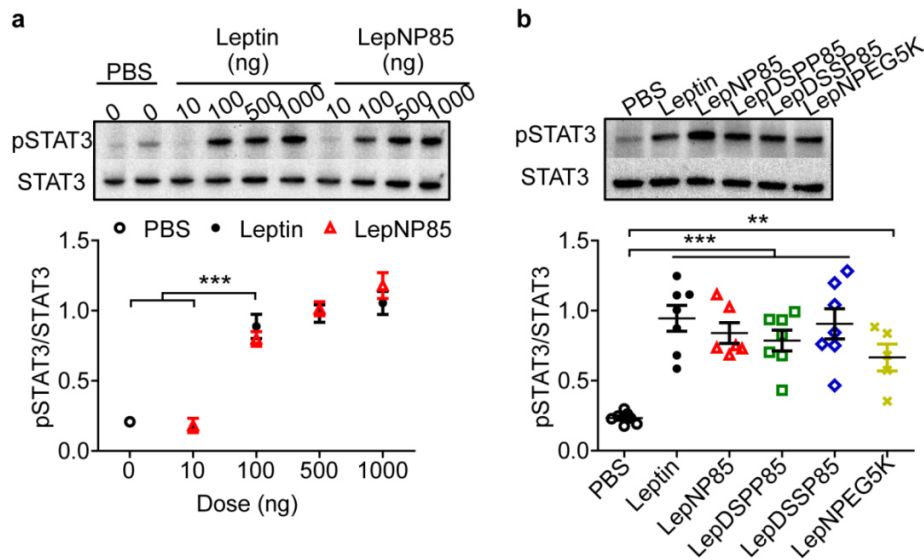
Figure 2.14. Phosphorylation of STAT3 in hypothalamus 30 min after ICV injection of leptin and leptin conjugates. (a) Dose response of leptin and LepNP85 1:1 conjugates. Data are mean ± SEM, n = 3. **(b)** Comparison of leptin and leptin 1:1 conjugates at 100 ng/mouse. Data are mean ± SEM, n = 5-7. ** $p < 0.01$ and *** $p < 0.001$ by One-way ANOVA and post Newman-Keuls Multiple Comparison Test.

2.3.7. Serum clearance and brain influx rates after IV injection

To characterize serum clearance and brain influx rate following IV administration, we labeled leptin and leptin conjugates with ^{125}I and ^{131}I respectively, and co-injected them into the left jugular veins of CD1 mice. The half-life of serum clearance was calculated from the linear portion of the regression of Ln serum concentration against time (**Figure 2.15** and **Table 2.2**). Similar to previously reported results for LepDSPP85 [43], LepNP85, LepDSSP85 and LepNPEG5K showed two-phase decay of serum clearance and prolonged half-life of 50.58-57.04 min compared to leptin (~11.41 min). The unidirectional brain influx rate (Ki) and the initial volume of brain distribution (Vi) were calculated using multiple-time regression analysis (**Table 2.2**). Vi included the vascular space and steady-state exchangeable space that was quickly equilibrated with the blood, such as rapid reversible transporter binding at the brain endothelial cells [246, 258]. The brain influx rate of native leptin was similar to the value reported previously (0.236 µl/g·min) [43]. LepNP85 displayed ~3.5-times lower brain influx rate and slightly lower initial volume of brain distribution compared to co-injected native leptin. We further compared LepNP85 to non-cleavable random lysine-modified conjugate, LepDSSP85. (We did not include in this study a cleavable analog, LepDSPP85 that was evaluated previously [43] to avoid any interference of the disulfide bond reduction and decrease the animal use.) Compared to LepDSSP85, LepNP85 displayed a trend of having ~1.5-time faster brain influx rate ($p = 0.05718$) and slightly albeit significantly higher initial volume of brain distribution. We also compared LepNP85 to the N-terminal PEGylated analog LepNPEG5K and revealed great similarity between these analogs. LepNPEG5K and LepNP85 had similar brain influx rates ($p = 0.8965$) and volumes of brain distribution (p

= 0.4086). Taken together, these results suggest that the N-terminal leptin conjugates with P85 or PEG5K are slightly superior in terms of brain delivery to the random lysine conjugate by IV injection. However, brain entry of LepNP85 was inhibited by co-injection of cold leptin (**Figure 2.16**), suggesting it cannot overcome the leptin peripheral resistance in obesity. Therefore, we administered LepNP85 intranasally using the INB route to bypass the peripheral resistance of leptin transporter.
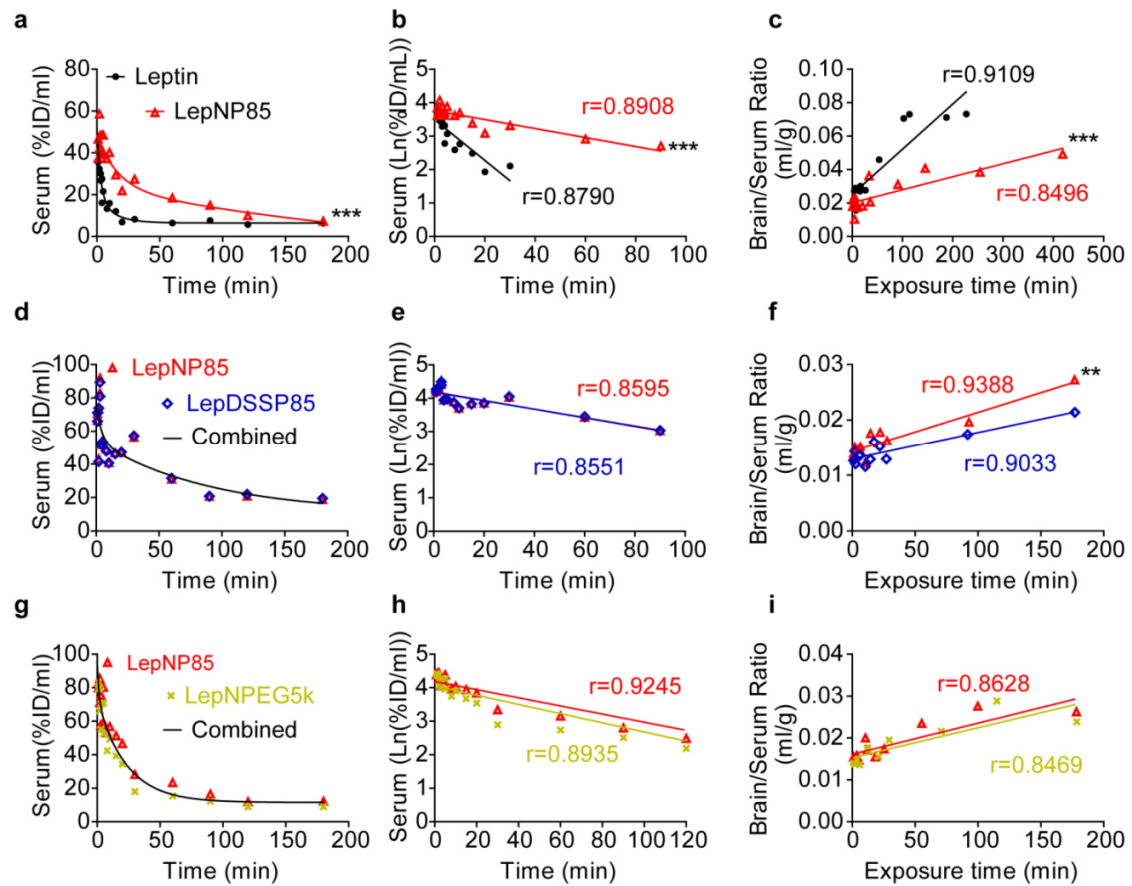
Figure 2.15. Serum clearance and unidirectional brain influx rate of leptin and leptin conjugates. In each row, the two compounds were labeled with ^{125}I and ^{131}I respectively and co-injected into CD-1 mice by IV injection. **(a, d, g)** Serum concentration over time. **(b, e, h)** Linear regression of serum concentration. **(c, f, i)** Multiple-time regression analysis for unidirectional brain influx rate. n = 1-2/time point, **$p < 0.01$ and ***$p < 0.001$ by two-way ANOVA.

Table 2.2. Clearance, unidirectional brain influx rates and initial volumes of brain distribution for leptin and leptin 1:1 conjugates.

	Leptin vs. LepNP85[a]		LepNP85 vs. LepDSSP85[a]		LepNP85 vs. LepNPEG5K[a]	
	Leptin	LepNP85	LepNP85	LepDSSP85	LepNP85	LepNPEG5K
$t_{1/2}$, min	11.42	51.52	53.38	54.52	57.04	50.58
Ki, ml/(min · g)	0.270 ± 0.004	0.078 ± 0.001***	0.071 ± 0.009	0.048 ± 0.007	0.074 ± 0.015	0.072 ± 0.015
Vi, ml/g	25.18 ± 0.35	20.17 ± 0.19	14.31 ± 0.53	12.94 ± 0.43**	16.11 ± 0.94	15.29 ± 1.03

[a] Pairs were labeled respectively with ^{125}I and ^{131}I and co-injected into mice by IV administration. $t_{1/2}$, Ki, and Vi were calculated from **Figure 7**, **$p < 0.01$ and ***$p < 0.001$ by two-way ANOVA.
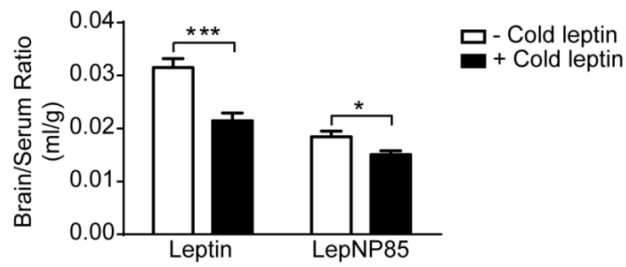
Figure 2.16. Inhibition of cold leptin on brain uptake of leptin and LepNP85. Male CD-1 mice were co-injected with ^{125}I-LepNP85 and ^{131}I-leptin with or without cold leptin (10 µg/mouse) into the jugular vein. Data are mean ± SEM, n = 10, * $p < 0.05$ and *** $p < 0.001$ by unpaired two-sided t-test.

2.3.8. Serum absorption and distribution after intranasal administration

2.3.8.1. Comparison of leptin and LepNP85

We examined whether Pluronic modification could improve INB delivery of leptin to the brain. Towards this goal, we co-administered ^{125}I-LepNP85 and ^{131}I-leptin into the upper nasal area near cribriform plate [205]. INB delivery of leptin in a rat model follows the traditional pattern of uptake by the olfactory bulb with less amounts of uptake by other brain regions and with little material entering blood [247]. Consistent to this report, the serum absorption of both leptin and LepNP85 increased over time (**Figure 2.17**). The AUC of serum concentration (%ID/ml) over the first 60 min for LepNP85 was ~1.5-times of that for co-injected leptin (**Table 2.3**), suggesting that the copolymer modification enhanced the serum absorption of LepNP85. However, the serum concentration of LepNP85 was still quite low (1.7%ID/ml at 60 min). Accordingly, the distribution of leptin and LepNP85 in peripheral organs was minimal and increased over time as the serum concentration increased (**Figure 2.18**). Notably, the lungs, which were supplied with iodinated proteins from blood and nose, had significantly higher accumulation compared to the other peripheral organs that had blood as the only source for iodinated proteins.
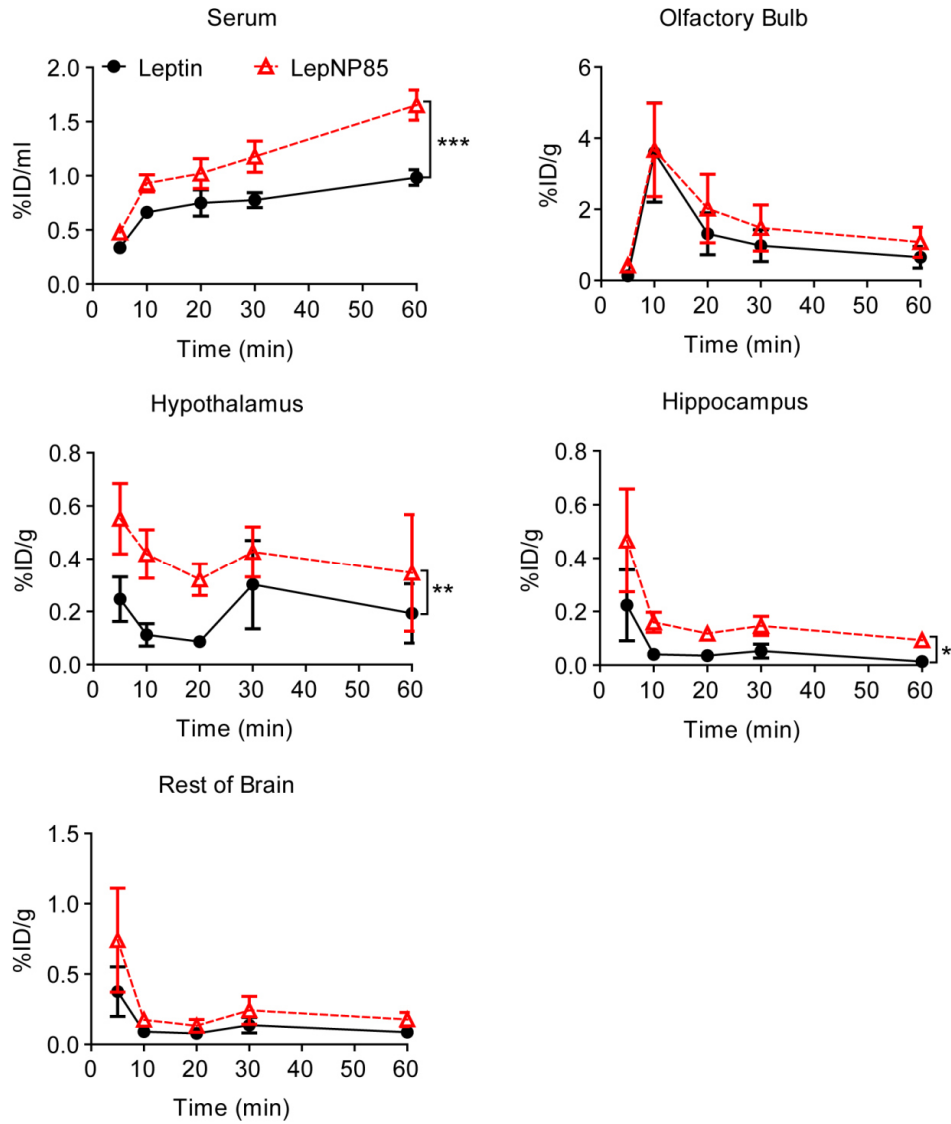
Figure 2.17. Serum absorption and brain regional distribution of intranasally delivered leptin and LepNP85 1:1 conjugate. Male CD-1 mice were co-injected with ^{125}I-LepNP85 and ^{131}I-leptin. Data are mean ± SEM, n = 7/time point, * $p < 0.05$, ** $p < 0.01$, and *** $p < 0.001$ by Two-way ANOVA.

Table 2.3. AUC of leptin and leptin conjugates by INB delivery.

	Leptin vs. LepNP85[a]		LepNP85 vs. LepNPEG5K[a]		LepNP85 vs. LepDSPP85[a]		LepNP85 vs. LepDSSP85[a]	
	Leptin	LepNP85	LepNP85	LepNPEG5k	LepNP85	LepDSPP85	LepNP85	LepDSSP85
Serum	43.56	66.71***	84.65	35.57***	48.84	72.71***	114.5	68.94
Olfactory bulb	69.82	94.46	37.84	21.64*	32.38	33.69	51.08	24.10
Hypothalamus	11.27	21.45**	11.94	4.83*	8.81	2.52**	13.09	7.24
Hippocampus	2.47	7.85*	6.44	2.04***	3.17	0.600***	6.95	3.59

[a] Pairs were labeled respectively with ^{125}I and ^{131}I and co-injected into mice by INB. AUCs were calculated from **Figure 2.17**, **2.19**, **2.20**, and **2.21**. N = 7/time point, *$p < 0.05$, **$p < 0.01$, and ***$p < 0.001$ by Two-way ANOVA.
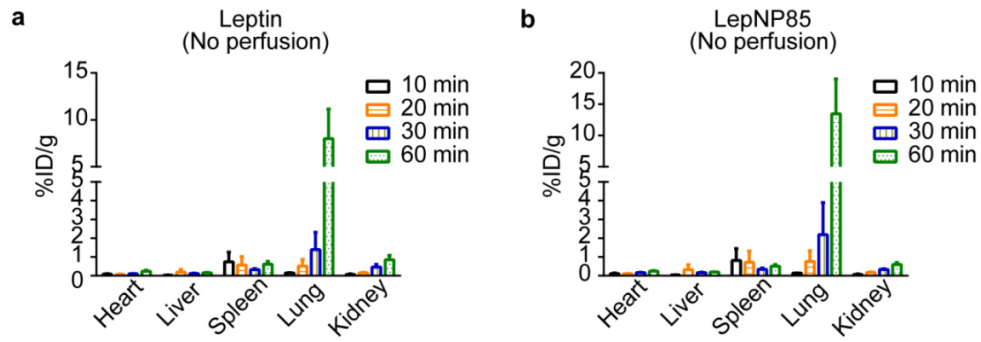
Figure 2.18. Peripheral distribution of leptin (a) and LepNP85 (b) in healthy mice by INB delivery. The mice were intranasally injected with ^{131}I-leptin and ^{125}I-LepNP85. At defined time points, the peripheral organs were sampled without perfusion. Data are mean ± SEM, n = 4.

The brain distribution pattern of both LepNP85 and native leptin was also similar to that reported for intranasal leptin in rat [247]: the highest concentration was observed in olfactory bulb, followed by hypothalamus and then hippocampus, which was comparable to the rest of brain (**Figure 2.17**). Compared to co-injected leptin, LepNP85 had similar accumulation in olfactory bulb, but 1.9-times higher AUC in hypothalamus and 3.2-times higher AUC in hippocampus over the first 60 min. This result was further reinforced by the PK study in DIO mice model suggesting that LepNP85 accumulated in the brain hypothalamus and hippocampus better than the unmodified leptin (**Figure 2.18a**). Brain distribution of intranasal LepNP85 did not differ between healthy mice and DIO mice (**Figure 2.18b**). These data support our hypothesis that Pluronic modification enhanced INB delivery of leptin.
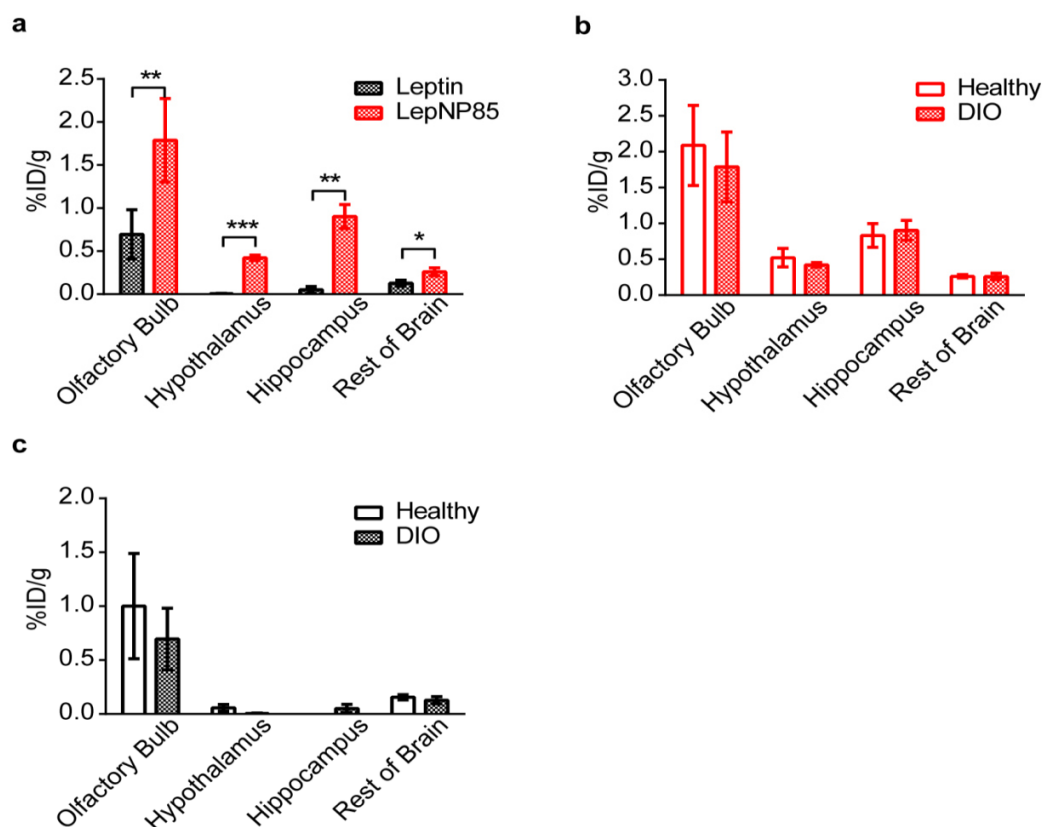
Figure 2.18. Brain distribution of leptin and LepNP85 in healthy and DIO mice after INB delivery. (a) Brain distribution of intranasally administered ^{131}I-leptin and ^{125}I-LepNP85 in DIO mice at 10 min. The DIO mice model was established by feeding male CD-1 mice (7 weeks of age at purchase) with a 60% high-fat diet (D12492; Research Diets, Inc., New Brunswick, NJ) for 8 months prior to use. **(b)** Comparison of the brain distribution of LepNP85 in healthy and DIO mice at 10 min post INB delivery. **(c)** Comparison of the brain distribution of leptin in healthy and DIO mice at 10 min post INB delivery. Data are mean ± SEM, n = 5. * $p < 0.05$, ** $p < 0.01$ and *** $p < 0.001$ by paired two-sided t-test.

2.3.8.2. Comparison of LepNP85 and LepNPEG5K

To explore the function of hydrophobic PPO block in P85, we compared LepNP85 to LepNPEG5K. LepNP85 accumulated 2.4-times more in serum, 1.7-times more in olfactory bulb, 2.5-times more in hypothalamus, and 3.2-times more in hippocampus than co-injected LepNPEG5K (**Figure 2.19**), suggesting that the PPO block in LepNP85 facilitates serum absorption and intranasal delivery to the brain. Note that leptin, LepNP85, and LepNPEG5K demonstrated similar integrity in serum and brain samples after intranasal administration as determined by TCA precipitation (**Table 2.4**), suggesting the above comparisons of total radioactivity represent the comparisons of intact proteins.

Figure 2.19. Serum absorption and brain distribution of intranasally delivered 1:1 conjugates of LepNP85 and LepNPEG5K. Male CD-1 mice were co-injected with ^{125}I-labeled LepNP85 and ^{131}I-labeled LepNPEG5K. Data are mean ± SEM, n = 7/ time point, * $p < 0.05$ and *** $p < 0.001$ by Two-way ANOVA.

Table 2.4. Stability of iodinated leptin and leptin conjugates in serum and brain following INB delivery.

Tissue	Sample	10 min		60 min		Process control[c]	
		Mean	SD	Mean	SD	Mean	SD
Brain[a]	Leptin	67.80%	12.80%	55.10%	9.70%	97.20%	0.30%
	LepNP85	60.40%	9.60%	57.40%	7.40%	96.20%	0.80%
Serum[a]	Leptin	56.30%	13.00%	62.10%	6.90%	98.00%	0.10%
	LepNP85	57.40%	7.40%	67.30%	7.60%	97.30%	0.40%
Brain[b]	LepNPEG5K	75.20%	12.20%	86.90%	10.70%	96.40%	0.10%
	LepNP85	79.00%	10.50%	87.00%	10.80%	95.40%	0.60%
Serum[b]	LepNPEG5K	53.40%	14.10%	63.60%	24.40%	97.30%	0.30%
	LepNP85	53.80%	16.80%	60.30%	23.00%	96.40%	1.20%

[a] The mice were dosed intranasally with ^{125}I-LepNP85 and ^{131}I-Leptin. n = 5.
[b] The mice were dosed intranasally with ^{125}I-LepNP85 and ^{131}I-LepNPEG5K. n = 5.
[c] The blank serum and brain samples were spiked with iodinated proteins and then treated similarly as serum and brain samples from dosed animal. n = 5.

2.3.8.3. Comparison of LepNP85, LepDSPP85, and LepDSSP85

Next, we compared LepNP85 to the previously developed LepDSPP85. Interestingly, LepNP85 had 0.7-time lower serum absorption, similar accumulation in OB, 3.5-times higher accumulation in hypothalamus, and 5.3-times higher accumulation in hippocampus (**Figure 2.20**). The reduced serum absorption and increased brain accumulation indicated that LepNP85 was superior to LepDSPP85. The difference between LepNP85 and LepDSPP85 in INB delivery cannot be explained by the difference in modification sites, because LepNP85 and LepDSSP85 had similar serum absorption and brain distribution after INB delivery (**Figure 2.21**). These suggest that the difference between LepNP85 and LepDSPP85 was mainly due to the reduction of disulfide bond in LepDSPP85. Taken together, LepNP85 is the best conjugate that accumulated most in brain hypothalamus and hippocampus by intranasal delivery.
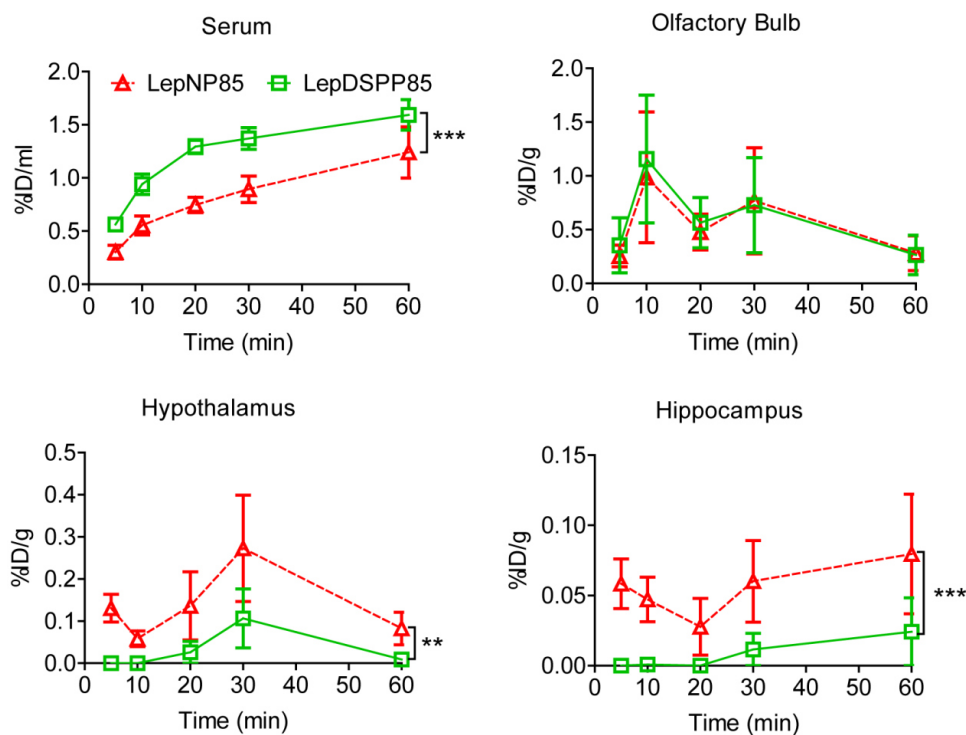
Figure 2.20. Serum absorption and brain regional distribution of intranasally delivered 1:1 conjugates of LepNP85 and LepDSPP85. Male CD-1 mice were co-injected with ^{125}I-labeled LepNP85 1:1 conjugates and ^{131}I-labeled LepDSPP85 1:1 conjugates. Data are mean ± SEM, n = 7/time point, ** $p < 0.01$ and *** $p < 0.001$ by Two-way ANOVA.
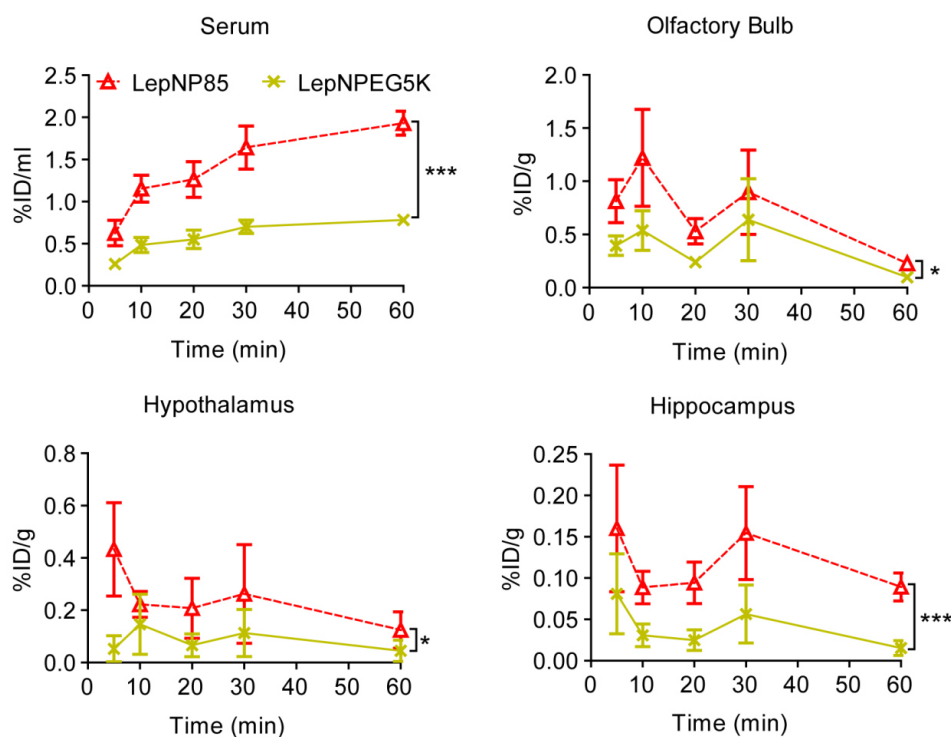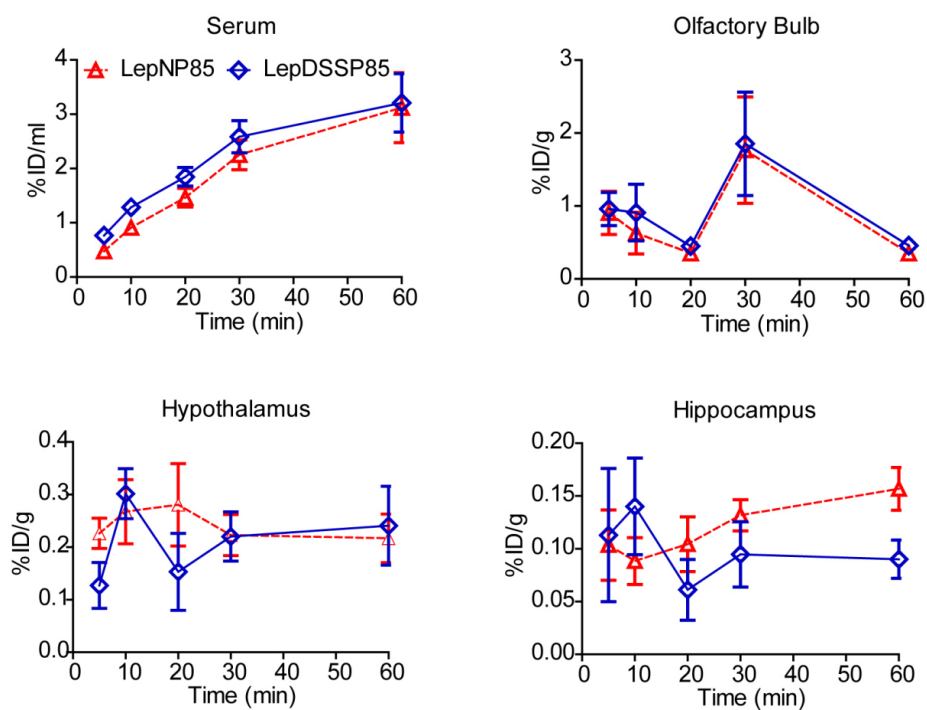
Figure 2.21. Serum absorption and brain regional distribution of intranasally delivered 1:1 conjugates of LepNP85 and LepDSSP85. Male CD-1 mice were co-injected with ^{125}I-LepNP85 conjugates and [131]I- LepDSSP85 conjugates. Data are mean ± SEM, n = 7/time point, no significant difference by Two-way ANOVA.

2.3.8.4. Brain/ serum ratios of leptin and leptin conjugates

The brain/serum ratios for leptin and leptin conjugates after INB delivery were calculated by summing radioactivity of hypothalamus, hippocampus, and the rest of brain (**Figure 2.22**). These values for all the conjugates were generally one order higher than the respective brain/serum ratios observed after IV administration. For the native leptin, the difference was somewhat less suggesting possibility of at least partial reabsorption of the hormone from the blood to the brain.
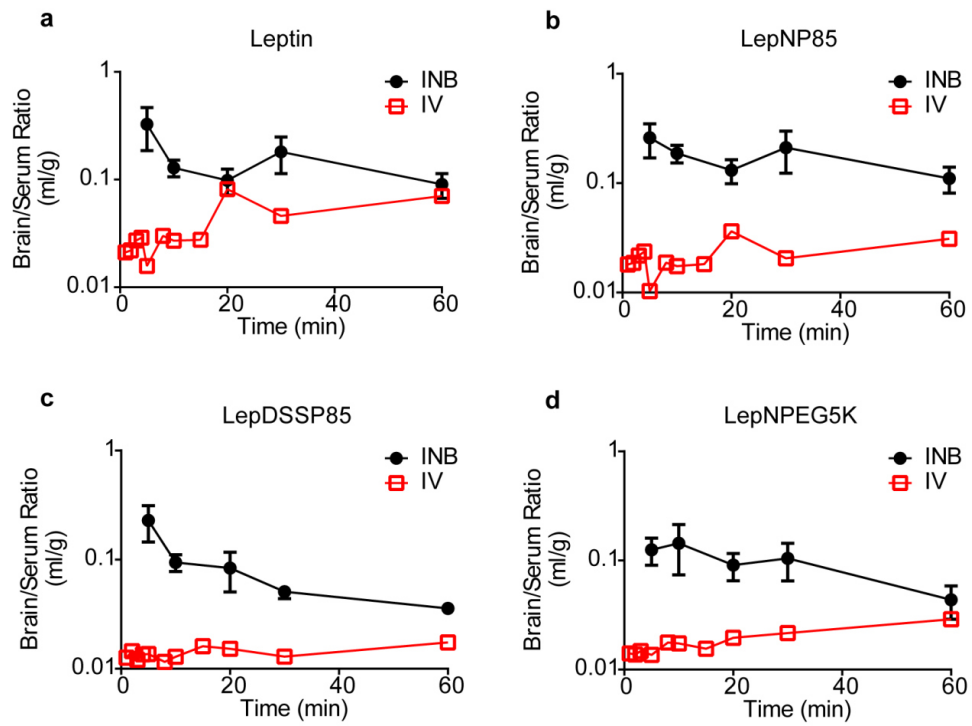
Figure 2.22. Brain/serum ratios of native leptin and leptin conjugates after INB and IV administration. (a) Leptin. **(b)** LepNP85. **(c)** LepDSSP85. **(d)** LepNPEG5K. Data are from **Figure 15**, **17**, **19**, and **21**.

2.3.8.5. Competitive effect of leptin on distribution of the conjugate

Fliedner, et al. reported that in a rat model the intranasal delivery of leptin to the brain is non-saturable although the serum absorption of the protein is saturable [247]. Specifically, co-injection of iodinated leptin with unlabeled leptin (0.2 mg/kg in ~600 g rats, which according to another paper is a therapeutic dose [185]) did not affect the amount of the labeled protein distributed in the brain (including olfactory bulb, hypothalamus and hippocampus) but distribution of this protein in the serum. We obtained similar result in our mouse study for LepNP85 conjugate. In this case, co-administration of the conjugate with unlabeled leptin (10 µg/mouse or 0.4 mg/kg in ~25 g mice) significantly decreased serum absorption of the conjugate, and did not inhibit its uptake in olfactory bulb, hypothalamus, and hippocampus over the first 30 min after INB delivery (**Figure 2.23**). This suggests that although the brain distribution of the LepNP85 appears to be receptor-independent, the serum distribution is still mediated by a saturable system that recognizes both the native leptin and this conjugate.
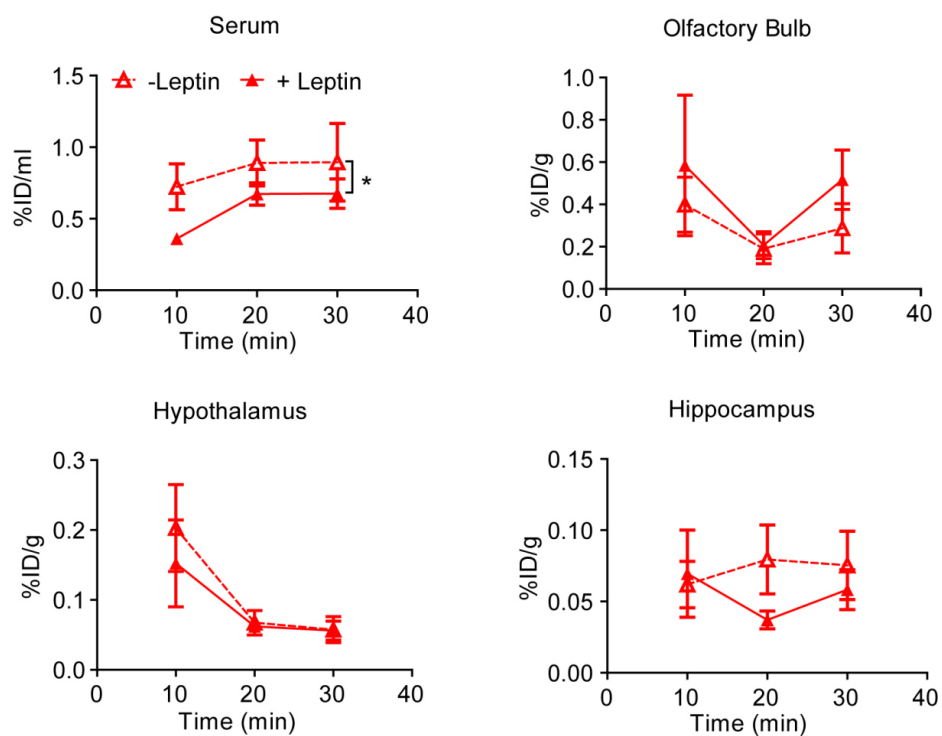
Figure 2.23. Serum absorption and brain regional distribution of intranasally delivered 1:1 conjugates of LepNP85 with or without cold leptin. Each male CD-1 mouse was injected with ^{125}I-labeled LepNP85 with or without 10 μg of cold leptin. Data are mean ± SEM, n = 7/time point, * $p < 0.05$ by Two-way ANOVA.

2.3.9. Blood absorption and brain clearance of leptin conjugate after ICV injection

We also observed that leptin and LepNP85 can be cleared back into blood when administered locally into the brain by ICV injection (**Figure 2.24**). Compared to leptin, plasma concentrations of LepNP85 were higher (p < 0.001 by Two-way ANOVA), suggesting that P85 modification enhanced the brain to blood clearance of leptin (**Figure 2.24a**). Compared to the initial time points, the plasma concentration of leptin dropped significantly at 4 h while the concentration of LepNP85 still remained high and decreased only at 8 h. The more sustained amount of the conjugate found in the blood may be due to both its greater brain to blood clearance as well as its longer circulation half-life compared to the native leptin (**Figure 2.15**). The brain concentrations of leptin were comparable to those of LepNP85 at all time points (**Figure 2.24b**). Compared to the initial time points, the brain concentrations of leptin and LepNP85 only dropped significantly after 4 h.
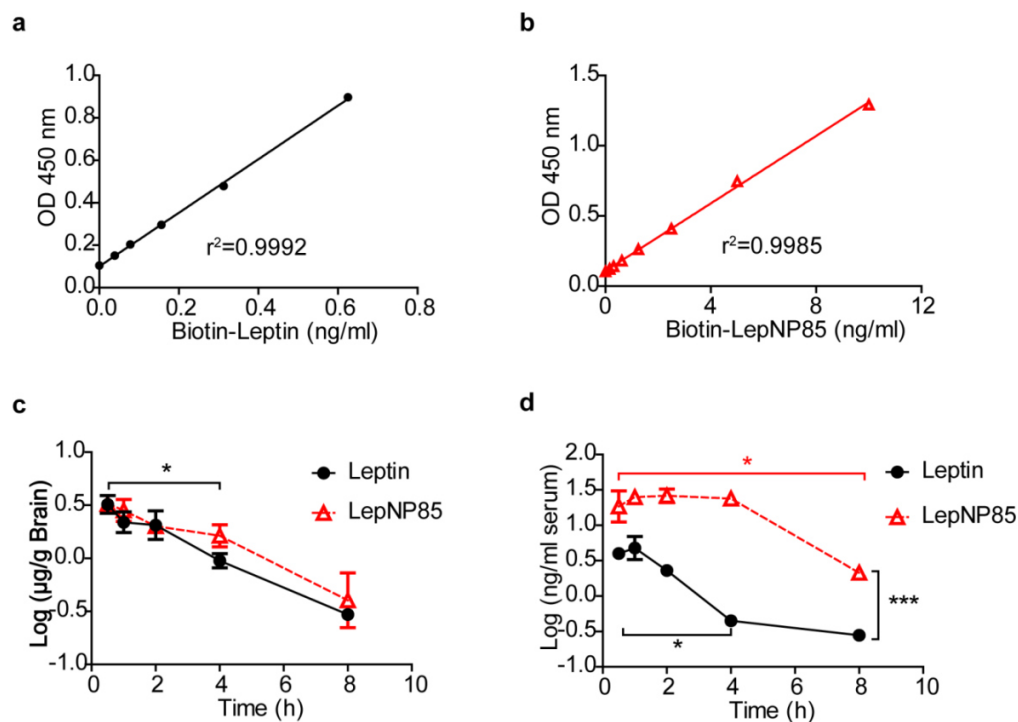
Figure 2.24. Brain clearance and serum absorption of leptin and LepNP85 by ICV injection.
One µg of biotin-labeled leptin and LepNP85 in 1 µl of PBS were injected locally into brain by ICV injection. The concentrations of biotin-labeled proteins in brain lysate and plasma were analyzed by ELISA. **(a, b)** ELISA standard curves for biotin labeled-leptin (a) and biotin-LepNP85 (b). Data are means of two replicates. **(c)** Blood absorption of biotin-leptin and biotin-LepNP85 after ICV injection. **(d)** Brain retention of biotin-leptin and biotin-LepNP85 after ICV injection. Data are mean ± SEM, n = 4/time point, * $p < 0.05$ by One-way ANOVA and post Dunnett's Multiple Comparison Test, and *** $p < 0.001$ by Two-way ANOVA.

2.3.10. Leptin receptor activation in hypothalamus after intranasal administration

One hour following intranasal administration, LepNP85 activated the downstream STAT3 signaling pathway of leptin receptor in brain hypothalamus at a dose of 5 µg/mouse (**Figure 2.25**). At this dose, unmodified leptin was not active. Leptin was found to be inactive until at dose of 12 µg/mouse. At this higher dose, LepNP85 was not active, which is consistent with the U shape response of leptin [259]. Note that the intranasal route is variable especially at low dose. At the dose of 5 µg/mouse, one out of the nine mice in the leptin group and four out of the eleven mice in the LepNP85 group responded to the treatment.
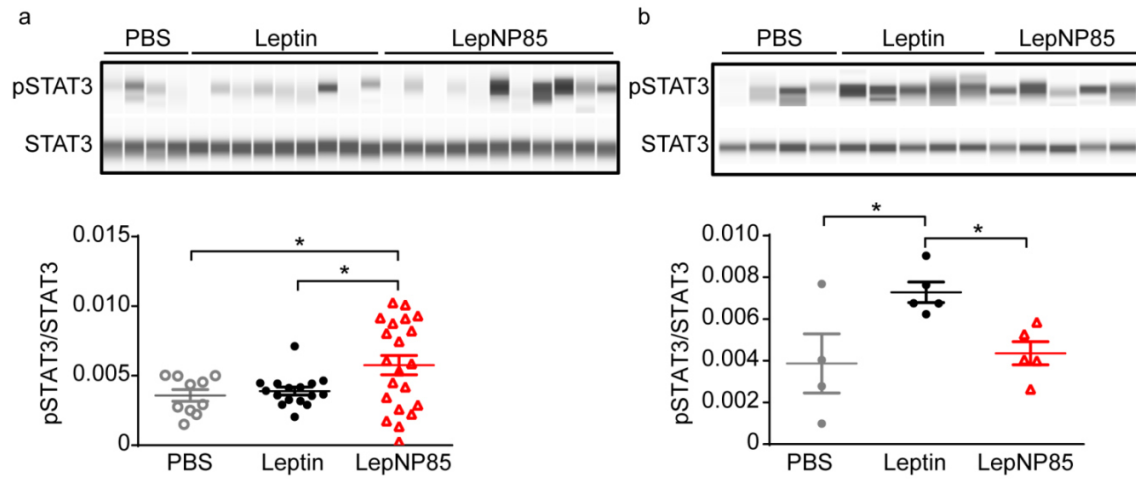
Figure 2.25. Phosphorylation of STAT3 in hypothalamus 1 h after intranasal injection of leptin and LepNP85. (a) At dose of 5 μg/mouse. n = 4-11. The western blotting was repeated twice. **(b)** At dose of 12 μg/mouse. n = 4-5. Data are mean ± SEM, * $p < 0.05$ by One-way ANOVA and post Newman-Keuls Multiple Comparison Test.

2.4. Discussion and conclusion

To improve the delivery of leptin to the brain, we previously modified leptin with P85 via a cleavable disulfide bond linker (LepDSPP85) [43]. In this approach, the polymer was attached to the protein randomly at five lysine amines K6, K12, K16, K34, and K107. The resulting conjugates displayed significantly increased serum stability and circulation time. Their brain accumulation was increased compared to native leptin probably due to the increased exposure to the BBB. Notably, while the 1:1 conjugate relied on the leptin transporter to enter the brain, the 1:2 conjugate was independent of the transporter [43]. However, the random modification also resulted in heterogeneity of the conjugates and considerable loss of their activity, especially in the case of the protein modified with two P85 chains. As previously reported based on the molecular dynamics simulation, the K6 and K12 positional isomers of these conjugates are likely to be inactive since the point modifications of these amino groups should sterically hinder the binding of leptin to its receptor [43]. This conclusion is also reinforced by other modeling studies indicating that K6 and K12 of leptin contribute to the binding specificity by forming salt bridges and hydrogen bonds with D615, E563, N564, and N565 in the leptin-binding domain (LBD) of the leptin receptor [260]. At the same time, based on our modeling study [43], the modification of leptin at the N-terminal amine should not affect the hormone binding to the receptor. Experimentally, leptin has been fused with Fc [261] or Pro/Ala/Ser polypeptides [56] at the N-termini, and the resulting fusion proteins were still active in reducing the body weight in both leptin-deficient ob/ob mice and normal lean mice. Therefore, in the present study, we selectively conjugated P85 to leptin N-terminal amine and showed that this conjugate has improved binding affinity compared to randomly modified forms.

Another limitation of the previously developed random lysine conjugate modified with one P85 polymer chain is that its entry to the brain appeared to be dependent on the BBB transporter, which is impaired in obese patients. We showed here that LepNP85 entered the brain slightly faster than the random conjugate. However, its brain delivery still relied on the BBB transporter as it was inhibited by the unmodified leptin. Hence we explored the INB route to bypass the BBB altogether. Several studies have reported physiological effects of native leptin administered through this route. For example, in a rat seizure model, nasal leptin showed anticonvulsant action via direct effects on glutamate neurotransmission in the hippocampus [262]. More relevantly, food intake was reduced in normal body weight rats and in DIO rats receiving intranasal leptin [185, 203, 263]. These results demonstrate that nasal leptin can access the brain in amounts large enough to produce therapeutic effects. Toxicity was not reported in animals receiving nasal leptin at therapeutic doses [185, 203, 263]. Furthermore, whether used as a weight loss measure or an approach to healthy weight maintenance, an easily and non-invasively administered product should have wide acceptance by the public and the greatest positive impact on our healthcare system [264].

The concept of INB delivery is that compounds administered intranasally gain direct access to the CNS [166]. Three pathways are believed to be involved in ferrying substances across the epithelial barriers and into the CNS: 1) transcellular transport across the sustencular cells in respiratory or olfactory epithelia, and then diffusion via the CSF and brain interstitial fluid; 2) intraneuronal or paraneuronal retrograde transmission via the olfactory nerves across the cribriform plate to olfactory bulb; 3) intraneuronal or paraneuronal retrograde transmission *via* the trigeminal nerve to caudal brainstem. Modification of proteins with amphiphilic Pluronic block copolymers such as P85 has been shown to enhance uptake of these proteins in neurons,

epithelial cells, and endothelial cells [62, 237, 265]. Therefore, we hypothesized that such modification can also enhance the transmembrane penetration of the polypeptide across these epithelial barriers. Towards this goal, we tested if P85 modification improves INB delivery.

We compared LepNP85 to native leptin and random leptin conjugates (LepDSPP85 and LepDSSP85). We also included in this study a comparison of LepNP85 with N-terminal conjugate with PEG having approximately same molecular mass as P85 (LepNPEG5K). We examined the serum absorption and distribution of these compounds in hypothalamus where leptin regulates feeding behavior and in hippocampus where leptin can mitigate the cognitive dysfunction associated with obesity [266, 267] and Alzheimer's disease [268]. Based on this study, LepNP85 was superior in terms of INB delivery to the native leptin as well as each other conjugate except for the non-cleavable random lysine conjugate LepDSSP85. Several conclusions can be made based on this. First, the P85 modification of leptin improved the intranasal delivery of this protein to the relevant regions of the brain. Second, the hydrophobic PPO block of P85 was important in the INB delivery process of the conjugate. (This conclusion was made by comparing the N-terminal conjugates of leptin with PEG (same as PEO) and P85 having a triblock structure PEO-PPO-PEO). Third, the linker between the protein and the copolymer needs to be stable as the cleavable LepDSPP85 conjugate was less successful in terms of INB delivery than the two non-cleavable conjugates LepNP85 and LepDSSP85. These two latter conjugates displayed virtually same brain distribution after intranasal administration, which means that the site of the P85 attachment to the protein is not as important for this delivery pathway. However, the N-terminal conjugate, LepNP85 is still preferable due to its greater binding affinity compared to any of the randomly modified conjugates, LepDSPP85 or LepDSSP85. Although we showed that reduction of disulfide bond partially recovered the

binding affinity of leptin released from LepDSPP85 [43], LepNP85 had comparable binding affinity and central activity to that of native leptin, suggesting that it is unnecessary to release leptin from LepNP85. Taken together, LepNP85 was the best of the studied conjugates for INB delivery of leptin to brain hypothalamus and hippocampus.

This modified form of leptin has displayed the central activity of the hormone after intranasal administration. Specifically, LepNP85 activated the leptin receptor in hypothalamus at 2.4-fold lower dose than the unmodified leptin. This was consistent with the 1.9-fold higher AUC of LepNP85 in hypothalamus compared to the native leptin after INB delivery. Due to the low expression level of leptin receptor in hippocampus, we were not able to detect enhanced phosphorylation of STAT3 in hippocampus following ICV and INB administration of leptin and LepNP85.

Interestingly, P85 modification increased the serum absorption of the LepNP85 conjugate after the intranasal administration compared to the native leptin. The serum distribution of the conjugates appeared to correlate with their hydrophobicity as LepNP85 displayed higher serum levels than LepNPEG5K, but these levels were approximately equal to those of the uncleavable conjugate LepDSSP85. This suggests that the hydrophobic PPO block in P85 facilitates leptin transport across the epithelial barriers into the underneath vasculature. Similar to the native protein, the LepNP85 conjugate at least in part used a saturable pathway for the distribution to the serum that was inhibited by co-administration of the free hormone. It is known that leptin receptors are expressed in human nasal mucosa [269-272] and serum levels of leptin were shown to positively correlate with that of nasal leptin in human [269]. Based on this, we believe that both the membrane binding of the PPO block and the receptor/transporter binding of the leptin might be responsible for the serum penetration of this conjugate after intranasal delivery. We

also observed that leptin and LepNP85 were cleared into blood when administered locally into the brain by ICV injection. Compared to native leptin, blood levels of LepNP85 were higher, suggesting that the P85 modification enhanced the clearance pathway from brain to blood. Very interestingly, the cleavable LepDSPP85 conjugate after intranasal delivery displayed even higher serum levels than LepNP85. This could not be explained by the rapid reduction of the disulfide bond and transformation of LepDSPP85 into the free leptin in the nasal cavity, since the free leptin has even lower rate of serum absorption than LepNP85. Perhaps the disulfide bond reduction during the serum absorption process and the resulting change of protein size and hydrophobicity, recovery of receptor binding affinity, and/or disulfide exchange with endogenous proteins may contribute to the higher serum absorption of LepDSPP85 compared to LepNP85.

We believe that one should not be concerned about the increased serum absorption of leptin as a result of P85 modification, because 1) the overall serum absorption of LepNP85 after intranasal delivery is minimal (< 2% ID/ml at 1 h) and 2) the obese patients with peripheral resistance have compensatory high circulating levels of leptin. However, having in mind that the serum pool of the material can re-enter the brain after BBB penetration, it is important to analyze whether the conjugate has a direct access to the brain from the nose or it enters brain due to reabsorption. Comparing the LepNP85 total brain/serum ratios for IV (~0.02 to 0.04 ml/g) and INB (~0.14 to 0.45 ml/g) suggests that the blood to brain route could explain at the most only ~9 to 14% of the whole brain uptake of this conjugate after intranasal administration. Therefore, we believe that the INB pathway was actually responsible for the increased distribution of the conjugate to the site of desired activity. This conclusion may be less obvious for the native leptin. Indeed, the leptin IV brain/serum ratios (~0.03 to 0.07 ml/g) are relatively closer to the INB

ratios (~0.12 to 0.36 ml/g). Therefore, the blood to brain reabsorption of the native hormone at least in part could contribute to its delivery to the brain after intranasal administration in the healthy animals. However, there are previous indications that native leptin can undergo the direct transport from nose to brain as INB delivery of leptin successfully reduced appetite and body weight in DIO models (where impaired transporter would have prevented the blood-to-brain reabsorption) [185, 203, 263]. Besides, Fliedner, et al demonstrated that IV injection of unlabeled leptin cannot inhibit brain accumulation of radiolabeled leptin administered by INB route, suggesting that leptin takes a direct pathway from the nose to the brain [247]. We have also demonstrated that in a DIO mice model INB LepNP85 accumulated in the brain hypothalamus and hippocampus better than the unmodified leptin. Brain distribution of intranasal LepNP85 in healthy mice and DIO mice was essentially same. Taken together, the increased brain accumulation of LepNP85 is not due to enhanced blood absorption and subsequent brain reabsorption, but due to enhanced direct nose-to-brain delivery of the hormone as a result of its modification with P85.

We did not observe aggregation of LepNP85 after the modification of leptin with the block copolymer. Moreover, at the active dose of LepNP85 (5 µg/mouse), the concentration of the injected solution was 0.625 mg/ml (5 µg in 8 µl PBS) or 29.8 µM, which is lower than the critical micelle concentration (CMC) of P85 (0.03 wt% [273] or 65.2 µM). The pharmacokinetic studies used trace amounts of radiolabeled leptin. This suggests that LepNP85 was unlikely to form micelles under the conditions used in the animal studies. Taken together, we believe that the improvement in the absorption of leptin as a result of P85 modification is likely due to the increased hydrophobicity and transmembrane penetration of the conjugate across the nasal epithelial barrier [62, 237, 265].

To the best of our knowledge, this is the first study showing that P85 modification of leptin can enhance its direct nose-to-brain transport of the hormone and its activity with respect to the receptor. In general, formulation strategies used to enhance direct nose-to-brain delivery of therapeutic proteins remain largely unexplored [163, 274]. Absorption enhancers/tight-junction modulators, bioadhesive polymers, enzyme inhibitors, and nanoparticles have been studied [187-191], aiming to improve the stability, prolong the residence time, create a local drug depot or enhance absorption across the mucosa epithelium. However, many of these strategies enhance systemic absorption following intranasal administration [192, 201]. Specifically for leptin, using an absorption enhancer lysophosphatidylcholine only enhanced systemic absorption but not the brain delivery [203]. In addition, the INB delivery of LepNP85 is independent of its receptors/transporters expressed in the nasal route, likely suggesting that our approach may be generalized for other proteins.

Of the challenges remaining for the development of an efficient treatment for obesity, we would like to point out significant variability in the delivery and activity of the INB administered hormone. Limited information is available on the influence of dosing volume, tube insertion depth, head position, and anesthesia on the nasal distribution pattern and efficiency of INB delivery [210-213]. Targeting the olfactory epithelium is likely to be more challenging in human than the experiments on rodents which have over 50% nasal cavity surface covered by olfactory epithelium [6]. The drug should pass through the narrow triangular shaped nasal valve to reach the posterior olfactory epithelium [6]. To decrease variability and improve INB delivery, one may need to use nasal devices such as one of those reported by Djupesland et al. [6]. Moreover, since obesity is a chronic disease and P85 modification did not enhance the retention of leptin in

the brain, the use of a depot system for LepNP85 may further be beneficial for the treatment of obesity.

In summary, we improved the brain delivery of leptin for treatment of obesity by conjugating this protein with Pluronic P85 and utilizing the INB route to bypass BBB. The conjugation was carried out by selectively modifying the N-terminal amine of leptin to preserve the protein binding affinity and maximize homogeneity of the conjugate. We showed that this modification enhanced the direct nose-to-brain transport of leptin.

CHAPTER III: MACROPHAGE EXOSOMES AS NATURAL NANOCARRIERS FOR PROTEIN DELIVERY TO INFLAMED BRAIN[3]

3.1. Introduction

Exosomes are 40 to 200 nm membrane-encased vesicles secreted by cells *via* fusion of multivesicular bodies with cell plasma membranes. They contribute to intercellular communication by carrying proteins and RNAs between neighboring cells or even to distant organs, and were clinically evaluated as cancer vaccines. Tumor-derived exosomes loaded with curcumin were previously shown to accumulate in microglial cells and alleviate brain inflammation [137]. Moreover, Mφ-derived exosomes loaded with catalase produce neuroprotection in a PD mouse model [275]. Both studies employed an intranasal route of administration, which in theory allows substances to bypass the BBB and directly enter the brain with minimum blood exposure. However, it is unclear if these exosomes access the brain directly or indirectly *via* absorption into blood and subsequent blood to brain transport. Nonetheless, the percentage of injected dose reaching the brain following intranasal delivery is usually lower than 1% and can be as low as 0.1% or even less [6]. Furthermore, this administration route has high variability in the dose reaching the brain due to variability in drug disposition and is limited by the drug amounts that can be delivered in humans [276]. A systemic, for example, IV administration route enables direct access to the BBB and uniform distribution through the brain

---

capillaries. However, brain bioavailability of ~98% of small-molecule drugs and almost all biomacromolecules is very poor. To address BBB penetration, exosomes from dendritic cells (DCs) were decorated with the brain targeting peptide (RVG) [136]. These modified exosomes delivered siRNA and silenced a gene of relevance to AD in the brain [136]. Unfortunately, such peptide-decorated exosomes can cause immune response. The immunogenicity of the targeting peptide alone is likely low. However, exosomes present major histocompatibility complex molecules and a co-stimulatory molecule CD86 on the surface, which can potentially boost the immune response, especially with chronic exposure [277, 278]. Naïve exosomes released from brain endothelial cells were shown to penetrate the BBB, delivering a fluorescent marker and a chemotherapeutic agent, doxorubicin, to the brain in Zebrafish [139]. Therefore, it is crucial to investigate whether naïve exosomes could penetrate the BBB in preclinical animal models, such as rodents and primates.

We examined the possibility of utilizing naïve exosomes as drug carriers for CNS. Our rationale was based on prior experience using Mϕs as cell carriers to treat CNS associated disorders [102, 106, 108]. Pathology of many neurologic disorders, including multiple sclerosis, AD, PD, stroke, brain tumors, traumatic brain injuries, and others can result in BBB dysfunction [279]. The inflammatory processes associated with some of these pathologies can increase diapedesis of peripheral immune cells across the BBB [280]. Gendelman's group used Mϕs as carriers for nanoformulated antiretroviral therapy for human immunodeficiency virus type 1 (HIV-1)-associated neurocognitive disorders [103]. We used Mϕs as carriers for systemic delivery of the nanoformulated therapeutic proteins and genes to the inflamed brain in the PD models [102, 106, 108]. The functional activity of Mϕs in these applications can be in part mediated by exosomes that share common elements, such as lymphocyte function-associated

antigen 1 (LFA-1) involved in the diapedesis of Mϕs across endothelial barriers [96]. The Mϕ exosomes can mediate the transfer of their cargo to other brain resident cells [102, 105, 108, 109], or facilitate spreading of viruses and virus proteins from periphery to and within the brain [124, 281].

3.2. Materials and methods

3.2.1. Material

FBS, penicillin-streptomycin, Dulbecco's modified eagle medium (DMEM), 0.25 % trypsin/EDTA, chemically defined lipid concentrate, HEPES (1M), CM-DiI, protein G magnetic beads, Illustra Nap-5 columns, G418 sulfate, Alexa Fluor 488-Transferrin(Tf), Alexa Fluor 488-Cholera toxin subunit B (CTB), and SlowFade® Gold antifade mountant were from Life Technologies (Grand Island, NY). Rat collagen I (lower viscosity) and Anti-Human DEC-205 antibodies were from R&D systems (Minneapolis, MN). Endothelial cell growth EBM-2medium was from Lonza (Basel, Switzerland). Goat anti-apoptosis-linked-gene-2 interacting protein X (Alix), goat anti- tumor susceptibility gene 101 protein (Tsg 101), goat anti-LFA-1 and rabbit anti-intercellular adhesion molecule 1 (ICAM-1) antibodies were from Santa Cruz (Dallas, Texas). Rat anti-lysosome-associated membrane protein 2 (LAMP-2), rabbit anti-clathrin heavy chain antibodies was from Abcam (Cambridge, MA). Rabbit anti-caveolin-1 antibodies were from Cell Signaling (Danver, MA). $Na^{125}I$ and $Na^{131}I$ were from Perkin-Elmer Life Sciences (Boston, MA). Formvar coated copper grid (200 meshes), M-per mammalian protein extraction reagent, Micro BCA protein assay kit, agarose, HALT™ proteinase and phosphatase inhibitor cocktail and ECL western blotting substrate were purchased from Thermo Fisher Scientific (Rockford, IL). BDNF was purchased from PeproTech (Rocky Hill, NJ). 4-15% polyacrylamide gel, native sample buffer, and laemmli sample buffer are purchased from Bio-Rad (Hercules,

CA). Human basic fibroblast growth factor (bFGF), hydrocortisone, FITC-dextran conjugates (70 kDa), LPS, and all other chemicals were from Sigma-Aldrich (St-Louis, MO).

3.2.2. Cell Culture

Raw 264.7 Mϕs (RAW Mϕs, American Type Culture Collection ATCC® TIB-71TM, Rockville, MD) between passage 1 and 30 were used. The cells were grown in DMEM medium plus 10% FBS and 1% penicillin-streptomycin, and subcultured by scraping. The conditioned medium for exosome collection was DMEM plus 1% penicillin-streptomycin and 10% FBS pre-centrifuged at 120,000g for 140 min to remove serum exosomes. hCMEC/D3 cells (a kind gift from Dr. Pierre-Olivier Couraud in Cochin Institute, France) between passage 30 and 35 were used. All cell cultureware for hCMEC/D3 cells was coated with 0.15 mg/ml rat collagen I. The cells were grown in EBM-2 containing 5% FBS, 1% Penicillin-Streptomycin, 1.4 µM hydrocortisone, 5µg/ml acid ascorbic, 100× diluted chemically defined lipid concentrate, 10 mM HEPES and 1 ng/ml bFGF . NIH-3T3 cells stably transfected with TrkB receptors (a kind gift from Dr. David Kaplan in University of Toronto, Canada) was cultured in DMEM supplemented with 10% Colorado Calf serum and 100 µg/ml of G418 sulfate.

3.2.3. Purification of Exosomes

Exosomes were purified by the common sequential centrifugation method [136, 282]. Raw Mϕs were grown in 7 T75 flasks to reach 70-80% confluence. Following two PBS washes, the cells were cultured in 10 ml conditioned medium for 2 days. The medium was then collected and centrifuged sequentially at 300g for 15 min, 3,000 g for 15 min, 20,000g for 70 min, and filtered through 0.2 µm membrane filters to remove cells and large particles. Exosomes were pelleted at 120,000g for 70 min, washed by PBS to remove proteins, pelleted again, and then resuspended in 1 ml PBS. For cell uptake study, the exosomes were labeled with CM-DiI dyes (2 µg/ml) added

to the medium before the first 120,000g pelleting step. The exosome suspension was filtered through 0.22 μm membrane filters to sterilize and remove the dye precipitate and stored in -80 °C for at most 3 weeks. Each batch of exosomes contained around 65 μg exosomal proteins as determined by microBCA and 3×10^{11} exosomes as determined by nanoparticle tracking analysis (NTA).

3.2.4. Characterization of Exosomes

Exosomes were characterized by DLS for intensity-weighted z-average diameter, PDI and zeta potential, by NTA for number-weighted diameter and particle concentration, and by transmission electron microscopy (TEM) for morphology. For DLS, the size was measured in PBS, and the zeta-potential was measured in 10 mM NaCl at 23 °C with a 173° scattering angle using Zetasizer Nano-ZS instrument (Malvern, UK) in at least triplicates. For NTA, each sample was diluted 500 times in PBS and loaded into Nanosight NS500 (Malvern, UK). Three videos of 60s with a sample advance in between were recorded with the minimal expected particle size, minimum track length and blur setting all set to automatic. For TEM, exosomes were adsorbed onto Formvar coated copper grid (200 mesh), stained with 2% uranyl acetate and characterized using Zeiss TEM 910 Transmission Electron Microscope (Jena, Germany) at 80 kV accelerating voltage.

3.2.5. Protein Composition and Exosomal Markers

Mϕs and Mϕ exosomes were lysed with RIPA buffer mixed with proteinase and phosphatase inhibitor cocktail. Protein composition and exosomal markers were detected by standard SDS-PAGE and western blot under reducing condition [282].

3.2.6. Cell Viability

Cell viability was determined by 3-(4, 5-dimethylthiazol-2-yl)-2, 5-diphenyltetrazolium bromide (MTT) assay. hCMEC/D3 cells were seeded in 96-well plates at 2000 cells/well in culture medium. After overnight incubation, the cells were treated with test agents in culture medium for time durations indicated in figure legend, and let grown in fresh culture medium (200 µl) for another 72 h. 20 µl of MTT in PBS (5 mg/ml) was added to each well. After 4 h incubation at 37 °C, the formed formazan precipitate was dissolved in 150 µl of DMSO. Absorbance at 570 nm (A) was read on a microplate reader SpectraMax M5 (Molecular devices). Blanks (wells without cells) that account for solvent adsorption and controls (wells with cells without test agents) for 100% viability were treated similarly. Cell viability (%) was calculated as $((A_{treated} - A_{blank}))/((A_{control} - A_{blank})) \times 100\%$. Data are means ± SD of 6 replicate wells.

3.2.7. Flow Cytometry

hCMEC/D3 cells were grown in 24-well plate at 5×10^4 cells/well for 4-5 days to reach confluence. In the uptake mechanism studies, the cells were pretreated with endocytosis inhibitors, carbohydrates or EGTA for 0.5 h, and then co-treated with CM-DiI labeled exosomes $(0.6 \times 10^{10}$ exosomes/ml) for 4 h. The inhibition of endocytosis markers uptake was studied similarly. The endocytosis markers used were Alexa Fluor 488-Transferrin (10 µg/ml) for clathrin mediated endocytosis, Alexa Fluor 488-CTB (5 µg/ml) for caveolae mediated endocytosis, and FITC-Dextran (70 kDa (10 mg/ml) for macropinocytosis. The antibody block assays were done by co-incubating exosomes with antibodies or isotope controls at 100 µg/ml for 4 h. The cells were washed thrice by PBS, detached by 0.25% trypsin/EDTA, collected by centrifugation at 100 g for 10 min, fixed with 4% paraformaldehyde for 10 min, and then

resuspended in 0.35 ml PBS. Viable singlets were gated based on forward scatter and side scatter. 5,000-10,000 viable singlets were recorded for each sample on Becton Dickinson LSRII (BD Biosciences) using 488 nm and 532 nm lasers. Unless otherwise noted in figure legend, data are not normalized and reported as mean fluorescence intensity (MFI) ± SD of 3 replicate wells.

3.2.8. Laser scanning confocal microscopy (LSCM)

hCMEC/D3 cells were cultured in 35 mm glass bottom dishes at 1×10^5 cells/well for 5-6 days to reach confluence. In endocytosis pathway studies, the cells were treated with CM-DiI labeled exosomes (1×10^{11} exosomes/ml) and Alexa Fluor 488-Transferrin (25 µg/ml) or Alexa Fluor 488-CTB (5 µg/ml) for 0.5 h, and then fixed before imaging. In the immunofluorescence studies, the cells were treated with CM-DiI labeled exosomes (1×10^{11} exosomes/ml) for 0.5 h, fixed by 4% paraformaldehyde, blocked with 10% goat serum/0.3% Triton® X-100 in PBS at room temperature for 1 h, and incubated with anti-clathrin heavy chain or anti-caveolin 1 antibodies in 1% goat serum/1% BSA/0.3% Triton® X-100 in PBS at 4 °C overnight. Followed three washes using 0.1% BSA in PBS, the cells were incubated with Alexa Fluor 488 conjugated secondary antibodies, washed trice and mounted in SlowFade® Gold antifade mountant (Life technologies). Images were collected by Zeiss CLSM 700/710 spectral confocal laser scanning microscope (Jena). Mander's colocalization coefficients were calculated using Image J and JACoP plugin [283, 284].

3.2.9. Native gel electrophoresis

Protein samples were mixed with equal volume of native sample buffer (Bio-Rad), and then resolved on 4-15% polyacrylamide gel (Bio-Rad) in 25 mM Tris-Cl/250 mM glycine, pH 8.5 at 120 v for 55 min, or on 0.5% horizontal agarose gel in 40 mM Tris/20 mM acetic acid/1 mM

EDTA, pH 7.6 at 80 v for 50 min. The gels were stained with coomassie blue G250, and scanned using FluorChem E System (ProteinSimple).

3.2.10. Radioactive Labeling

Exosomes and proteins were labeled with iodine by chloramine-T method [43]. For this study, we collected Mϕ exosomes after 12 h incubation of Mϕ in DMEM to exclude iodination of serum proteins that could be co-precipitated during isolation of exosomes by ultracentrifugation. Briefly, exosomes or proteins were mixed with 1 mCi of Na^{125}I or Na^{131}I (Perkin Elmer) and 10 µg of chloramine-T in phosphate buffer (0.25 M, pH 7.5) for 60 s. Labeled exosomes and proteins were purified by Illustra Nap-5 columns (Life technologies) and collected in tubes pretreated with 1% BSA in PBS to prevent nonspecific adsorption. The iodine association (iodine in labeled sample/total iodine) was determined by trichloroacetic acid precipitation method [43]. Briefly, 1 µl of purified samples was mixed with 0.5 ml of 1% BSA in PBS and 0.5 ml of 30% TCA, and then centrifuged at 5400g for 10 min. The resulted pellet and supernatant were counted on r-counter (PerkinElmer). The iodine association was calculated as the percentage of pellet radioactivity to total radioactivity. The iodine association for exosomes and BSA/BDNF was higher than 85% and 98%, respectively.

3.2.11. Animal studies

All animal experiments were conducted under the approval of the University of North Carolina Institutional Animal Care and Use Committee. Six to eight weeks old male CD-1 mice were purchased from Charles River Laboratories.

3.2.11.1. Animal procedures

Mice were anesthetized with 40% urethane (4 g/kg) by IP injection. ^{125}I-labeled substances (4×10^5 cpm) and ^{131}I-labeled BSA were co-injected to the right jugular vein. At each time point,

blood was collected from the left carotid artery, allowed to clot and then centrifuged at 5400g for 10 min to collect serum. The mouse was immediately decapitated after collection of the arterial blood and the whole brain and peripheral organs removed and weighed immediately after decapitation. The radioactivity of serum and tissues were counted and normalized to injected dose (ID) by volume (ml) or weight (g) (%ID/ml or %ID/g). An injection check representing ID was also counted (n = 3).

3.2.11.2. Noncompartmental analysis of PK parameters

The noncompartmental PK parameters including the volume of distribution at steady state Vss (ml), the rate of clearance, CL (ml/min), the mean residence time from the time of dosing to last detectable concentration MRT_{last} (h), and MRT_{inf} (h) were estimated using Phoenix$^{®}$WinNonlin$^{®}$ 6.3 (Pharsight).

3.2.11.3. Multiple-time regression analysis of influx into the brain

The Ki (slope) and Vi (y-intercept) were calculated from the linear portion of multiple-time regression analysis [246]. Brain/serum ratios (Am/Cp_t, ml/g) of co-injected BSA were used to correct for the vascular space or leakage [285], and subtracted from that of the test substance to yield the delta brain/serum ratios. The delta brain/serum ratios were plotted against their respective exposure times using the equation

$$Am/Cp_t = Ki \left. \int_0^t Cp_t dt \middle/ Cp_t \right. + Vi$$

, where the exposure time ($\left. \int_0^t Cp_t dt \middle/ Cp_t \right.$) was the trapezoidal integral of serum cpm at time t (Cp_t) from time 0 to time t divided by Cp_t.

3.2.11.4. Brain accumulation

Brain accumulation of test substance (%ID/g) was calculated by multiplying the delta brain/serum ratio (ml/g) with serum concentration (%ID/ml) at selected time point.

3.2.11.5. Capillary depletion

Capillary depletion was performed to determine whether the injected substances cross the capillary walls and enter the brain parenchyma as previously reported [285]. 10 min after injection, serum and brain samples were collected as mentioned above. The brain was homogenized in 1.25 ml of physiological buffer containing 10 mM HEPES, 141 mM NaCl, 4 mM KCl, 2.8 mM $CaCl_2$, 1 mM $MgSO_4$, 1 mM NaH_2PO_4, and 10 mM D-glucose, pH 7.4, and then mixed with equal volume of 40 % Dextran (70 kDa, Sigma) by vortex. The mixture was centrifuged at 3500g for 20 min at 4 °C. The radioactivity of the capillary pellet, parenchyma supernatant, and serum was counted. The delta capillary/serum ratio and parenchyma/serum ratio of ^{125}I-labeled test substance was corrected using ^{131}I-BSA data, and then multiplied by the serum concentration to calculate the uptake (%ID/g) in brain capillary and parenchyma.

3.3. Results

3.3.1. Characterization of Mϕ exosomes

We hypothesized that Mϕ-derived exosomes can naturally bind with brain endothelial cells, pass across the BBB, and enter the brain. To test this hypothesis, we collected exosomes secreted by RAW Mϕs by the sequential centrifugation method [136, 282]. We characterized their size distribution and zeta potential by DLS and NTA, morphology by TEM, and protein composition by SDS-PAGE and western blotting (**Figure 3.1**). Consistent with published results [136, 286], Mϕ exosomes were heterogeneous by size with an intensity-weighted z-average diameter of 149 ± 10 nm, a relatively small PDI of 0.134 ± 0.048 as determined by DLS, a number-weighted

mean diameter of 130 ± 49 nm and a mode diameter of 90 ± 2 nm by NTA. Mϕ exosomes were

negatively charged (zeta potential -18 mV) in 10 mM NaCl. TEM showed spherical morphology

as published [282]. Occasionally, we observed aggregation and cup-shaped nanovesicles as an

artifact of sample drying [282]. Based on SDS-PAGE, the protein composition of exosomes

differed from both the parent Mϕs and fetal bovine serum (FBS) [282]. As revealed using

western blotting, compared to Mϕs, exosomes were enriched with Alix and Tsg 101, two

exosomal markers related to the biogenesis of multivesicular bodies [124]. Mϕ exosomes also

contained a transmembrane protein LAMP 2 and a cytosolic protein β-actin that are frequently

detected in exosomes [124].
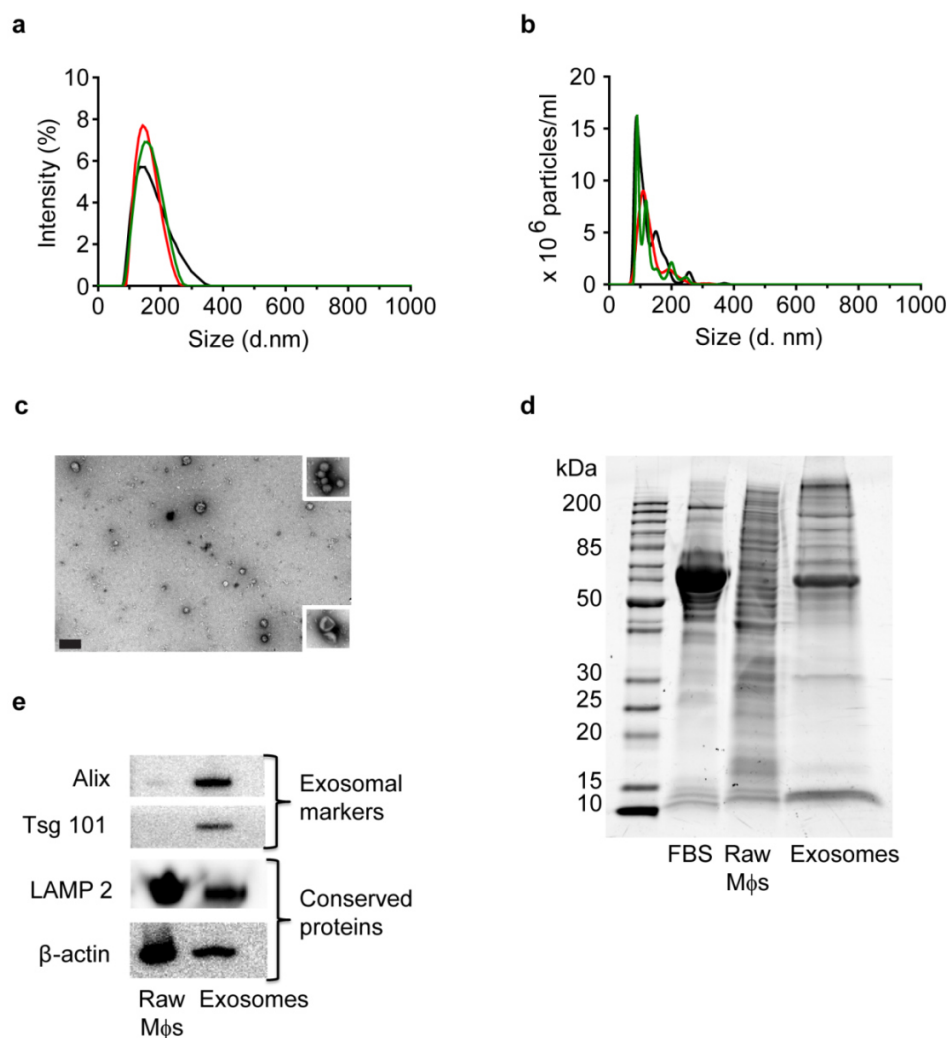
Figure 3.1. Characterization of Mϕ exosomes. (a) Intensity-weighted size distribution of exosomes by DLS. **(b)** Number-weighted size distribution of exosomes by NTA. Different colors show three repeated measurements. **(c)** Morphology of Mϕ exosomes by TEM. Scale bar = 200 nm, magnification × 50,000. Insets show the aggregation and artificial cup-shape. **(d)** SDS-PAGE of lysates of RAW Mϕs and exosomes for protein composition. **(e)** Western blotting of RAW Mϕs and exosome lysates at comparable protein loading amounts showing exosomal markers and conserved proteins.

3.3.2. Cell uptake of Mϕ exosomes in brain endothelial cells

Next, we characterized the interactions of Mϕ exosomes with human cerebral microvascular endothelial cells (hCMEC/D3) as an *in vitro* BBB model. The MTT assay showed that the viability of these cells was not affected by their exposure to Mϕ exosomes for 24 h up to the highest tested concentration of 2×10^{11} exosomes/ml (**Figure 3.2a**). All subsequent studies involving hCMEC/D3 cells used lower concentrations of exosomes. We labeled exosomes with the lipophilic dye CM-DiI to monitor their uptake by hCMEC/D3 cells. CM-DiI labeling did not significantly change the size distribution and zeta-potential of exosomes as determined by DLS (the intensity-based diameter of CM-DiI labeled exosomes was 166 ± 18 nm, PDI 0.139 ± 0.03, and zeta potential -18 ± 5 mV). A*fter an initial lag* period of 4 h, the amount of Mϕ exosomes in hCMEC/D3 cells increased in a linear fashion over 48 h (**Figure 3.2b**).
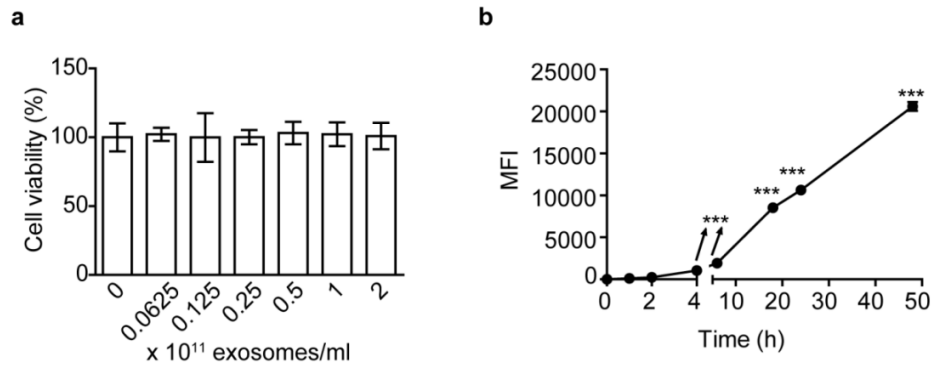
Figure 3.2. Cytotoxicity and time-dependent uptake of Mϕ exosomes in hCMEC/D3 cells.
(a) Cell viability of hCMEC/D3 cells after 24 h incubation with exosomes and another 72 h in fresh culture medium was determined by MTT assay. Data are means ± SD, n = 6. Cell viability of exosomes-treated cells was comparable to untreated cells. **(b)** Time-dependent uptake of CM-DiI labeled exosomes at 0.6×10^{10} exosomes/ml. *** $p < 0.001$ *vs.* untreated cells. Cell uptake was determined by Flow cytometry. Data are MFI ± SD of 5000-10000 live singlets, n = 3. Statistical comparisons are made by one-way ANOVA and post Newman-Keuls multiple comparison test.

Incubation at 4 °C completely blocked the uptake of Mϕ exosomes (**Figure 3.3a**), suggesting that their internalization in hCMEC/D3 cells is an energy-dependent process. To dissect the endocytosis pathways, we pre-incubated hCMEC/D3 cells with endocytosis inhibitors for 0.5 h, and then co-incubated with fresh inhibitors and Mϕ exosomes for another 4 h. We selected hyperosmolar sucrose [287], nystatin [287], and 5-(N-Ethyl-N-isopropyl) amiloride (EIPA) [288] as the inhibitors for clathrin-mediated endocytosis, caveolae-mediated endocytosis, and macropinocytosis, respectively. Each inhibitor, at non-toxic concentrations (**Figure 3.4**), diminished uptake of a corresponding endocytosis marker (transferrin, CTB, and dextran) (**Figure 3.3b**, **c**, **d**). Each of these inhibitors also decreased the uptake of Mϕ exosomes (**Figure 3.3a**). Note that the chemical inhibitors are rarely exclusive for each endocytosis pathway [289, 290], and hence the percentage of inhibition of cellular uptake by each of the inhibitor cannot represent the absolute contribution of each endocytosis pathway. However, this study suggested that these exosomes, similar to exosomes derived from tumor or immune cells [291], utilize multiple pathways (including clathrin, caveolae, and macropinocytosis) to enter the endothelial cells. Involvement of clathrin and caveolae pathways was further supported by colocalization of Mϕ exosomes with transferrin, anti-clathrin heavy chain antibodies, CTB, and anti-caveolin 1 antibodies (**Figure 5**).
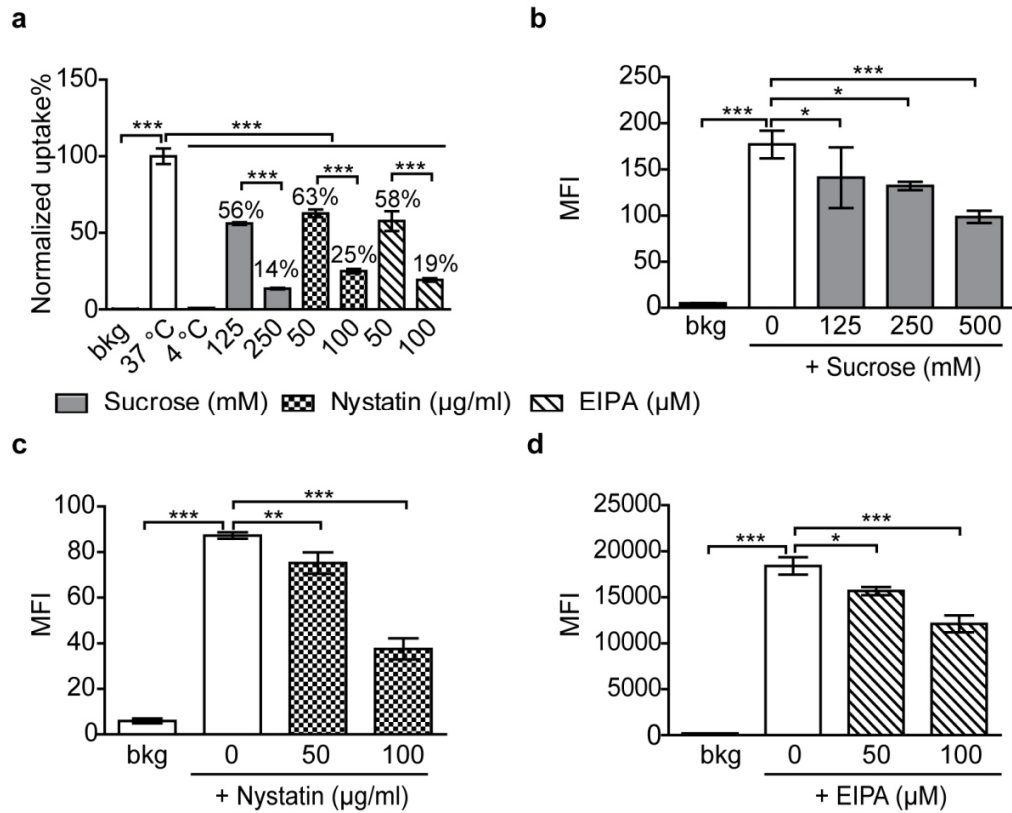
Figure 3.3. Endocytosis pathways of Mφ exosomes in hCMEC/D3 cells. Cells were pre-incubated with endocytosis inhibitors for 0.5 h, and then incubated with fresh inhibitors and **(a)** CM-DiI labeled exosomes at 0.6×10^{10} exosomes/ml, **(b)** Alexa Fluor 488-transferin at 10 μg/ml, **(c)** Alexa Fluor 488-CTB at 5 μg/ml, or **(d)** FITC-dextran (70 kDa) at 10 mg/ml for another 4 h. All inhibitors at selected concentrations (except sucrose at 500 mM) ensured at least 80% cell viability. Cell uptake was determined by flow cytometry and in (a) normalized to 37 °C group. Data are MFI ± SD of 5000-10000 live singlets, n = 3, * $p < 0.05$, ** $p < 0.01$, and *** $p < 0.001$ *vs.* untreated cells background (bkg) or indicated groups by one-way ANOVA and post Newman-Keuls multiple comparison test.
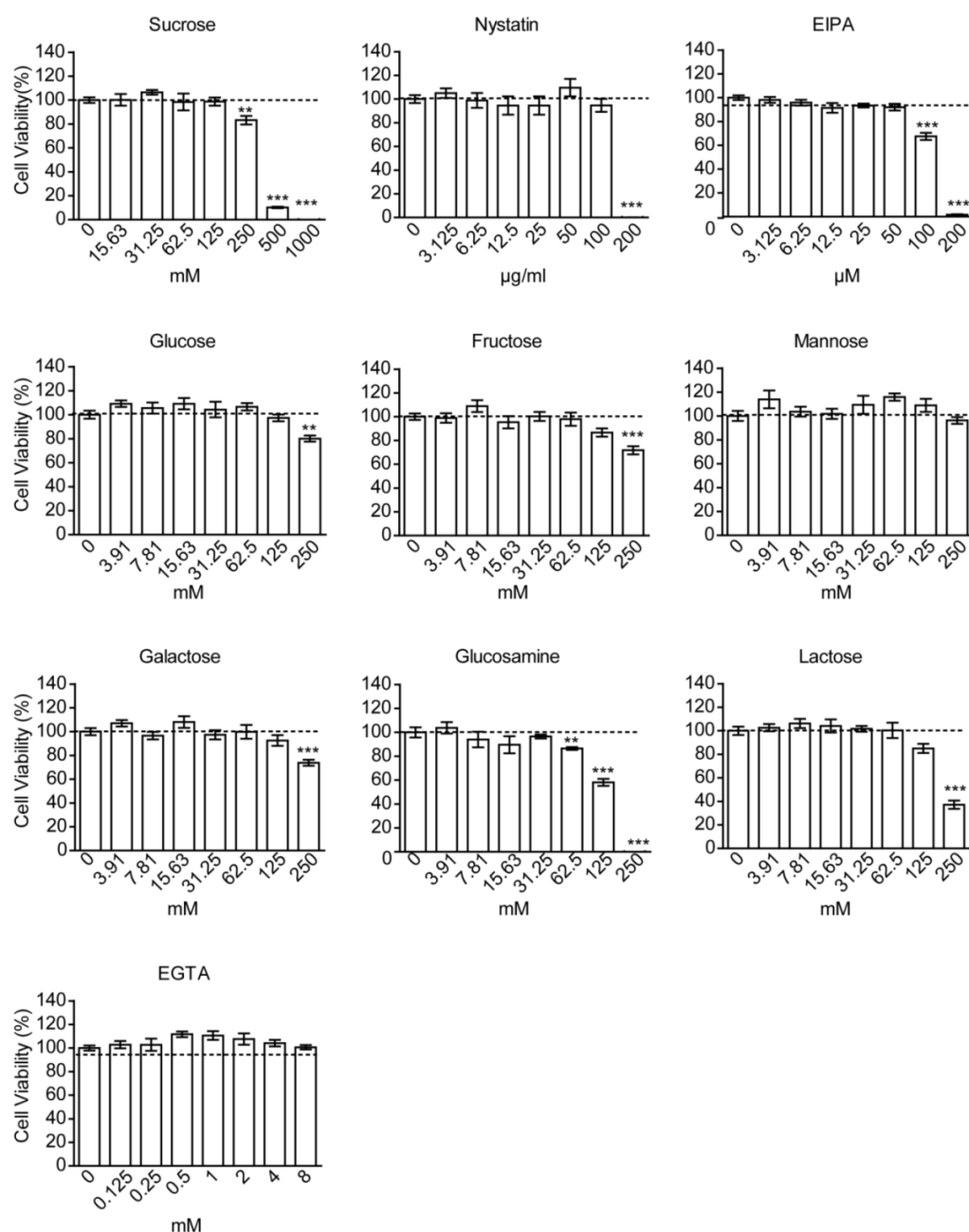
Figure 3.4. Effects of endocytosis inhibitors, carbohydrates and EGTA on cell viability of hCMEC/D3 cells. Cells were treated with indicated compounds for 5 h, and then let grow in fresh medium for another 72 h. Cell viability was determined by MTT assay. Data are means ± SD, n = 6, ** $p < 0.05$ and *** $p < 0.001$ for treated cells *vs.* untreated cells by One-way ANOVA and post Newman-Keuls multiple comparison test.
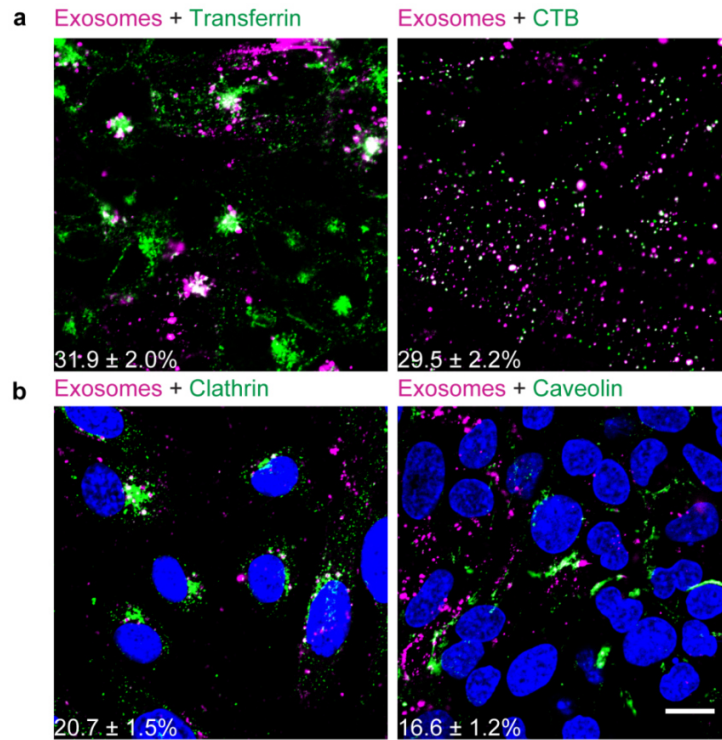
Figure 3.5. LSCM of the uptake of Mϕ exosomes in hCMEC/D3 cells. (a) hCMEC/D3 cells were treated with CM-DiI labeled exosomes (purple) at 1×10^{11} exosomes/ml and Alexa Fluor 488-transferrin (green) at 25 µg/ml or Alexa Fluor 488-CTB (green) at 5 µg/ml for 0.5 h, and then fixed before imaging. (b) hCMEC/D3 cells were treated with CM-DiI labeled exosomes (purple) at 1×10^{11} exosomes/ml for 0.5 h, fixed, and then immunostained with anti-clathrin heavy chain or anti-caveolin-1 antibody (green). Mean ± SD of Mander's colocalization coefficients calculated by Image J JACoP plugin [283, 284] from 7-30 different fields of view are shown in percentage. Colocalized regions were shown in white. Scale bar 15 µm.

The concentration dependence of the uptake (at 4 h time point) suggested saturation at high concentrations of Mϕ exosomes (**Figure 3.6a**), similar to the reported uptake of glioblastoma exosomes in glioblastoma cells [292]. Non-labeled exosomes decreased uptake of fluorescently labeled exosomes in a concentration-dependent manner (**Figure 3.6b**). This suggested a possibility of saturable receptor interactions and we therefore examined the molecular mechanisms involved.
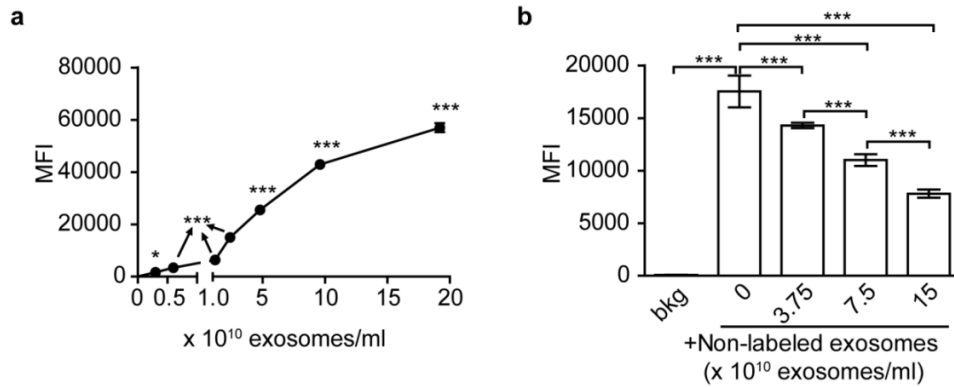
Figure 3.6. Saturable uptake of Mϕ exosomes in hCMEC/D3 cells. (a) Concentration-dependent uptake of CM-DiI labeled exosomes at 4 h. * $p < 0.05$ and *** $p < 0.001$ *vs.* untreated cells. **(b)** Inhibition of uptake of CM-DiI labeled exosomes (0.6×10^{10} exosomes/ml at 4 h) by non-labeled exosomes. *** $p < 0.001$ *vs.* bkg or indicated groups. Cell uptake was determined by Flow cytometry. Data are MFI ± SD of 5000-10000 live singlets, n = 3. Statistical comparisons are made by one-way ANOVA and post Newman-Keuls multiple comparison test.

3.3.3. ICAM-1/LFA-1 mediated cell uptake of Mϕ exosomes in brain endothelial cells

The interactions between integrin LFA-1 and ICAM-1 were previously implicated in the uptake of Mϕ exosomes in human umbilical vein endothelial cells [122]. The LFA-1 and ICAM-1 were indeed expressed in our Mϕ exosomes and hCMEC/D3 cells, respectively (**Figure 3.7a, b**). The ICAM-1 was upregulated by treating hCMEC/D3 cells with LPS (**Figure 3.7b**), which mimics the response of brain endothelial cells to inflammation [293], and was accompanied by the increased accumulation of exosomes in the cells (**Figure 3.7c**). Moreover, each of anti-ICAM-1 or anti-LFA-1 antibodies and their combination inhibited the exosome uptake (**Figure 3.7d**) suggesting that both LFA-1 and ICAM-1 play an important role in the uptake of Mϕ exosomes in brain endothelial cells.

3.3.4. C-type lectin receptors mediated uptake of Mϕ exosomes in brain endothelial cells

During the endocytosis inhibition studies (**Figure 3.3**), we noted that sucrose had a more profound inhibitory effect on the cell uptake of Mϕ exosomes than that of transferrin. Therefore, we hypothesized that some additional carbohydrate binding receptors may be involved in the uptake of exosomes. The possible candidates are the C-type lectin receptors that require binding of calcium for their carbohydrate-binding activity [294]. It was reported that DCs-derived exosomes are internalized into recipient cells partially by mannose/glucosamine-binding C-type lectin receptors, as was demonstrated by a blocking assay using DEC205 antibodies, the calcium chelator ethylenediaminetetraacetic acid (EDTA), and a panel of carbohydrates, including mannose and glucosamine [294]. We confirmed the presence of lectin receptors in hCMEC/D3 cells by western blotting using DEC205 antibodies (**Figure 3.8a**). Furthermore, the accumulation of Mϕ-derived exosomes in hCMEC/D3 cells was decreased by a panel of carbohydrates, the calcium chelator ethylene glycol-bis(2-aminoethylether)-N, N, N', N'-tetraacetic acid (EGTA),

and DEC205 antibodies (**Figure 3.8b, c, d**). Among the carbohydrates, glucosamine inhibited

the uptake of exosomes at much lower concentrations, suggesting that the inhibitory effect

differed from the hyperosmotic effect of sucrose that blocked endocytosis [295]. It was reported

that some carbohydrates, for example glucosamine, inhibit ICAM-1 expression in rat

cardiomyocytes [296] and human retinal pigment epithelial cells [297]. We tested this possibility

and demonstrated that even at the highest concentrations used, glucose and glucosamine did not

inhibit the expression of ICAM-1 in our cell model (**Figure 3.9**). Therefore, in addition to

ICAM-1, specific carbohydrate binding receptors, especially glucosamine-binding C-type lectin

receptors, mediate the accumulation of Mϕ-derived exosomes in hCMEC/D3 cells. The LPS

stimulation did not enhance expression of lectin receptors in hCMEC/D3 cells (**Figure 3.10**),

suggesting that, in contrast to ICAM-1, these receptors are not involved in the increased uptake

of Mϕ exosomes in response to LPS stimulation.
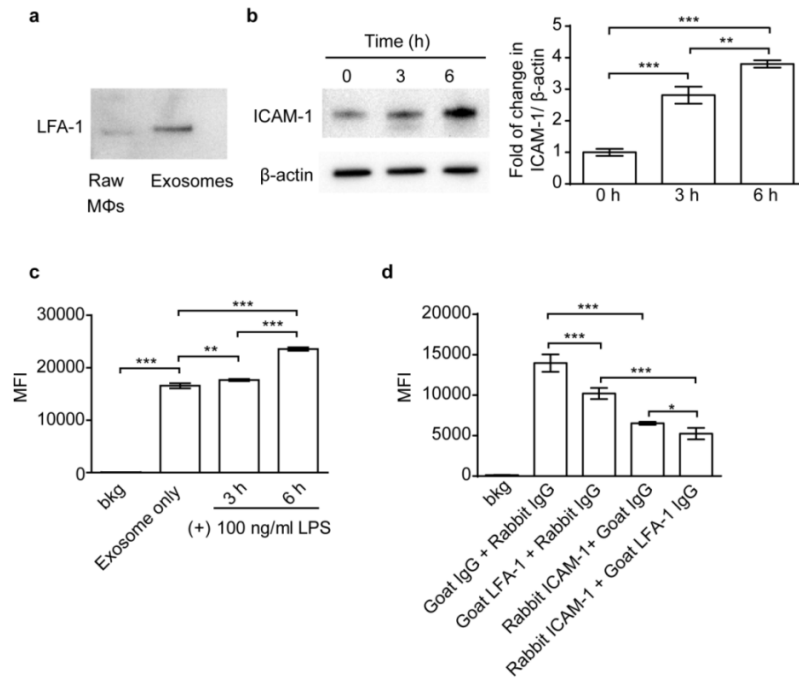
Figure 3.7. ICAM-1/LFA-1 mediate uptake of Mϕ exosomes in hCMEC/D3 cells. (a)
Expression of LFA-1 in Raw Mϕs and Mϕ-derived exosomes by western blotting at equal protein
loading. **(b)** Expression of ICAM-1 in hCMEC/D3 cells in response to 3 or 6 h of stimulation
with LPS (100 ng/ml). **(c)** Uptake of exosomes in hCMEC/D3 cells with or without 3 or 6 h of
LPS stimulation. **(d)** Effect of co-incubation with anti-ICAM-1 or anti-LFA-1 antibodies (100
µg/ml) on cell uptake of exosomes in hCMEC/D3 cells. Cell uptake was determined by flow
cytometry after 4 h incubation with CM-DiI labeled exosomes (0.6×10^{10} exosomes/ml). Data are
MFI ± SD of 5000-10000 live singlets, n = 3, * $p < 0.05$, ** $p < 0.01$ and *** $p < 0.001$ *vs.*
indicated groups by one-way ANOVA and post Newman-Keuls multiple comparison test.
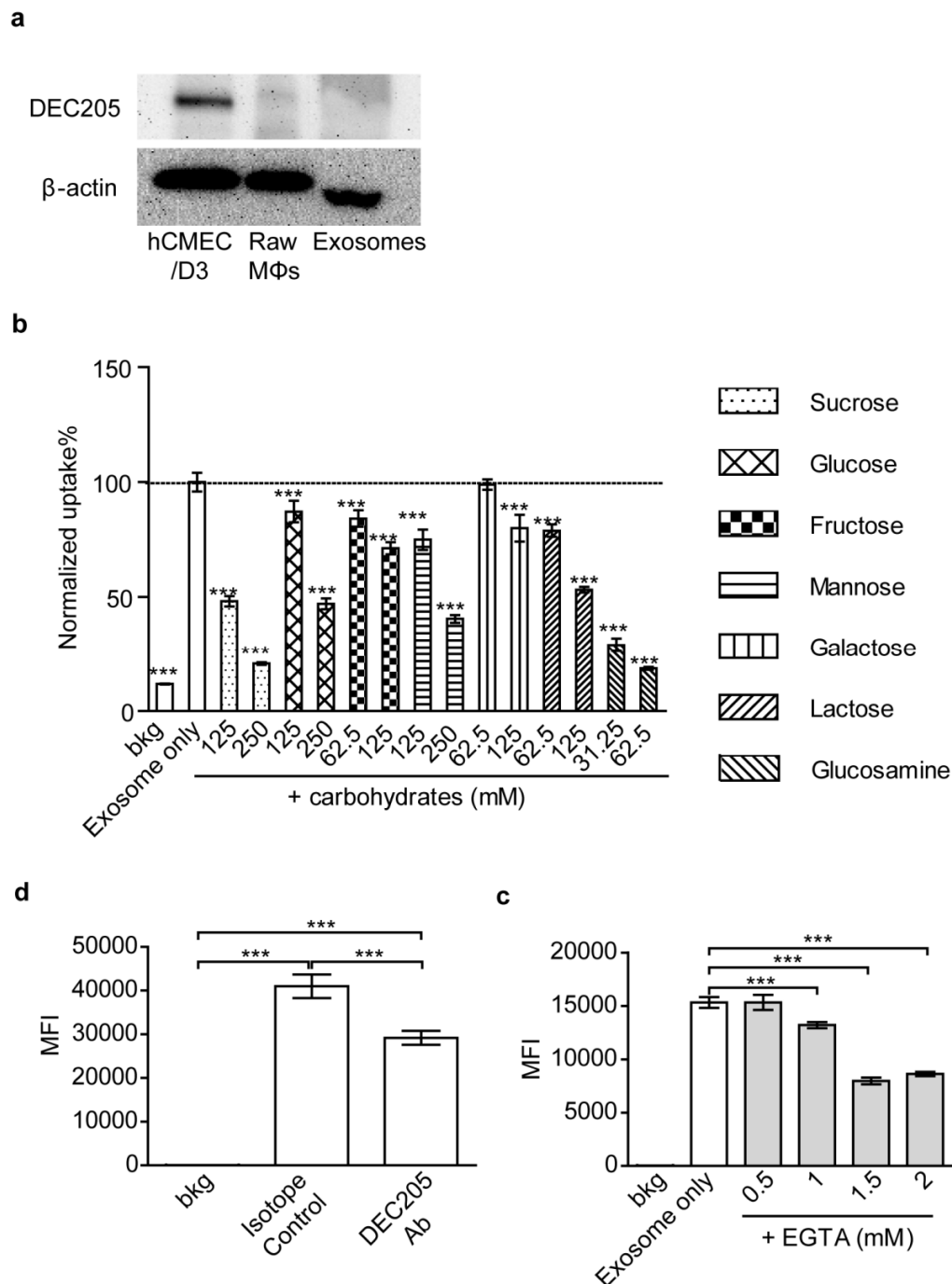
Figure 3.8. C-type lectin receptors mediate uptake of Mφ-derived exosomes in hCMEC/D3 cells. (a) Expression of lectin receptors in hCMEC/D3 cells. Raw Mφs and Mφ-derived exosomes examined by western blotting at equivalent protein loading for C-type lectin receptor (DEC205) at non-reducing condition and β-actin at reducing condition. **(b)** Effect of

carbohydrates on the uptake of exosomes. The carbohydrates were added to cells 0.5 h before and during incubation with exosomes. The data are normalized to the control cells treated with exosomes only. **(c, d)** Accumulation of exosomes in hCMEC/D3 cells in the presence of (c) EGTA and (d) DEC205 antibody (100 µg/ml). In (a, c, d) cells were exposed to CM-DiI labeled exosomes (0.6×10^{10} exosomes/ml) for 4 h and then analyzed by flow cytometry. Data are MFI ± SD of 5000-10000 live singlets, n = 3, *** $p < 0.001$. Statistical comparisons were made by one-way ANOVA and post Newman-Keuls multiple comparison tests. The used concentrations of carbohydrates and EGTA ensured at least 80% cell viability (**Figure 3.4**).
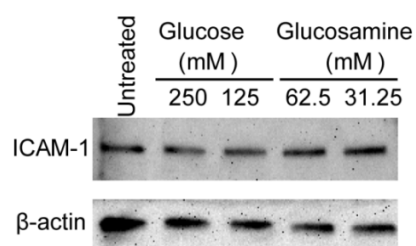
Figure 3.9. Effect of glucose and glucosamine on ICAM-1 expression in hCMEC/D3 cells. Cells were treated with glucose and glucosamine at indicated concentrations for 4.5 h. Protein expression was determined by western blotting using β-actin as loading control.
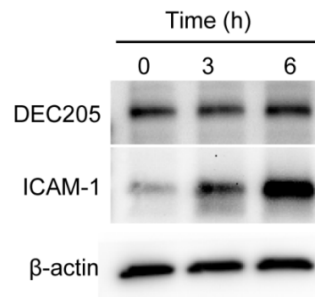
Figure 3.10. Effect of LPS stimulation on expression of lectin receptors (DEC205) and ICAM-1 in hCMEC/D3 cells. Cells were treated with LPS (100 ng/ml) for 3 or 6 h. Protein expression was determined by western blot using β-actin as loading control.

3.3.5. *In vivo* PK and distribution of Mϕ exosomes

Next, we characterized the PK and distribution of Mϕ exosomes in healthy CD-1 mice after IV injection of ^{125}I-radiolabeled Mϕ exosomes along with ^{131}I-labeled BSA as a vascular marker [298]. The labeled exosomes and BSA were separated from free iodine in a Nap-5 column. We characterized the size distribution of exosomes before and after elution to evaluate if the labeling procedure changes the size distribution. The z-average diameter of exosomes was decreased to 116.2 ± 6.2 nm from 147 ± 8.3 nm after elution, suggesting that the size exclusion column removed the large particles. The clearance of both Mϕ exosomes and BSA showed a two-phase decay (**Figure 3.11a**). Their PK parameters are presented in **Table 3.1**. Similar to tumor-derived exosomes [135], Mϕ exosomes mainly accumulated in the liver and spleen at 10 min, 4 h, and 24 h (**Figure 3.11b**), suggesting entrapment of exosomes in the MPS system [299] or their binding with ICAM-1 [147] and lectin receptors [148] expressed in liver and spleen. Accumulation of Mϕ exosomes in the brain at 10 min and 4 h was 0.1% ID/g, and decreased to 0.05% at 24 h, suggesting a slow rate of clearance from the brain. Importantly, 94% of exosomes penetrated the brain accumulated in the brain parenchyma fraction as was shown by the capillary depletion assay (**Figure 3.11c**).
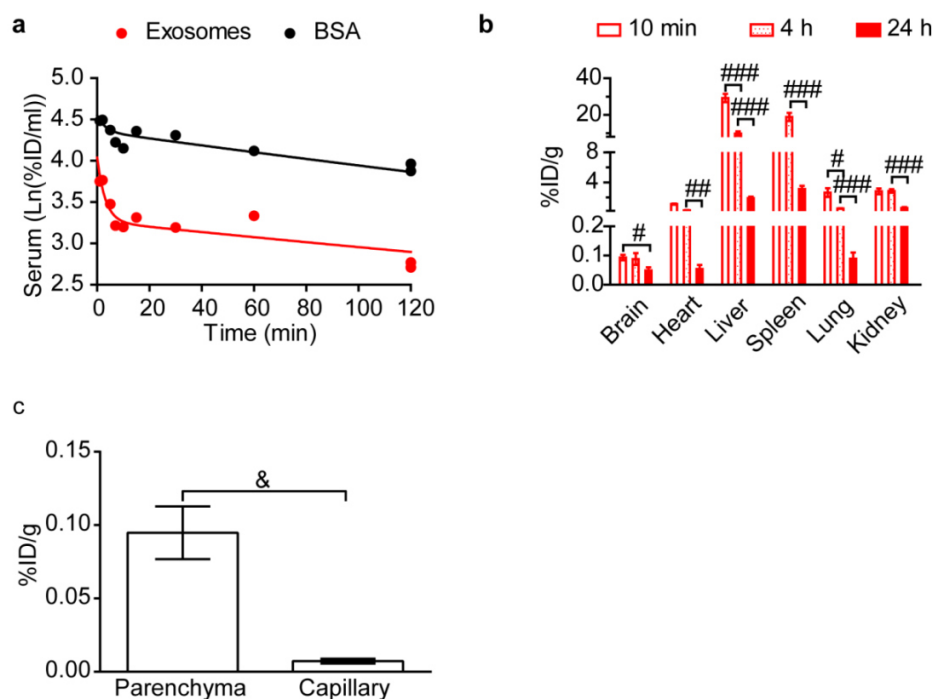
Figure 3.11. PK and distribution of Mϕ exosomes in healthy CD-1 mice. The mice were co-injected with ^{125}I-exosomes and ^{131}I-BSA *via* jugular vein. **(a)** Clearance of exosomes and BSA. **(b)** Tissue distribution of exosomes. Tissue accumulation was corrected for vascular space using BSA data. Data are means ± SEM, n = 3-6. # $p < 0.05$, ## $p < 0.01$, and ### $p < 0.001$ *vs.* indicated group by unpaired two-tailed t-test. **(c)** Brain distribution of Mϕ exosomes at 10 min. Data are means ± SEM, n = 4, & $p < 0.05$ by paired two-tailed t-test.

Table 3.1. Noncompartmental PK parameters of Mϕ exosomes and BSA in healthy CD-1 mice.

	Cl (ml/min)	Vss (ml)	MRT$_{last}$ (h)	MRT$_{inf}$ (h)
^{125}I-Exosomes	0.016	3.15	0.91	3.40
^{131}I-BSA*	0.0039	1.44	0.94	6.10

*The Cl and Vss of BSA were consistent with the previous publications (0.0035 ml/min and 1.5 ml) [300].

To examine whether the inflammation increases the homing of Mϕ-derived exosomes to the brain, we compared the PK of Mϕ exosomes in healthy mice and in mice with LPS-induced encephalitis, a mouse model of brain inflammation [301]. The clearance of exosomes and co-injected BSA in the brain-inflamed mice resembled those in the healthy mice (**Figure 3.12a**). Both healthy and brain-inflamed mice showed a statistically significant net brain influx of exosomes (**Figure 3.12b**): the slopes (Ki) of the delta brain/serum ratios plotted against exposure time significantly deviated from zero ($p < 0.05$), thus demonstrating net brain influx. The Ki and initial Vi of exosomes in the brain-inflamed mice were respectively 3- and 2-fold higher than those in the healthy mice. The plot of the delta brain/serum ratios against serum concentrations directly demonstrated increased accumulation of Mϕ-derived exosomes in the inflamed brains at similar serum concentrations of exosomes (**Figure 3.12c**). In addition, the brain influx rates of BSA in the brain-inflamed and healthy mice were comparable ($p = 0.076$, **Figure 3.12d**), suggesting that the increase in the brain influx of exosomes under inflammation was not caused by BBB disruption. Consistent with the increased brain influx rate, the brain accumulation of Mϕ exosomes in the inflamed brain at 10 min was 5.8 fold higher than that in the healthy mice (**Figure 3.12e**). These results are consistent with our *in vitro* finding of an increased accumulation of exosomes in LPS treated brain endothelial cells (**Figure 3.7c**). As the expression of ICAM-1 in brain endothelium increases during inflammation, the adhesion and potential brain accumulation of exosomes through LFA-1/ICAM-1 interaction could also increase. This process may have some commonality with the increased brain infiltration of Mϕs upon inflammation [99, 280]. The mouse model of LPS-induced encephalitis also displayed significantly higher accumulation of Mϕ exosomes in the heart (1.6 fold), lungs (7.1 fold) and kidneys (3.9 fold) (**Figure 3.12e**). This could be explained by peripheral inflammation resulting

from the absorption of LPS from the brain CSF to the blood [285] and/or activation of microglia and release of other inflammatory cytokines to the peripheral [302, 303]. Zhou et al. showed that ICV injection of LPS at a lower dose (2 µg) activates microglia as well as peritoneal macrophage, clearly suggesting that a peripheral inflammation process does occur after brain local injection of LPS [303]. Th*e* inflammation-responsive brain distribution of Mϕ exosomes is remarkable and provides a strong rationale for their potential application as natural nanocarriers for neurodegenerative disorders commonly accompanied with brain inflammation.
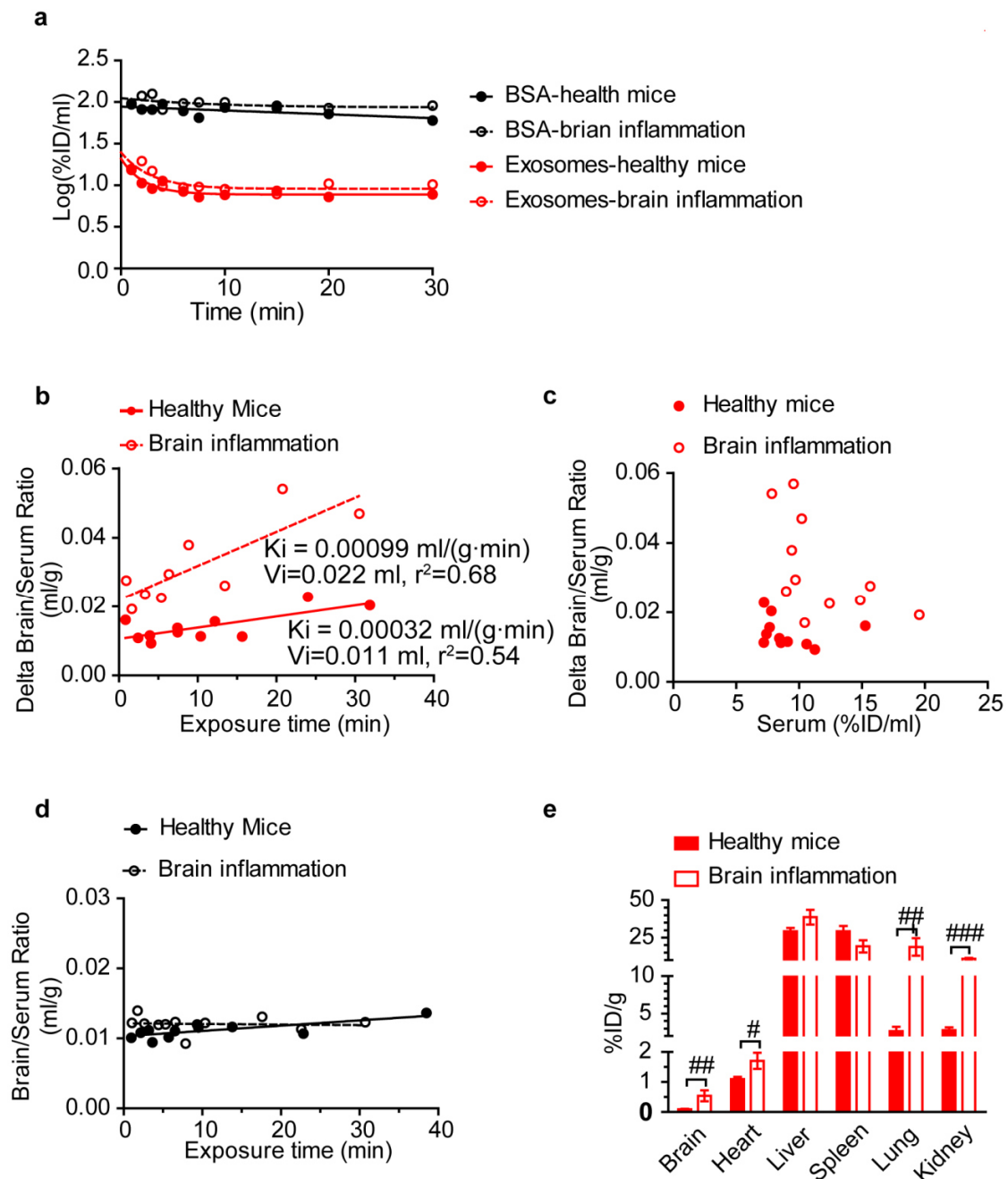
Figure 3.12. Comparision of PK and distribution of Mφ exosomes in healthy and brain-inflamed CD-1 mice. The brain inflammation in CD-1 mice was induced by intracranial injection of 10 μg LPS 24 h before the exosome administration. The mice were co-injected with ^{125}I-exosomes and ^{131}I-BSA *via* jugular vein. **(a)** Clearance of exosomes and BSA in healthy mice and brain-inflamed mice. **(b)** Multiple-time regression analysis of exosomes for brain influx rate in healthy and brain-inflamed mice. Delta brain/serum ratios were calculated by subtracting the brain/serum ratios of BSA from those of exosomes to correct for vascular space

[285]. n = 1 per time point. **(c)** Plot of delta brain/serum ratios of Mϕ exosomes against serum concentrations of Mϕ exosomes. **(d)** Multiple-time regression analysis of co-injected BSA for brain influx rate in healthy and brain inflamed mice. n = 1 per time point. Both slops are comparable to zero. **(e)** Distribution of exosomes at 10 min. Tissue accumulation was corrected for vascular space using BSA data. Data are means ± SEM, n = 3-6. # $p < 0.05$, ## $p < 0.01$, and ### $p < 0.001$ *vs.* indicated group by unpaired two-tailed t-test.

3.3.6. Mφ exosomes deliver a protein cargo to the brain

To determine whether Mφ exosomes could deliver cargo to the brain, we loaded them with

BDNF as a model protein by simple mixing of the exosomes and BDNF in 10 mM phosphate

buffer (pH 7.4). The binding of BDNF (isoelectric point 9.99) [304] with the negatively charged

exosomes (zeta potential -18 mV) by electrostatic and polysaccharide interactions [305, 306]

formed a BDNF-exosome complex (ExoBDNF), which was confirmed using Protein G-magnetic

beads coupled with BDNF antibodies (**Figure 3.13a**) and native polyacrylamide gel

electrophoresis (PAGE) (**Figure 3.13b**). The latter indicated that Mφ-derived exosomes can

capture as much as 20 % by weight of BDNF relative to its own protein. Characterized by DLS,

the z-average diameter of exosomes, ExoBDNF, and BDNF in one batch were 147.0 ± 8.3 nm,

209.5 ± 4.7 nm, and 36.1 ± 13.5 nm. The increase in diameter, the pull-down assay, and the

native electrophoresis all support that BDNF can associate with exosomes by simple mixing.

Interestingly, ExoBDNF released BDNF upon binding with the BDNF receptor TrkB. We mixed

ExoBDNF with increasing amount of TrkB-Fc fusion proteins, and then resolved the proteins in

native agarose gel electrophoresis. In this experiment (**Figure 3.14a**), BDNF was retained in the

loading well, but migrated toward cathode upon binding with TrkB-Fc at a slower rate than free

TrkB-Fc. ExoBDNF was also retained in the well, but TrkB-Fc could extract BDNF from

ExoBDNF as the band for BDNF-TrkB-Fc complex increased in intensity, and the amount of

BDNF that was retained in the well was decreased. Moreover, ExoBDNF activated TrkB

receptors and downstream Akt signaling in NIH-3T3-TrKB cells comparably to unformulated

BDNF (**Figure 3.14b**, **c**). ExoBDNF-induced phosphorylation of TrkB receptors and Akt can be

blocked by the excess of TrkB-Fc proteins. This suggests that the signaling induced by

ExoBDNF was mediated by TrkB receptors, which probably have superior affinity with respect

to BDNF than the exosomes. Overall, we demonstrated that functional BDNF could be loaded onto Mϕ-derived exosomes and released in the presence of TrkB receptors in the target brain tissues.

We further determined whether Mϕ-derived exosomes facilitate BDNF transfer to the brain. In this experiment, we co-injected [131]I- BSA and ^{125}I-BDNF with or without exosomes into the jugular vein of healthy CD-1 mice. The brain/serum ratios of BDNF loaded onto exosomes were significantly higher than those BDNF alone (**Figure 3.15a**). Importantly, 89% and 95% of the BDNF accumulated in the brain distributed to the brain parenchyma in the BDNF alone group and ExoBDNF group (**Figure 3.15b**), suggesting that both BDNF alone and BDNF in ExoBDNF group can penetrate the BBB. In addition, brain accumulation of ExoBDNF in the parenchyma fraction was significantly higher than BDNF alone in healthy mice. To the contrary, the brain influx rates of co-injected BSA in both groups were comparable and did not differ from 0 (**Figure 3.15c**). The brain/serum ratios of BSA in both groups were similar as well (**Figure 3.15d**). These data also indirectly suggested that BDNF at least in part remained with exosomes after administration *in vivo*. We also found that ExoBDNF complex was stable in the presence of NaCl up to the highest tested concentration of 1 M (**Figure 3.16**).
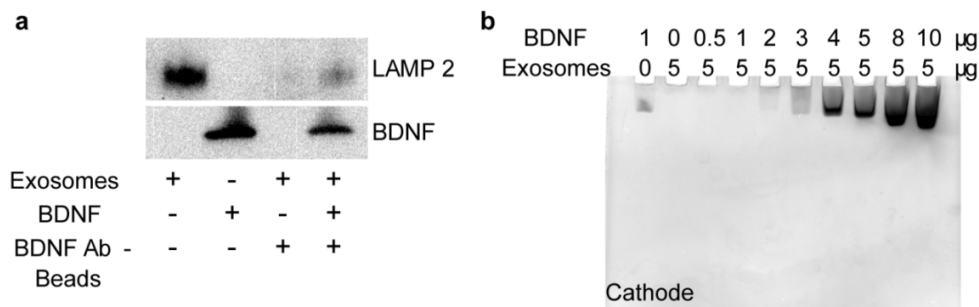
Figure 3.13. Formation of ExoBDNF complex. (a) ExoBDNF were isolated using protein G magnetic beads modified with BDNF-specific antibodies. The presence of LAMP 2 in the magnetic bead-separated fractions indicated that the exosomes were captured on the beads. A control group of exosomes without BDNF treatment was used to account for nonspecific binding. **(b)** Native PAGE of the mixtures of Mϕ exosomes and BDNF at different protein ratios. Exosomes prevented the neurotrophic factor migration in the gel toward the cathode up to a BDNF: exosomal protein weight ratio of 1:5.
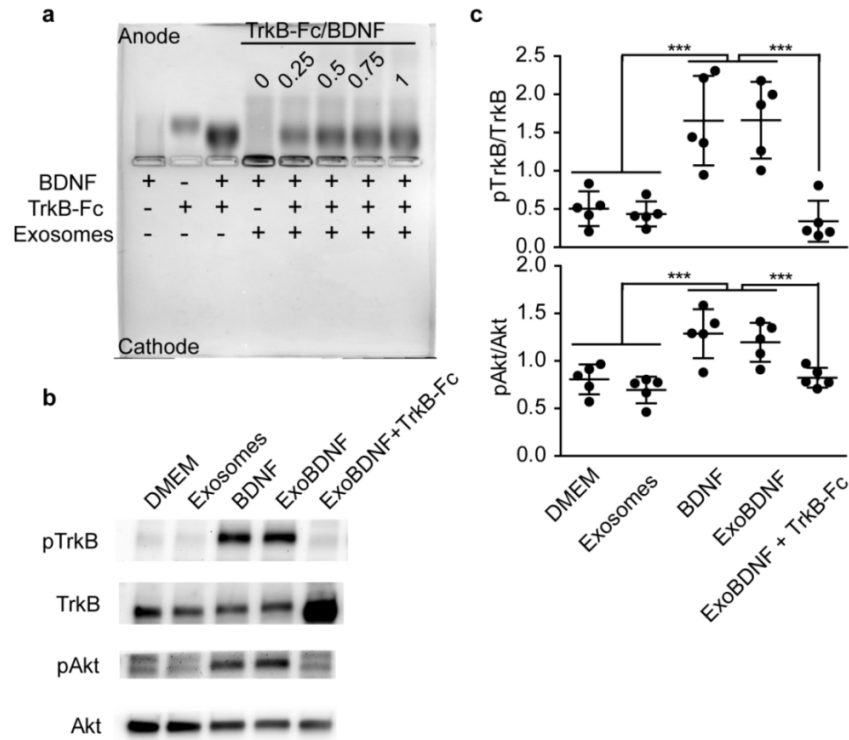
Figure 3.14. Dissociation of BDNF and exosomes by BDNF receptors. (a) Native agarose gel electrophoresis of ExoBDNF in the presence of increasing amount of TrkB-Fc. **(b)** Western blotting analysis of the activation of TrkB receptors and Akt signaling in NIH-3T3-TrkB cells by different treatments. The cells were treated with BDNF or ExoBDNF at 500 ng/ml of BDNF for 5 min in the absence or presence of 5 molar equivalents of TrkB-Fc. **(c)** Densitometry analysis of the western blotting in (b) using Image J. Data are means ± SD, n = 5, *** $p < 0.001$ *vs.* indicated groups by one-way ANOVA and post Newman-Keuls multiple comparison test. Note that residual TrkB-Fc increased the band intensity of TrkB in the ExoBDNF +TrkB-Fc group.
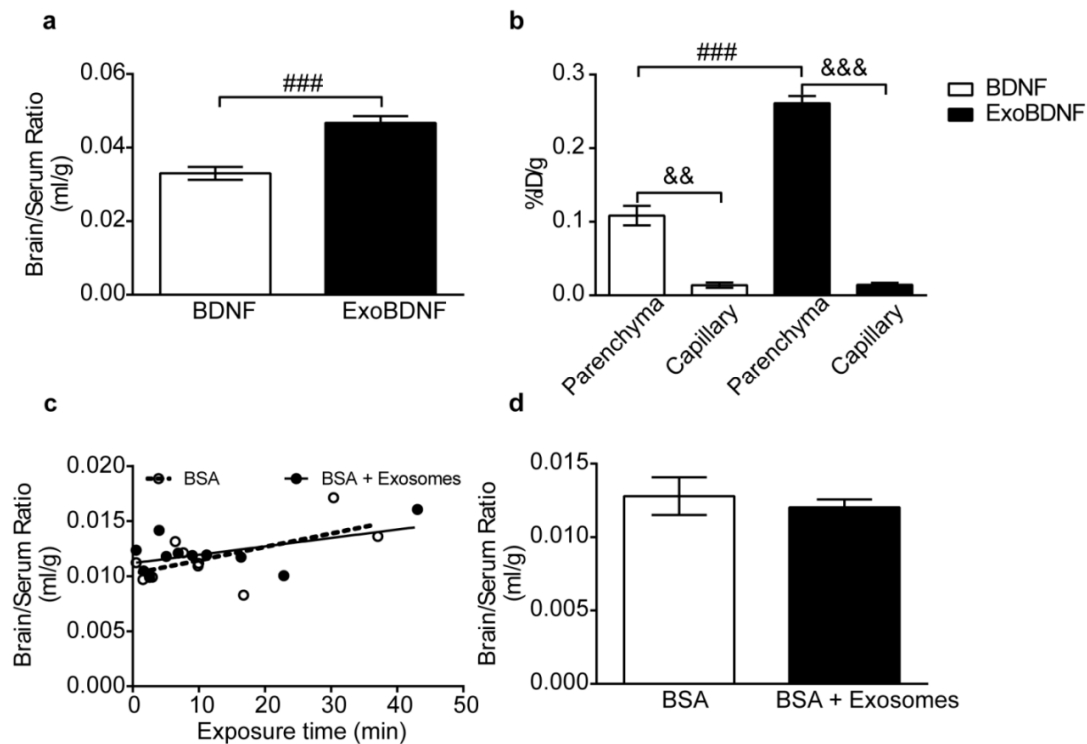
Figure 3.15. Brain delivery of ExoBDNF complex in healthy mice. The mice were co-injected with ^{131}I-BSA and ^{125}I-BDNF with or without Mϕ exosomes *via* jugular vein. **(a)** The brain/serum ratios of ^{125}I-BDNF at time points of 1, 2, 3, 4, 5, 6, 7.5, 10, 15, 20, 30 min were averaged. ### $p < 0.001$ by unpaired two-tailed t-test. **(b)** Distribution of BDNF or BDNF in ExoBDNF in brain parenchyma at 10 min determined by capillary depletion assay. Data are means ± SEM, n = 5, && $p < 0.01$ and &&& $p < 0.001$ by paired two-tailed t-test, ### $p < 0.001$ by unpaired two-tailed t-test. **(c)** Multiple-time regression analysis of co-injected BSA in healthy mice. Both slopes are comparable to 0 ($p = 0.064$ for BSA and $p = 0.09$ for BSA + Exosomes). **(d)** The brain/serum ratios of ^{131}I-BSA at time points of 1, 2, 3, 4, 5, 6, 7.5, 10, 15, 20, 30 min were averaged.
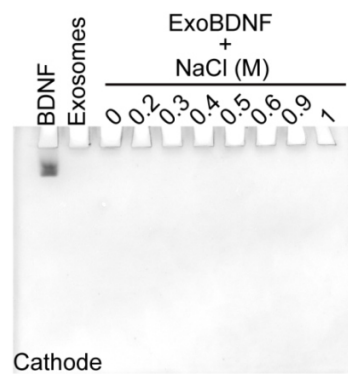
Figure 3.16. Native PAGE of ExoBDNF in the presence of salt. ExoBDNF was formed at BDNF: exosome protein weight ratio of 1:5.

We further compared the brain accumulation of naked and exosome-formulated BDNF in healthy and brain-inflamed mice (**Figure 3.17**). The brain accumulation of exosome-formulated BDNF in healthy mice was slightly but not significantly increased compared to BDNF alone ($p = 0.63$). Brain inflammation resulted in a trend to increase the brain accumulation of free BDNF but the difference was not significant when compared to the healthy mice ($p = 0.11$). In contrast, accumulation of exosome-formulated BDNF (ExoBDNF) in the brain-inflamed mice was significantly increased compared to the same formulation in the healthy animals (3.6 fold). Moreover, the brain accumulation of BDNF with this formulation was also superior to that of the BDNF alone in the inflamed brain (2.2 fold).
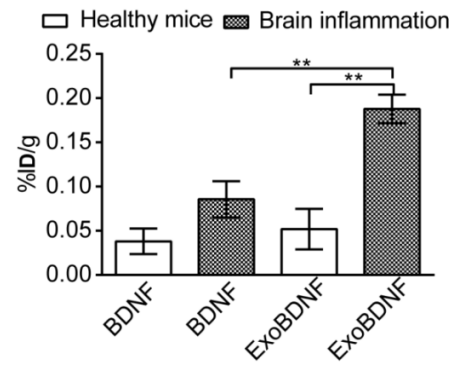
Figure 3.17. Brain accumulation of ExoBDNF complex. The mice were co-injected with ^{131}I-BSA and ^{125}I-BDNF with or without Mϕ exosomes *via* jugular vein. BSA data were used to correct for the vascular space. Brain accumulation of ^{125}I-BDNF or ^{125}I-BDNF in ExoBDNF in healthy or brain-inflamed mice at 10 min. Data are means ± SEM, n = 4, ** $p < 0.01$ indicated group by one-way ANOVA and post Newman-Keuls multiple comparison test.

3.4. Discussion and conclusion

To summarize, we isolated exosomes from Raw Mϕs and characterized their interaction with immortalized human brain endothelial cells (hCMEC/D3 cells) *in vitro*, and their PK in mice with or without brain inflammation. *In vitro*, we first showed that hCMEC/D3 cells internalized Mϕ exosomes in a saturable manner using multiple pathways (clathrin-/caveolae-mediated endocytosis, and macropinocytosis), implying a possible receptor-mediated pathway. We then confirmed that Mϕ-derived exosomes inherited LFA-1 from their parental cells, a protein that interacts with endothelial ICAM-1 and mediates the lateral migration and diapedesis of Mϕs across the BBB [96]. More importantly, the LFA-1 and ICAM-1 also mediated cellular uptake of Mϕ-derived exosomes in hCMEC/D3 cells. The cellular uptake of exosomes increased significantly under inflammation conditions in response to overexpression of ICAM-1 receptors on endothelial cells, resembling the increased diapedesis of Mϕs across the BBB under inflammation. We also identified that cellular uptake of Mϕ-derived exosomes in hCMEC/D3 cells involves C-type lectin receptors, because various carbohydrates, specific antibodies, and calcium chelators blocked the accumulation. However, the C-type lectin receptors were not responsible for the increased cellular uptake under inflammation. *In vivo*, we demonstrated that IV administered Mϕ-derived exosomes penetrated the BBB to the brain parenchyma in healthy mice. Although these exosomes mainly distributed in the liver and spleen, they also accumulated in brain as high levels as 0.1 ID%/g, and were slowly cleared from the brain. Consistent with increased cellular uptake under inflammation, Mϕ-derived exosomes entered the brain 3.1-fold faster and accumulated 5.8-fold greater in the inflamed brain than in the healthy brain, without increasing accumulation in liver and spleen. Strategies to reduce uptake by the MPS such as PEGylation can be explored in the future to shield exosomes and extend circulation time in order

to further improve brain accumulation. Furthermore, we loaded a model cargo protein radiolabeled BDNF onto Mφ exosomes and showed that they successfully delivered BDNF to the brain parenchyma in healthy mice, and even at greater extent to the brain with inflammation (0.19 ID%/g). Noteworthy, our findings contradict with the results reported by Hwang et al.[141]. This report indicated that technetium-radiolabeled Mφ exosomes and the Mφ extruded membrane vesicles showed no detectable signal in the brain region of BALB/c mice obtained by single photon emission computed tomography (SPECT) [141]. This discrepancy can be possibly explained by the higher sensitivity of iodine detection method and difference in size distribution. Compared to exosomes utilized in this investigation (130 nm), the Mφ-derived extruded membrane vesicles had larger average diameter (218 nm), which may result in increased sequestration in peripheral organs causing lower brain transport. Besides, our study was consistent with the study showing that fluorescently labeled exosomes released from autologous dendritic cells was detectable in mouse brains 24 h after IV injection [142] and the study showing that exosomes from HEK cells can penetrate inflamed BBB endothelial cells in vitro using a transcellular route [307].

Although we did not specifically evaluate the blood-CSF barrier (choroid plexus or ependymal barrier), our in vivo model can reflect an influence of that barrier. The vascular barrier is usually thought to be the preferred route for drug delivery because of its proximity to the neurons and the blood-CSF barrier is generally assumed to primarily inventory the vascular BBB [2, 3, 7], however, such a view can underestimate the importance of the choroid plexus. We showed in vitro that exosomes can be internalized into human brain endothelial cells. Therefore, we conclude that exosomes can penetrate the vascular barrier, but can make no conclusions regarding their ability to penetrate the blood-CSF barrier.

The Raw 264.7 Mϕ exosomes, which originate from BALB/c mice, were tested in a different murine strain (CD-1 mice). Possibly, these exosomes are cleared faster in CD-1 mice than in autologous BALB/c mice due to immune response. However, recent publications demonstrate that exosomes from different species (human, rat, or mouse) and exosomes from different mouse strains all show rapid clearance and sequestration by MPS organs such as liver, spleen, and lung in mice [135, 141-145]. These data indicate that exosomes may not readily avoid the MPS sequestration as assumed from their wide existence in biological fluids and their "self" nature. If accelerated clearance in CD-1 mice did occur, we would expect higher brain uptake of these exosomes in BALB/c mice as a result of longer exposure to the BBB. As gender difference in inflammatory response [308] and in the brain transduction of adeno-associated virus serotype 9 [309] has been reported, it would be interesting to investigate the potential gender influence in brain penetration of exosomes.

The ability of Mϕ exosomes to cross the BBB and ferry a cargo to the brain parenchyma especially under brain inflammation, a common condition associated with many CNS disorders [92], can be explored to deliver various disease-modulating proteins to the brain. In addition to the natural tropism, another benefit of exosomes over artificial drug carriers is the feasibility of having genetically modified parent cells as a factory continuously secreting active therapeutic proteins into exosomes. Moreover, exosomes mediated cargo transfer from transplanted Mϕs to contiguous brain resident cells, such as endothelial cells and neurons [102, 105, 108, 109], and spreading of disease-relevant proteins inside the brain and into CSF [124, 281], suggesting exosomes may facilitate drug distribution in the brain upon penetrating the BBB. Taken together, Mϕ-derived exosomes are promising nanocarriers for brain delivery of therapeutic proteins.

CHAPTER IV: SUMMARY, SIGNIFICANCE, AND FUTURE DIRECTION[4]

Proteins are an important class of therapeutics to treat CNS disorders. However, therapeutic proteins can hardly penetrate the BBB to reach the brain at therapeutic concentrations. In this dissertation, first, I review with published examples the current strategies used to deliver therapeutic proteins to the brain, including strategies that can disrupt the BBB, penetrate the BBB, or bypass the BBB. Furthermore, the *pros* and *cons* and design parameters that one need to take into account and optimize for each brain delivery strategy are summarized.

Second, I look into the brain delivery problems of leptin, a potential treatment for obesity. Leptin enters the brain by a saturable transporter system on the BBB and acts in the brain to regulate feeding and thermogenesis. However, its brain entry is impaired in overweight and moderately obese patients. Previously, we modified the lysine amines of leptin with P85 to enhance the protein penetration across the BBB. We found that this modification results in random modification at five lysine amines in leptin and significant loss of activity. The results are published in Journal of Controlled Release (doi: 10.1016/j.jconrel.2014.05.044.). I was listed as the second author for my contribution in the synthesis, purification, and characterization of the conjugates. I characterized the polymer conjugation sites using LC-MS/MS, the secondary structure of leptin and leptin conjugates using CD, and the stability of the disulfide bond in human serum using western blotting. These data are not included in this dissertation.

---

[4] The figures and table of this chapter previously appeared as part of a manuscript soon to be submitted. The original citation is as follows: Yuan, D et al. "", xxxxxx, 2017, xxxxxx.

We continue to improve the leptin conjugate system for brain delivery of leptin. In Chapter II, I optimize the conjugation chemistry to restrict the P85 attachment to the N-terminal amine of leptin. The leptin N-terminal P85 conjugate (LepNP85) has higher homogeneity, binding affinity to leptin receptor, and net brain influx rate than the random lysine conjugates. However, this advanced form of leptin-P85 conjugate enters the brain dependently on the transporter which is impaired in the target patient population. Hence the conjugate was administered intranasally to bypass the BBB. I compared the brain uptake of the unmodified leptin, LepNP85, the N-terminal conjugate with PEG, and the random lysine conjugates with P85 using cleavable and non-cleavable linkers following intranasal administration. I found that the conjugates have direct access to the brain from the nose and that LepNP85 has higher nose-to-brain transport than unmodified leptin and other forms of leptin conjugates. Due to the improved nose-to-brain delivery, LepNP85 activates the leptin receptor in brain hypothalamus at two fold-lower dose than unmodified leptin. As the intranasal transport of LepNP85 to the brain was independent of the leptin receptor, the improvement made by P85 modification in nose-to-brain transport could be possibly extended to other therapeutic proteins.

It would be interesting to screen other Pluronics or polymers with different values of hydrophilic-lipophilic balance (HLB) to optimize the nose-to-brain delivery of leptin. Perhaps conjugation with more hydrophobic polymers could further enhance the intranasal delivery of leptin to the brain. However, it is reasonable to suspect that conjugation with hydrophobic polymers may disturb the structure of leptin and enhance protein aggregation. To determine the effect of P85 modification on protein stability, I monitored the change of leptin's intrinsic fluorescence upon heat-induced protein unfolding using NanoDSF (**Figure 4. 1** and **Table 4.1**). Compared to the unmodified leptin and the mixture of leptin and P85, LepNP85 unfolds at lower

temperature and fails to refold upon cooling. This likely suggests that the hydrophobic PPO block in P85 when in close proximity with leptin (compared to the mixture) facilitates the protein unfolding and stabilizes the unfolded proteins to prevent refolding by interacting with the hydrophobic patches on the protein. Unexpectedly, LepNP85 has lower PDI and less aggregation peaks than leptin at 25 °C. The proteins were stressed by five repeated freeze and thaw to induce aggregation. Both leptin and LepNP85 have no change in their size distribution, and LepNP85 still has less aggregation than leptin after repeated freeze and thaw (**Figure 4. 2**). This suggests that LepNP85 has better colloidal stability than leptin. The hydrophobic interaction between the PPO block and the surface hydrophobic patches of leptin and the shielding effect of the PEO blocks may prevent the formation of intermolecular protein aggregates. It would be interesting to compare the colloidal stability of leptin and LepNP85 after long-term storage at 4 °C and 25 °C. Likely LepNP85 only has stability issue under heating, a condition which dehydrates P85 and denatures the polypeptide chain of leptin leading to increased hydrophobic interaction between the protein and P85. Therefore, the ideal amphiphilic polymer for leptin conjugation should be selected based on the brain delivery efficiency and the conjugate stability.
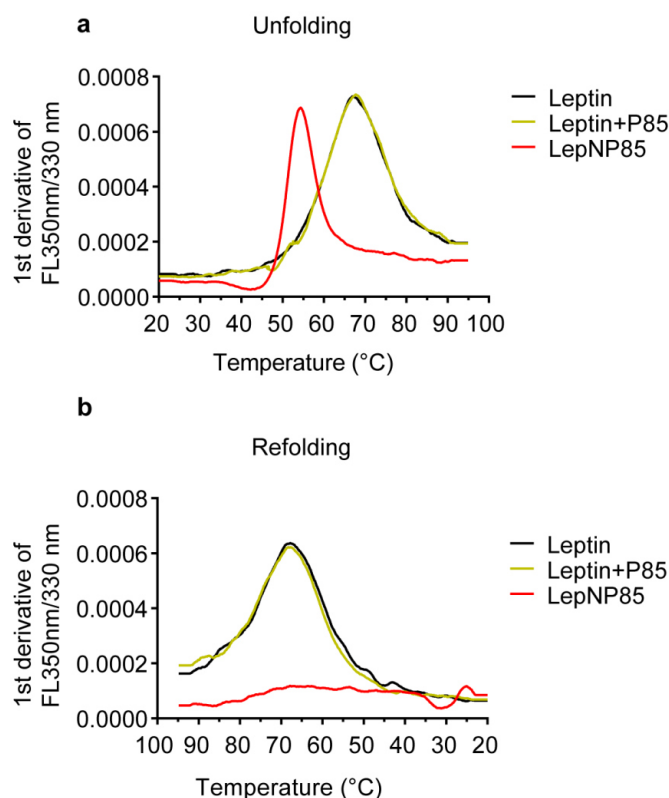
Figure 4.1. Structural change of leptin and LepNP85 upon heating and cooling. Leptin, LepNP85, and a mixture of leptin and P85 at 1:1 molar ratio in 10 mM sodium phosphate, pH 7.5 at protein concentration of 0.5 mg/ml were heated from 20 °C to 95 °C at a heating rate of 1 °C/min and then cooled to 20 °C at a cooling rate of 1 °C/min. The intrinsic fluorescence of leptin was monitored at 330 nm and 350 nm after excitation at 285 nm (excitation power 100%) using a NanoDSF instrument (Prometheus NT. 48, NanoTemper). Upon heat-induced protein unfolding, the embedded aromatic amino acids will be exposed to the aqueous environment leading to shift of the maximum fluorescence emission from 330 nm to 350 nm. By monitoring the change in fluorescence at 350 nm and 330 nm, we can monitor the unfolding and refolding process of proteins. The first derivatives of the ratio of fluorescence at 350 nm/330 nm were plotted against temperatures to determine the onset temperature of unfolding, midpoint of unfolding transition (Tm), and the refolding temperature. **(a)** Heat-induced protein unfolding. **(b)** Protein refolding under cooling.

Table 4.1. The unfolding onset temperature and Tm of leptin and LepNP85.

	Leptin	Leptin + P85	LepNP85
Onset*, °C	48.0 ± 0.2	48.5 ± 1.4	35.9 ± 2.2
Tm*, °C	67.5 ± 0.2	67.9 ± 0.6	54.3 ± 0.1

*Values are mean ± SD of three repeated NanoDSF measurements.
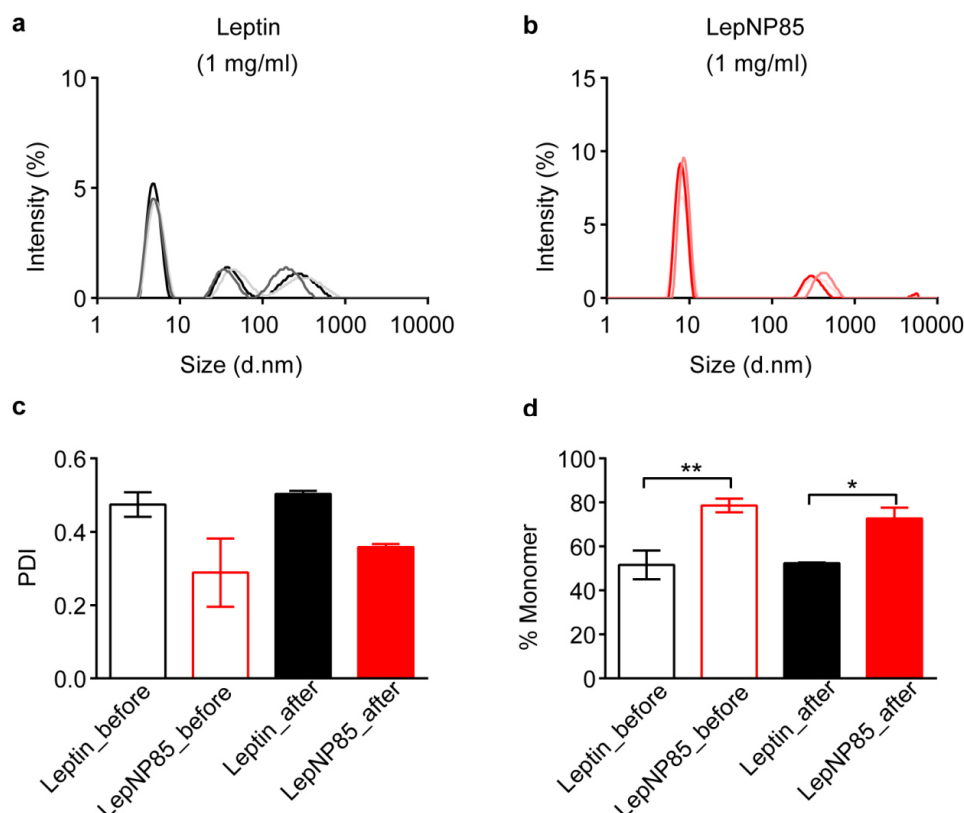
Figure 4.2. Size distributions of leptin and LepNP85 by DLS after five repeated freeze and thaws. The proteins at protein concentration of 1 mg/ml were frozen at -80 °C and thawed at RT (23 °C) repeatedly for five cycles. The size measurements were conducted using Zetasizer Nano-ZS instrument (Malvern, UK) at the default scattering angle of 173°at 25 °C. Intensity weighted size distribution of leptin **(a)** and **(b)** LepNP85. Three repeated measurements after repeated freeze and thaw were shown in different colors for each protein. **(c)** PDI and **(d)** percentage of the main peak (monomer) before and after repeated freeze and thaw. Data are mean ± SD, n=3, * $p < 0.05$ and ** $p < 0.01$ unpaired two-sided t-test.

Furthermore, LepNP85 does not improve the brain retention of leptin and is cleared from the brain within 4 h, thus requiring frequent dosing. It is possible that an intranasal depot system that can continuously release the conjugate in the nasal cavity could prolong the therapeutic effect and reduce the dose frequency.

In Chapter III, I investigated if Mϕ exosomes can penetrate the BBB and act as brain delivery nanocarriers for therapeutic proteins. This is inspired by the brain homing property of Mϕs. We suspect Mϕ exosomes by inheriting surface properties and biological functions from their parent cells can mimic Mϕs and penetrate the BBB. To test this possibility, I characterized the interaction of Mϕ exosomes with human brain endothelial cells *in vitro* and the brain PK of Mϕ exosomes in mice. *In vitro*, I showed that the endothelial cells internalize Mϕ exosomes using multiple endocytosis pathways in a saturable manner. The cell uptake is mediated partially by the interaction between endothelial ICAM-1 and the LFA-1expressed on exosomes, the same interaction that mediates the diapedesis of Mϕs across the BBB. Under inflammation when the endothelial cells upregulate ICAM-1 expression, the cell uptake of Mϕ exosomes increases, resembling the increased diapedesis of Mϕs across the BBB under brain inflammation. Also, the interaction between endothelial lectin receptor and exosomal surface carbohydrates mediates the cell uptake, but this interaction is not responsible for the increased uptake under inflammation. *In vivo*, I showed that Mϕ exosomes penetrate the BBB to the brain parenchyma in healthy CD-1 mice and enter the brain to a greater extent in a neuroinflammation model. Furthermore, I loaded a model protein cargo, BDNF onto the exosome surface, and showed that these exosomes facilitate the brain penetration of BDNF in both healthy mice and brain-inflamed mice. Taken together, we showed that Mϕ exosomes can penetrate the BBB and ferry a cargo to the brain

parenchyma, suggesting that these exosomes are potential brain delivery nanocarriers. We can genetically engineer the cells to have the cells continuously secrete the exosomes containing the therapeutic proteins *in vitro*, and then dose the patients with these exosomes. Alternatively, we can implant the engineered cells and have the cells release the therapeutic exosomes *in vivo* to reduce the dosing frequency.

One limitation of the exosome therapy is that exosomes are sequestered by peripheral MPS organs, which limits the amount of exosomes available for brain uptake and leads to peripheral toxicity. Strategies such as insertion of PEG-lipid conjugates to shield exosomes from MPS recognition can be explored in the future to extend the circulation time and improve brain uptake. However, the effect of PEGylation on exosome brain penetration should be investigated simultaneously. In the case of peripheral inflammation when the peripheral vasculatures upregulate ICAM-1 expression, exosomes may be further diverted to the inflamed peripheral organs from the brain. Therefore, for CNS drugs that exert significant peripheral toxicity, it is critical to characterize the inflammation components in peripheral as well as in brain under disease states. Surface engineering strategies such as decoration with brain targeting ligands may be explored to improve the brain selectivity.

Since exosomes cannot readily avoid MPS sequestration, exosomes can be internalized by circulating immune cells and delivered to the brain by the cell carriers, which may in part contribute to the brain uptake of exosomes. To test if exosomes penetrate the BBB independently of the cell carriers, we can perform a brain perfusion experiment *via* the carotid artery using exosomes suspended in a physiological buffer and determine if the exosomes can enter the brain. This experiment is currently undergoing in Dr. Banks' laboratory. Additionally, we can deplete the circulating immune cells using clodronate liposomes and compare the brain uptake of

exosomes to that in animals treated with control liposomes. However, clodronate liposomes also deplete tissue Mφ [310] and likely increase the brain uptake of exosomes by limiting the peripheral sequestration, which makes it difficult to interpret the function of circulating immune cells.

As discussed in Chapter I, Mφs of different polarized phenotypes differ in their brain permeability and intrinsic biological functions. It would be interesting to compare the brain permeability of exosomes secreted from M1 and M2 Mφs. Given that the brain entry mechanism is based on ICAM-1/LFA-1 interaction, exosomes from other cell lines, especially other immune cells such as dendritic cells, may express LFA-1 and penetrate the brain as well. The selection of cell origins should be based on the brain homing property as well as the intrinsic biological functions of released exosomes, which could be either beneficial or detrimental to the desired therapy.

APPENDIX

This appendix describes the PK data analysis partially adapted from Dr. William Banks's laboratory in University of Washington.

1. Multiple-time regression analysis for calculation of unidirectional brain influx rate (Ki) and initial volume of brain distribution

Purpose:

The Ki, measured in ml/g•min, represents the rate at which compounds are moving from the blood circulation to the brain parenchyma. The Vi, measured in ml, represents the apparent volume of brain distribution, which includes the vascular space and steady-state exchangeable space that was quickly equilibrated with the blood, such as binding at the brain endothelial cells [246, 258].

Animal procedure:

1) After anesthesia with IP injection of urethane (40 mg/kg), the mice are injected with 0.2 ml of iodinated materials *via* jugular vein.

2) At defined time points (1 to 180 min), blood was sampled from the right carotid artery, allowed to clot at 23 °C, and then centrifuged at 5400g for 10 min. 50 μl of serum is collected from the supernatant.

3) Immediately after blood sampling, the whole brain is removed and kept on ice with cover untiled being weighed.

4) The serum samples, brain samples, and four aliquots of injection solutions representing injected dose (ID, CPM per mouse) are counted on r-counter simultaneously.

Data analysis:

1) The CPM in brain/serum samples is divided by ID and multiplied by 100 to get %ID, and then normalized by weight for brain samples (Am, %ID/g) or by volume for serum samples (Cpt, %ID/ml).

2) The exposure time ($\int Cpt \cdot dt / Cpt$) is the integral area under the curve (AUC) of serum concentration Cpt from time 0 to time t divided by Cpt at time t. The AUC is calculated using the trapezoidal rule as below.
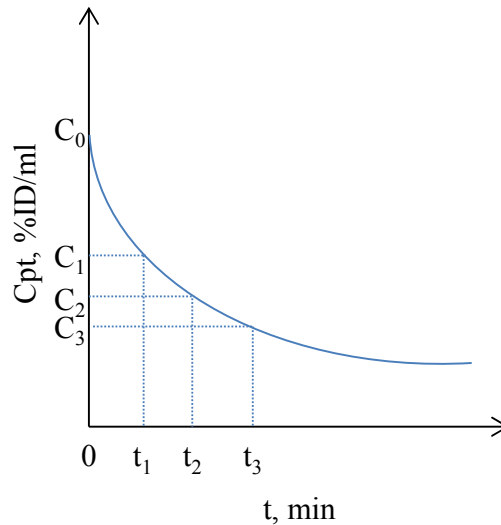
$$\int_0^{t_3} Cpt \cdot dt = \frac{(C1+C0) \cdot t1}{2} + \frac{(C2+C1) \cdot (t2-t1)}{2} + \frac{(C3+C2) \cdot (t3-t2)}{2}$$

3) The unidirectional brain influx rate (Ki, ml/g·min) and initial volume of brain distribution (Vi, ml/g) are determined by multiple-time regression analysis using the following equation [246]

$$Am/_{Cpt} = Ki \frac{\int Cpt \cdot dt}{Cpt} + Vi$$

where $Am/_{Cpt}$ is the brain/serum ratios (ml/g), and $\frac{\int Cpt \cdot dt}{Cpt}$ the exposure time, which is the integral area under the curve (AUC) of serum concentration Cpt from time 0 to time t divided by Cpt at time t.

2. Calculation of circulation half-life

Purpose:

This method is used to obtain the volume of distribution and circulation half-life from the linear portion of the regression of Ln(serum concentration) against time.

Animal procedure:

The animal procedure is same as the above section.

Data analysis:

Half-life: Ln(Cpt) is plotted against time (t, min) using Prism 5.0 software (GraphPad, San Diego, CA). The clearance rate (k, min^{-1}), half-life ($t_{1/2}$, min), and volume of distribution (V, ml) are calculated from the slope and y-intercept of the linear regression using the following equations [43]

$$Ln(Cpt) = k \times t + V$$

$$t_{1/2} = 0.693/k$$

3. Calculation of tissue accumulation

Purpose:

This method is used to calculate the tissue accumulation in non-perfused mice. The tissue accumulation can be directly measured in perfused mice. However, the efficiency of perfusion is varied among mice. Instead, the tissue accumulation can be calculated in non-perfused mice using co-injected iodinated BSA to adjust for the vascular space.

Animal procedure:

1) After anesthesia with IP injection of urethane (40 mg/kg), the mice are injected with 0.2 ml of ^{125}I-labelled test compound and ^{131}I-labelled BSA *via* jugular vein.

2) At defined time points, blood was sampled from the right carotid artery, allowed to clot at 23 °C, and then centrifuged at 5400g for 10 min. 50 µl of serum is collected from the supernatant.

3) Immediately after blood sampling, the tissue sample is removed and kept on ice with cover untiled being weighed.

4) The serum samples, tissue samples, and four aliquots of injection solutions representing injected dose (ID, CPM per mouse) are counted on r-counter simultaneously.

Data analysis:

1) For each of ^{125}I-labelled test compound and ^{131}I-labelled BSA, the CPM in serum and tissue samples is divided by ID and multiplied by 100 to get %ID, and then normalized by weight for tissue samples (%ID/g) and by volume for serum samples (%ID/ml).

2) Tissue/serum ratios (ml/g) for each of ^{125}I-labelled test compound and ^{131}I-labelled BSA are calculated as below.

$$\text{Tissue/serum ratio} = \frac{\%ID/g}{\%ID/ml}$$

3) Tissue accumulation of the ^{125}I-labelled test compound (%ID/g) is calculated as below.

Tissue accumulation (%ID/g) = (Tissue/serum ratio of test compound – Tissue/serum ratio of BSA) • Serum concentration of test compound

REFERENCES

[1] I. Brasnjevic, H.W. Steinbusch, C. Schmitz, P. Martinez-Martinez, I. European NanoBioPharmaceutics Research, Delivery of peptide and protein drugs over the blood-brain barrier, Prog Neurobiol, 87 (2009) 212-251.

[2] J. Rip, G.J. Schenk, A.G. de Boer, Differential receptor-mediated drug targeting to the diseased brain, Expert Opin Drug Deliv, 6 (2009) 227-237.

[3] W.A. Banks, Developing drugs that can cross the blood-brain barrier: applications to Alzheimer's disease, BMC Neuroscience, 9 (2008) S2-S2.

[4] P. Calias, W.A. Banks, D. Begley, M. Scarpa, P. Dickson, Intrathecal delivery of protein therapeutics to the brain: a critical reassessment, Pharmacol Ther, 144 (2014) 114-122.

[5] W.M. Pardridge, Drug transport across the blood-brain barrier, J Cereb Blood Flow Metab, 32 (2012) 1959-1972.

[6] P.G. Djupesland, J.C. Messina, R.A. Mahmoud, The nasal approach to delivering treatment for brain diseases: an anatomic, physiologic, and delivery technology overview, Ther Deliv, 5 (2014) 709-733.

[7] Y. Chen, L. Liu, Modern methods for delivery of drugs across the blood–brain barrier, Advanced Drug Delivery Reviews, 64 (2012) 640-665.

[8] A. Hartsock, W.J. Nelson, Adherens and tight junctions: Structure, function and connections to the actin cytoskeleton, Bba-Biomembranes, 1778 (2008) 660-669.

[9] A.C. Luissint, C. Artus, F. Glacial, K. Ganeshamoorthy, P.O. Couraud, Tight junctions at the blood brain barrier: physiological architecture and disease-associated dysregulation, Fluids Barriers CNS, 9 (2012) 23.

[10] J.M. Anderson, C.M. Van Itallie, Physiology and function of the tight junction, Cold Spring Harb Perspect Biol, 1 (2009) a002584.

[11] J.L. Mikitsh, A.M. Chacko, Pathways for small molecule delivery to the central nervous system across the blood-brain barrier, Perspect Medicin Chem, 6 (2014) 11-24.

[12] W.M. Pardridge, The Blood-Brain Barrier: Bottleneck in Brain Drug Development, NeuroRx, 2 (2005) 3-14.

[13] S. Mitragotri, P.A. Burke, R. Langer, Overcoming the challenges in administering biopharmaceuticals: formulation and delivery strategies, Nat Rev Drug Discov, 13 (2014) 655-672.

[14] X. Yi, D.S. Manickam, A. Brynskikh, A.V. Kabanov, Agile delivery of protein therapeutics to CNS, J Control Release, 190 (2014) 637-663.

[15] D.E. Bullard, M. Bourdon, D.D. Bigner, Comparison of various methods for delivering radiolabeled monoclonal antibody to normal rat brain, Journal of neurosurgery, 61 (1984) 901-911.

[16] E.A. Neuwelt, H.D. Specht, P.A. Barnett, S.A. Dahlborg, A. Miley, S.M. Larson, P. Brown, K.F. Eckerman, K.E. Hellstrom, I. Hellstrom, Increased delivery of tumor-specific monoclonal antibodies to brain after osmotic blood-brain barrier modification in patients with melanoma metastatic to the central nervous system, Neurosurgery, 20 (1987) 885-895.

[17] B.J. Shin, J.K. Burkhardt, H.A. Riina, J.A. Boockvar, Superselective intra-arterial cerebral infusion of novel agents after blood-brain disruption for the treatment of recurrent glioblastoma multiforme: a technical case series, Neurosurg Clin N Am, 23 (2012) 323-329, ix-x.

[18] B. Erdlenbruch, C. Schinkhof, W. Kugler, D.E. Heinemann, J. Herms, H. Eibl, M. Lakomek, Intracarotid administration of short-chain alkylglycerols for increased delivery of methotrexate to the rat brain, British journal of pharmacology, 139 (2003) 685-694.

[19] M. Kaya, L. Chang, A. Truong, M.W. Brightman, Chemical induction of fenestrae in vessels of the blood-brain barrier, Exp Neurol, 142 (1996) 6-13.

[20] J.F. Jordao, E. Thevenot, K. Markham-Coultes, T. Scarcelli, Y.Q. Weng, K. Xhima, M. O'Reilly, Y. Huang, J. McLaurin, K. Hynynen, I. Aubert, Amyloid-beta plaque reduction, endogenous antibody delivery and glial activation by brain-targeted, transcranial focused ultrasound, Exp Neurol, 248 (2013) 16-29.

[21] N. Sheikov, N. McDannold, N. Vykhodtseva, F. Jolesz, K. Hynynen, Cellular mechanisms of the blood-brain barrier opening induced by ultrasound in presence of microbubbles, Ultrasound Med Biol, 30 (2004) 979-989.

[22] J.F. Jordão, C.A. Ayala-Grosso, K. Markham, Y. Huang, R. Chopra, J. McLaurin, K. Hynynen, I. Aubert, Antibodies Targeted to the Brain with Image-Guided Focused Ultrasound Reduces Amyloid-β Plaque Load in the TgCRND8 Mouse Model of Alzheimer's Disease, PLoS ONE, 5 (2010) e10549.

[23] B. Rodriguez-Frutos, L. Otero-Ortega, J. Ramos-Cejudo, P. Martinez-Sanchez, I. Barahona-Sanz, T. Navarro-Hernanz, C. Gomez-de Frutos Mdel, E. Diez-Tejedor, M. Gutierrez-Fernandez, Enhanced brain-derived neurotrophic factor delivery by ultrasound and microbubbles promotes white matter repair after stroke, Biomaterials, 100 (2016) 41-52.

[24] G. Samiotaki, C. Acosta, S. Wang, E.E. Konofagou, Enhanced delivery and bioactivity of the neurturin neurotrophic factor through focused ultrasound-mediated blood--brain barrier opening in vivo, J Cereb Blood Flow Metab, 35 (2015) 611-622.

[25] W. Feng, S. Yu, L. Lin, L. Li, C. Youli, Z. Hairong, L. Xin, Y. Fei, Z. Chao, S. Chengyu, S. Jie, L. Shukun, C. Yun, Targeted Delivery of GDNF Through the Blood-Brain Barrier by Mri-Guided Focused Ultrasound, Ultrasound in Medicine & Biology, 39 (2013) S26.

[26] S.K. Wu, M.T. Yang, K.H. Kang, H.C. Liou, D.H. Lu, W.M. Fu, W.L. Lin, Targeted delivery of erythropoietin by transcranial focused ultrasound for neuroprotection against ischemia/reperfusion-induced neuronal injury: a long-term and short-term study, PLoS One, 9 (2014) e90107.

[27] P.Y. Chen, H.Y. Hsieh, C.Y. Huang, C.Y. Lin, K.C. Wei, H.L. Liu, Focused ultrasound-induced blood-brain barrier opening to enhance interleukin-12 delivery for brain tumor immunotherapy: a preclinical feasibility study, J Transl Med, 13 (2015) 93.

[28] M. Kinoshita, N. McDannold, F.A. Jolesz, K. Hynynen, Noninvasive localized delivery of Herceptin to the mouse brain by MRI-guided focused ultrasound-induced blood-brain barrier disruption, Proc Natl Acad Sci U S A, 103 (2006) 11719-11723.

[29] M. Kinoshita, N. McDannold, F.A. Jolesz, K. Hynynen, Targeted delivery of antibodies through the blood–brain barrier by MRI-guided focused ultrasound, Biochemical and Biophysical Research Communications, 340 (2006) 1085-1090.

[30] E.J. Park, Y.Z. Zhang, N. Vykhodtseva, N. McDannold, Ultrasound-mediated blood-brain/blood-tumor barrier disruption improves outcomes with trastuzumab in a breast cancer brain metastasis model, J Control Release, 163 (2012) 277-284.

[31] N. McDannold, C.D. Arvanitis, N. Vykhodtseva, M.S. Livingstone, Temporary disruption of the blood-brain barrier by use of ultrasound and microbubbles: safety and efficacy evaluation in rhesus macaques, Cancer Res, 72 (2012) 3652-3663.

[32] W. Yang, R.F. Barth, R. Leveille, D.M. Adams, M. Ciesielski, R.A. Fenstermaker, J. Capala, Evaluation of systemically administered radiolabeled epidermal growth factor as a brain tumor targeting agent, J Neurooncol, 55 (2001) 19-28.

[33] U. Bickel, T. Yoshikawa, W.M. Pardridge, Delivery of peptides and proteins through the blood-brain barrier, Adv Drug Deliv Rev, 46 (2001) 247-279.

[34] R.E. Kontermann, Strategies for extended serum half-life of protein therapeutics, Curr Opin Biotechnol, 22 (2011) 868-876.

[35] W.R. Strohl, Fusion Proteins for Half-Life Extension of Biologics as a Strategy to Make Biobetters, BioDrugs, 29 (2015) 215-239.

[36] V.N. Podust, S. Balan, B.C. Sim, M.P. Coyle, U. Ernst, R.T. Peters, V. Schellenberger, Extension of in vivo half-life of biologically active molecules by XTEN protein polymers, J Control Release, 240 (2016) 52-66.

[37] S.B. van Witteloostuijn, S.L. Pedersen, K.J. Jensen, Half-Life Extension of Biopharmaceuticals using Chemical Methods: Alternatives to PEGylation, ChemMedChem, 11 (2016) 2474-2495.

[38] P.L. Turecek, M.J. Bossard, F. Schoetens, I.A. Ivens, PEGylation of Biopharmaceuticals: A Review of Chemistry and Nonclinical Safety Information of Approved Drugs, J Pharm Sci, 105 (2016) 460-475.

[39] F.M. Veronese, P. Caliceti, O. Schiavon, Branched and Linear Poly(Ethylene Glycol): Influence of the Polymer Structure on Enzymological, Pharmacokinetic, and Immunological Properties of Protein Conjugates, Journal of Bioactive and Compatible Polymers, 12 (1997) 196-207.

[40] A.H. Sehon, Suppression of antibody responses by conjugates of antigens and monomethoxypoly(ethylene glycol), Advanced Drug Delivery Reviews, 6 (1991) 203-217.

[41] L. Wu, J. Chen, Y. Wu, B. Zhang, X. Cai, Z. Zhang, Y. Wang, L. Si, H. Xu, Y. Zheng, C. Zhang, C. Liang, J. Li, L. Zhang, Q. Zhang, D. Zhou, Precise and combinatorial PEGylation

generates a low-immunogenic and stable form of human growth hormone, J Control Release, 249 (2017) 84-93.

[42] S. Jevsevar, M. Kunstelj, V.G. Porekar, PEGylation of therapeutic proteins, Biotechnol J, 5 (2010) 113-128.

[43] X. Yi, D. Yuan, S.A. Farr, W.A. Banks, C.D. Poon, A.V. Kabanov, Pluronic modified leptin with increased systemic circulation, brain uptake and efficacy for treatment of obesity, J Control Release, 191 (2014) 34-46.

[44] Y. Gong, J.C. Leroux, M.A. Gauthier, Releasable Conjugation of Polymers to Proteins, Bioconjug Chem, 26 (2015) 1172-1181.

[45] C. Reichert, G. Borchard, Noncovalent PEGylation, An Innovative Subchapter in the Field of Protein Modification, J Pharm Sci, 105 (2016) 386-390.

[46] E. Ambrosio, M. Barattin, S. Bersani, S. Shubber, S. Uddin, C.F. van der Walle, P. Caliceti, S. Salmaso, A novel combined strategy for the physical PEGylation of polypeptides, J Control Release, 226 (2016) 35-46.

[47] M.J. Webber, E.A. Appel, B. Vinciguerra, A.B. Cortinas, L.S. Thapa, S. Jhunjhunwala, L. Isaacs, R. Langer, D.G. Anderson, Supramolecular PEGylation of biopharmaceuticals, Proc Natl Acad Sci U S A, 113 (2016) 14189-14194.

[48] A. Mero, T. Ishino, I. Chaiken, F.M. Veronese, G. Pasut, Multivalent and flexible PEG-nitrilotriacetic acid derivatives for non-covalent protein pegylation, Pharm Res, 28 (2011) 2412-2421.

[49] P. Zhang, F. Sun, S. Liu, S. Jiang, Anti-PEG antibodies in the clinic: Current issues and beyond PEGylation, J Control Release, 244 (2016) 184-193.

[50] I.A. Ivens, W. Achanzar, A. Baumann, A. Brandli-Baiocco, J. Cavagnaro, M. Dempster, B.O. Depelchin, A.R. Rovira, L. Dill-Morton, J.H. Lane, B.M. Reipert, T. Salcedo, B. Schweighardt, L.S. Tsuruda, P.L. Turecek, J. Sims, PEGylated Biopharmaceuticals: Current Experience and Considerations for Nonclinical Development, Toxicol Pathol, 43 (2015) 959-983.

[51] A.J. Keefe, S. Jiang, Poly(zwitterionic)protein conjugates offer increased stability without sacrificing binding affinity or bioactivity, Nat Chem, 4 (2011) 59-63.

[52] A. Mero, M. Pasqualin, M. Campisi, D. Renier, G. Pasut, Conjugation of hyaluronan to proteins, Carbohydr Polym, 92 (2013) 2163-2170.

[53] R. Luxenhofer, Y. Han, A. Schulz, J. Tong, Z. He, A.V. Kabanov, R. Jordan, Poly(2-oxazoline)s as polymer therapeutics, Macromol Rapid Commun, 33 (2012) 1613-1631.

[54] E. Elinav, L. Niv-Spector, M. Katz, T.O. Price, M. Ali, M. Yacobovitz, G. Solomon, S. Reicher, J.L. Lynch, Z. Halpern, W.A. Banks, A. Gertler, Pegylated leptin antagonist is a potent orexigenic agent: preparation and mechanism of activity, Endocrinology, 150 (2009) 3083-3091.

[55] K.M. Lo, J. Zhang, Y. Sun, B. Morelli, Y. Lan, S. Lauder, B. Brunkhorst, G. Webster, S. Hallakou-Bozec, L. Doare, S.D. Gillies, Engineering a pharmacologically superior form of leptin for the treatment of obesity, Protein Eng Des Sel, 18 (2005) 1-10.

[56] V. Morath, F. Bolze, M. Schlapschy, S. Schneider, F. Sedlmayer, K. Seyfarth, M. Klingenspor, A. Skerra, PASylation of Murine Leptin Leads to Extended Plasma Half-Life and Enhanced in Vivo Efficacy, Mol Pharm, 12 (2015) 1431-1442.

[57] M. Schlapschy, U. Binder, C. Borger, I. Theobald, K. Wachinger, S. Kisling, D. Haller, A. Skerra, PASylation: a biological alternative to PEGylation for extending the plasma half-life of pharmaceutically active proteins, Protein Eng Des Sel, 26 (2013) 489-501.

[58] W. Hassouneh, S.R. MacEwan, A. Chilkoti, Fusions of elastin-like polypeptides to pharmaceutical proteins, Methods Enzymol, 502 (2012) 215-237.

[59] R.G. Thorne, W.H. Frey, 2nd, Delivery of neurotrophic factors to the central nervous system: pharmacokinetic considerations, Clin Pharmacokinet, 40 (2001) 907-946.

[60] W.A. Banks, A.J. Kastin, Peptides and the blood-brain barrier: lipophilicity as a predictor of permeability, Brain research bulletin, 15 (1985) 287-292.

[61] E.V. Batrakova, S.V. Vinogradov, S.M. Robinson, M.L. Niehoff, W.A. Banks, A.V. Kabanov, Polypeptide point modifications with fatty acid and amphiphilic block copolymers for enhanced brain delivery, Bioconjug Chem, 16 (2005) 793-802.

[62] X. Yi, A.V. Kabanov, Brain delivery of proteins via their fatty acid and block copolymer modifications, J Drug Target, 21 (2013) 940-955.

[63] F. Herve, N. Ghinea, J.M. Scherrmann, CNS delivery via adsorptive transcytosis, AAPS J, 10 (2008) 455-472.

[64] W.M. Pardridge, D. Triguero, J. Buciak, J. Yang, Evaluation of cationized rat albumin as a potential blood-brain barrier drug transport vector, J Pharmacol Exp Ther, 255 (1990) 893-899.

[65] D. Triguero, J.B. Buciak, J. Yang, W.M. Pardridge, Blood-brain barrier transport of cationized immunoglobulin G: enhanced delivery compared to native protein, Proc Natl Acad Sci U S A, 86 (1989) 4761-4765.

[66] Z. Nagy, H. Peters, I. Huttner, Charge-related alterations of the cerebral endothelium, Lab Invest, 49 (1983) 662-671.

[67] J.E. Hardebo, J. Kahrstrom, Endothelial negative surface charge areas and blood-brain barrier function, Acta Physiol Scand, 125 (1985) 495-499.

[68] M. Kristensen, D. Birch, H. Morck Nielsen, Applications and Challenges for Use of Cell-Penetrating Peptides as Delivery Vectors for Peptide and Protein Cargos, Int J Mol Sci, 17 (2016).

[69] N.Q. Shi, X.R. Qi, B. Xiang, Y. Zhang, A survey on "Trojan Horse" peptides: opportunities, issues and controlled entry to "Troy", J Control Release, 194 (2014) 53-70.

[70] L.L. Zou, J.L. Ma, T. Wang, T.B. Yang, C.B. Liu, Cell-penetrating Peptide-mediated therapeutic molecule delivery into the central nervous system, Curr Neuropharmacol, 11 (2013) 197-208.

[71] S.R. Schwarze, A. Ho, A. Vocero-Akbani, S.F. Dowdy, In vivo protein transduction: delivery of a biologically active protein into the mouse, Science, 285 (1999) 1569-1572.

[72] D.J. Mitchell, D.T. Kim, L. Steinman, C.G. Fathman, J.B. Rothbard, Polyarginine enters cells more efficiently than other polycationic homopolymers, J Pept Res, 56 (2000) 318-325.

[73] G. Tunnemann, G. Ter-Avetisyan, R.M. Martin, M. Stockl, A. Herrmann, M.C. Cardoso, Live-cell analysis of cell penetration ability and toxicity of oligo-arginines, J Pept Sci, 14 (2008) 469-476.

[74] S. Reissmann, Cell penetration: scope and limitations by the application of cell-penetrating peptides, J Pept Sci, 20 (2014) 760-784.

[75] Y. Gotanda, F.Y. Wei, H. Harada, K. Ohta, K. Nakamura, K. Tomizawa, K. Ushijima, Efficient transduction of 11 poly-arginine peptide in an ischemic lesion of mouse brain, J Stroke Cerebrovasc Dis, 23 (2014) 2023-2030.

[76] S. Tanaka, K. Kitagawa, S. Sugiura, E. Matsuoka-Omura, T. Sasaki, Y. Yagita, M. Hori, Infiltrating macrophages as in vivo targets for intravenous gene delivery in cerebral infarction, Stroke, 35 (2004) 1968-1973.

[77] Y. Jiang, P. Arounleut, S. Rheiner, Y. Bae, A.V. Kabanov, C. Milligan, D.S. Manickam, SOD1 nanozyme with reduced toxicity and MPS accumulation, J Control Release, 231 (2016) 38-49.

[78] J.M. Lajoie, E.V. Shusta, Targeting receptor-mediated transport for delivery of biologics across the blood-brain barrier, Annu Rev Pharmacol Toxicol, 55 (2015) 613-631.

[79] Y.Y. Wang, P.C. Lui, J.Y. Li, Receptor-mediated therapeutic transport across the blood-brain barrier, Immunotherapy, 1 (2009) 983-993.

[80] A.R. Jones, E.V. Shusta, Blood-brain barrier transport of therapeutics via receptor-mediation, Pharm Res, 24 (2007) 1759-1771.

[81] Y.J. Yu, Y. Zhang, M. Kenrick, K. Hoyte, W. Luk, Y. Lu, J. Atwal, J.M. Elliott, S. Prabhu, R.J. Watts, M.S. Dennis, Boosting brain uptake of a therapeutic antibody by reducing its affinity for a transcytosis target, Sci Transl Med, 3 (2011) 84ra44.

[82] N. Bien-Ly, Y.J. Yu, D. Bumbaca, J. Elstrott, C.A. Boswell, Y. Zhang, W. Luk, Y. Lu, M.S. Dennis, R.M. Weimer, I. Chung, R.J. Watts, Transferrin receptor (TfR) trafficking determines brain uptake of TfR antibody affinity variants, J Exp Med, 211 (2014) 233-244.

[83] J.A. Couch, Y.J. Yu, Y. Zhang, J.M. Tarrant, R.N. Fuji, W.J. Meilandt, H. Solanoy, R.K. Tong, K. Hoyte, W. Luk, Y. Lu, K. Gadkar, S. Prabhu, B.A. Ordonia, Q. Nguyen, Y. Lin, Z. Lin, M. Balazs, K. Scearce-Levie, J.A. Ernst, M.S. Dennis, R.J. Watts, Addressing safety liabilities of TfR bispecific antibodies that cross the blood-brain barrier, Sci Transl Med, 5 (2013) 183ra157, 181-112.

[84] J. Niewoehner, B. Bohrmann, L. Collin, E. Urich, H. Sade, P. Maier, P. Rueger, J.O. Stracke, W. Lau, A.C. Tissot, H. Loetscher, A. Ghosh, P.O. Freskgard, Increased brain penetration and potency of a therapeutic antibody using a monovalent molecular shuttle, Neuron, 81 (2014) 49-60.

[85] H. Sade, C. Baumgartner, A. Hugenmatter, E. Moessner, P.O. Freskgard, J. Niewoehner, A human blood-brain barrier transcytosis assay reveals antibody transcytosis influenced by pH-dependent receptor binding, PLoS One, 9 (2014) e96340.

[86] Q.H. Zhou, J.Z. Lu, E.K. Hui, R.J. Boado, W.M. Pardridge, Delivery of a peptide radiopharmaceutical to brain with an IgG-avidin fusion protein, Bioconjug Chem, 22 (2011) 1611-1618.

[87] D.T. Wiley, P. Webster, A. Gale, M.E. Davis, Transcytosis and brain uptake of transferrin-containing nanoparticles by tuning avidity to transferrin receptor, Proc Natl Acad Sci U S A, 110 (2013) 8662-8667.

[88] J. Paterson, C.I. Webster, Exploiting transferrin receptor for delivering drugs across the blood-brain barrier, Drug Discov Today Technol, 20 (2016) 49-52.

[89] M. Lo, H.S. Kim, R.K. Tong, T.W. Bainbridge, J.M. Vernes, Y. Zhang, Y.L. Lin, S. Chung, M.S. Dennis, Y.J. Zuchero, R.J. Watts, J.A. Couch, Y.G. Meng, J.K. Atwal, R.J. Brezski, C. Spiess, J.A. Ernst, Effector attenuating substitutions that maintain antibody stability and reduce toxicity in mice, J Biol Chem, (2017).

[90] F. Ueda, K.B. Raja, R.J. Simpson, I.S. Trowbridge, M.W. Bradbury, Rate of 59Fe uptake into brain and cerebrospinal fluid and the influence thereon of antibodies against the transferrin receptor, Journal of neurochemistry, 60 (1993) 106-113.

[91] F. Zhang, Y.A. Lin, S. Kannan, R.M. Kannan, Targeting specific cells in the brain with nanomedicines for CNS therapies, J Control Release, (2015).

[92] E.V. Batrakova, A.V. Kabanov, Cell-mediated drug delivery to the brain, Journal of Drug Delivery Science and Technology, 23 (2013) 419-433.

[93] H. Lassmann, M. Schmied, K. Vass, W.F. Hickey, Bone marrow derived elements and resident microglia in brain inflammation, Glia, 7 (1993) 19-24.

[94] G.J. Schenk, H.E. de Vries, Altered blood-brain barrier transport in neuro-inflammatory disorders, Drug Discov Today Technol, 20 (2016) 5-11.

[95] M. Prinz, A. Mildner, Microglia in the CNS: immigrants from another world, Glia, 59 (2011) 177-187.

[96] W.A. Muller, Getting leukocytes to the site of inflammation, Vet Pathol, 50 (2013) 7-22.

[97] N.A. Pawlowski, G. Kaplan, E. Abraham, Z.A. Cohn, The selective binding and transmigration of monocytes through the junctional complexes of human endothelium, J Exp Med, 168 (1988) 1865-1882.

[98] A.S. Lossinsky, R.R. Shivers, Structural pathways for macromolecular and cellular transport across the blood-brain barrier during inflammatory conditions. Review, Histol Histopathol, 19 (2004) 535-564.

[99] C.V. Carman, Mechanisms for transcellular diapedesis: probing and pathfinding by 'invadosome-like protrusions', J Cell Sci, 122 (2009) 3025-3035.

[100] M.L. Selenica, P. Reid, G. Pena, J. Alvarez, J.B. Hunt, Jr., K.R. Nash, D. Morgan, M.N. Gordon, D.C. Lee, Adeno associated viral-mediated intraosseous labeling of bone marrow derived cells for CNS tracking, J Immunol Methods, 432 (2016) 51-56.

[101] R. Tanaka, M. Komine-Kobayashi, H. Mochizuki, M. Yamada, T. Furuya, M. Migita, T. Shimada, Y. Mizuno, T. Urabe, Migration of enhanced green fluorescent protein expressing bone marrow-derived microglia/macrophage into the mouse brain following permanent focal ischemia, Neuroscience, 117 (2003) 531-539.

[102] M.J. Haney, Y. Zhao, E.B. Harrison, V. Mahajan, S. Ahmed, Z. He, P. Suresh, S.D. Hingtgen, N.L. Klyachko, R.L. Mosley, H.E. Gendelman, A.V. Kabanov, E.V. Batrakova, Specific transfection of inflamed brain by macrophages: a new therapeutic strategy for neurodegenerative diseases, PLoS One, 8 (2013) e61852.

[103] H. Dou, C.B. Grotepas, J.M. McMillan, C.J. Destache, M. Chaubal, J. Werling, J. Kipp, B. Rabinow, H.E. Gendelman, Macrophage delivery of nanoformulated antiretroviral drug to the brain in a murine model of neuroAIDS, J Immunol, 183 (2009) 661-669.

[104] E.V. Batrakova, S. Li, A.D. Reynolds, R.L. Mosley, T.K. Bronich, A.V. Kabanov, H.E. Gendelman, A macrophage-nanozyme delivery system for Parkinson's disease, Bioconjug Chem, 18 (2007) 1498-1506.

[105] M.J. Haney, P. Suresh, Y. Zhao, G.D. Kanmogne, I. Kadiu, M. Sokolsky-Papkov, N.L. Klyachko, R.L. Mosley, A.V. Kabanov, H.E. Gendelman, E.V. Batrakova, Blood-borne macrophage-neural cell interactions hitchhike on endosome networks for cell-based nanozyme brain delivery, Nanomedicine (Lond), 7 (2012) 815-833.

[106] A.M. Brynskikh, Y. Zhao, R.L. Mosley, S. Li, M.D. Boska, N.L. Klyachko, A.V. Kabanov, H.E. Gendelman, E.V. Batrakova, Macrophage delivery of therapeutic nanozymes in a murine model of Parkinson's disease, Nanomedicine (Lond), 5 (2010) 379-396.

[107] N.L. Klyachko, M.J. Haney, Y. Zhao, D.S. Manickam, V. Mahajan, P. Suresh, S.D. Hingtgen, R.L. Mosley, H.E. Gendelman, A.V. Kabanov, E.V. Batrakova, Macrophages offer a paradigm switch for CNS delivery of therapeutic proteins, Nanomedicine (Lond), 9 (2014) 1403-1422.

[108] Y. Zhao, M.J. Haney, R. Gupta, J.P. Bohnsack, Z. He, A.V. Kabanov, E.V. Batrakova, GDNF-transfected macrophages produce potent neuroprotective effects in Parkinson's disease mouse model, PLoS One, 9 (2014) e106867.

[109] M.J. Haney, Y. Zhao, S. Li, S.M. Higginbotham, S.L. Booth, H.Y. Han, J.A. Vetro, R.L. Mosley, A.V. Kabanov, H.E. Gendelman, E.V. Batrakova, Cell-mediated transfer of catalase nanoparticles from macrophages to brain endothelial, glial and neuronal cells, Nanomedicine (Lond), 6 (2011) 1215-1230.

[110] K.C. Biju, Q. Zhou, G. Li, S.Z. Imam, J.L. Roberts, W.W. Morgan, R.A. Clark, S. Li, Macrophage-mediated GDNF Delivery Protects Against Dopaminergic Neurodegeneration: A Therapeutic Strategy for Parkinson's Disease, Mol Ther, 18 (2010) 1536-1544.

[111] N. Doshi, A.J. Swiston, J.B. Gilbert, M.L. Alcaraz, R.E. Cohen, M.F. Rubner, S. Mitragotri, Cell-Based Drug Delivery Devices Using Phagocytosis-Resistant Backpacks, Advanced Materials, 23 (2011) H105-H109.

[112] A.C. Anselmo, J.B. Gilbert, S. Kumar, V. Gupta, R.E. Cohen, M.F. Rubner, S. Mitragotri, Monocyte-mediated delivery of polymeric backpacks to inflamed tissues: a generalized strategy to deliver drugs to treat inflammation, J Control Release, 199 (2015) 29-36.

[113] E.V. Batrakova, H.E. Gendelman, A.V. Kabanov, Cell-mediated drug delivery, Expert Opin Drug Deliv, 8 (2011) 415-433.

[114] E. Blanco, H. Shen, M. Ferrari, Principles of nanoparticle design for overcoming biological barriers to drug delivery, Nat Biotechnol, 33 (2015) 941-951.

[115] K. Hirota, H. Terada, Endocytosis of Particle Formulations by Macrophages and Its Application to Clinical Treatment, 2012.

[116] Y. Su, Z. Xie, G.B. Kim, C. Dong, J. Yang, Design strategies and applications of circulating cell-mediated drug delivery systems, ACS Biomater Sci Eng, 1 (2015) 201-217.

[117] K.A. Beningo, Y.-l. Wang, Fc-receptor-mediated phagocytosis is regulated by mechanical properties of the target, Journal of Cell Science, 115 (2002) 849-856.

[118] Y. Zhao, M.J. Haney, N.L. Klyachko, S. Li, S.L. Booth, S.M. Higginbotham, J. Jones, M.C. Zimmerman, R.L. Mosley, A.V. Kabanov, H.E. Gendelman, E.V. Batrakova, Polyelectrolyte complex optimization for macrophage delivery of redox enzyme nanoparticles, Nanomedicine (Lond), 6 (2011) 25-42.

[119] H.I. Tong, W. Kang, P.M. Davy, Y. Shi, S. Sun, R.C. Allsopp, Y. Lu, Monocyte Trafficking, Engraftment, and Delivery of Nanoparticles and an Exogenous Gene into the Acutely Inflamed Brain Tissue - Evaluations on Monocyte-Based Delivery System for the Central Nervous System, PLoS One, 11 (2016) e0154022.

[120] H.I. Tong, W. Kang, Y. Shi, G. Zhou, Y. Lu, Physiological function and inflamed-brain migration of mouse monocyte-derived macrophages following cellular uptake of superparamagnetic iron oxide nanoparticles-Implication of macrophage-based drug delivery into the central nervous system, Int J Pharm, 505 (2016) 271-282.

[121] J. Wu, S. Yang, H. Luo, L. Zeng, L. Ye, Y. Lu, Quantitative evaluation of monocyte transmigration into the brain following chemical opening of the blood-brain barrier in mice, Brain Res, 1098 (2006) 79-85.

[122] S.C. Jang, O.Y. Kim, C.M. Yoon, D.S. Choi, T.Y. Roh, J. Park, J. Nilsson, J. Lotvall, Y.K. Kim, Y.S. Gho, Bioinspired exosome-mimetic nanovesicles for targeted delivery of chemotherapeutics to malignant tumors, ACS nano, 7 (2013) 7698-7710.

[123] L. Urbanelli, A. Magini, S. Buratta, A. Brozzi, K. Sagini, A. Polchi, B. Tancini, C. Emiliani, Signaling Pathways in Exosomes Biogenesis, Secretion and Fate, Genes, 4 (2013) 152-170.

[124] S. Fais, M. Logozzi, L. Lugini, C. Federici, T. Azzarito, N. Zarovni, A. Chiesi, Exosomes: the ideal nanovectors for biodelivery, Biological chemistry, 394 (2013) 1-15.

[125] E.G. Trams, C.J. Lauter, N. Salem, Jr., U. Heine, Exfoliation of membrane ecto-enzymes in the form of micro-vesicles, Biochim Biophys Acta, 645 (1981) 63-70.

[126] R.M. Johnstone, M. Adam, J.R. Hammond, L. Orr, C. Turbide, Vesicle formation during reticulocyte maturation. Association of plasma membrane activities with released vesicles (exosomes), J Biol Chem, 262 (1987) 9412-9420.

[127] H. Valadi, K. Ekstrom, A. Bossios, M. Sjostrand, J.J. Lee, J.O. Lotvall, Exosome-mediated transfer of mRNAs and microRNAs is a novel mechanism of genetic exchange between cells, Nat Cell Biol, 9 (2007) 654-659.

[128] J.L. Hood, R.S. San, S.A. Wickline, Exosomes released by melanoma cells prepare sentinel lymph nodes for tumor metastasis, Cancer Res, 71 (2011) 3792-3801.

[129] G.C. Sampey, S.S. Meyering, M. Asad Zadeh, M. Saifuddin, R.M. Hakami, F. Kashanchi, Exosomes and their role in CNS viral infections, J Neurovirol, 20 (2014) 199-208.

[130] D.M. Sun, X.Y. Zhuang, S.Q. Zhang, Z.B. Deng, W. Grizzle, D. Miller, H.G. Zhang, Exosomes are endogenous nanoparticles that can deliver biological information between cells, Advanced Drug Delivery Reviews, 65 (2013) 342-347.

[131] D. Ha, N. Yang, V. Nadithe, Exosomes as therapeutic drug carriers and delivery vehicles across biological membranes: current perspectives and future challenges, Acta Pharmaceutica Sinica B, 6 (2016) 287-296.

[132] M. Basso, V. Bonetto, Extracellular Vesicles and a Novel Form of Communication in the Brain, Front Neurosci-Switz, 10 (2016).

[133] D.M. Pegtel, L. Peferoen, S. Amor, Extracellular vesicles as modulators of cell-to-cell communication in the healthy and diseased brain, Philos T R Soc B, 369 (2014).

[134] T.J. Smyth, J.S. Redzic, M.W. Graner, T.J. Anchordoquy, Examination of the specificity of tumor cell derived exosomes with tumor cells in vitro, Biochim Biophys Acta, 1838 (2014) 2954-2965.

[135] T. Smyth, M. Kullberg, N. Malik, P. Smith-Jones, M.W. Graner, T.J. Anchordoquy, Biodistribution and delivery efficiency of unmodified tumor-derived exosomes, J Control Release, 199 (2015) 145-155.

[136] L. Alvarez-Erviti, Y. Seow, H. Yin, C. Betts, S. Lakhal, M.J. Wood, Delivery of siRNA to the mouse brain by systemic injection of targeted exosomes, Nat Biotechnol, 29 (2011) 341-345.

[137] X. Zhuang, X. Xiang, W. Grizzle, D. Sun, S. Zhang, R.C. Axtell, S. Ju, J. Mu, L. Zhang, L. Steinman, D. Miller, H.G. Zhang, Treatment of brain inflammatory diseases by delivering exosome encapsulated anti-inflammatory drugs from the nasal region to the brain, Mol Ther, 19 (2011) 1769-1779.

[138] M.J. Haney, N.L. Klyachko, Y. Zhao, R. Gupta, E.G. Plotnikova, Z. He, T. Patel, A. Piroyan, M. Sokolsky, A.V. Kabanov, E.V. Batrakova, Exosomes as drug delivery vehicles for Parkinson's disease therapy, J Control Release, 207 (2015) 18-30.

[139] T.Z. Yang, P. Martin, B. Fogarty, A. Brown, K. Schurman, R. Phipps, V.P. Yin, P. Lockman, S.H. Bai, Exosome Delivered Anticancer Drugs Across the Blood-Brain Barrier for Brain Cancer Therapy in Danio Rerio, Pharm Res-Dordr, 32 (2015) 2003-2014.

[140] C.A. MacRae, R.T. Peterson, Zebrafish as tools for drug discovery, Nat Rev Drug Discov, 14 (2015) 721-731.

[141] W. Hwang do, H. Choi, S.C. Jang, M.Y. Yoo, J.Y. Park, N.E. Choi, H.J. Oh, S. Ha, Y.S. Lee, J.M. Jeong, Y.S. Gho, D.S. Lee, Noninvasive imaging of radiolabeled exosome-mimetic nanovesicle using (99m)Tc-HMPAO, Sci Rep, 5 (2015) 15636.

[142] O.P. Wiklander, J.Z. Nordin, A. O'Loughlin, Y. Gustafsson, G. Corso, I. Mager, P. Vader, Y. Lee, H. Sork, Y. Seow, N. Heldring, L. Alvarez-Erviti, C.I. Smith, K. Le Blanc, P. Macchiarini, P. Jungebluth, M.J. Wood, S.E. Andaloussi, Extracellular vesicle in vivo biodistribution is determined by cell source, route of administration and targeting, J Extracell Vesicles, 4 (2015) 26316.

[143] Y. Takahashi, M. Nishikawa, H. Shinotsuka, Y. Matsui, S. Ohara, T. Imai, Y. Takakura, Visualization and in vivo tracking of the exosomes of murine melanoma B16-BL6 cells in mice after intravenous injection, J Biotechnol, 165 (2013) 77-84.

[144] T. Imai, Y. Takahashi, M. Nishikawa, K. Kato, M. Morishita, T. Yamashita, A. Matsumoto, C. Charoenviriyakul, Y. Takakura, Macrophage-dependent clearance of systemically administered B16BL6-derived exosomes from the blood circulation in mice, J Extracell Vesicles, 4 (2015) 26238.

[145] M. Morishita, Y. Takahashi, M. Nishikawa, K. Sano, K. Kato, T. Yamashita, T. Imai, H. Saji, Y. Takakura, Quantitative analysis of tissue distribution of the B16BL6-derived exosomes using a streptavidin-lactadherin fusion protein and iodine-125-labeled biotin derivative after intravenous injection in mice, J Pharm Sci, 104 (2015) 705-713.

[146] S.C. Saunderson, A.C. Dunn, P.R. Crocker, A.D. McLellan, CD169 mediates the capture of exosomes in spleen and lymph node, Blood, 123 (2014) 208-216.

[147] F. Aoudjit, E.F. Potworowski, T.A. Springer, Y. St-Pierre, Protection from lymphoma cell metastasis in ICAM-1 mutant mice: a posthoming event, J Immunol, 161 (1998) 2333-2338.

[148] G.R. Vasta, H. Ahmed, Animal lectins : a functional view, CRC Press, Boca Raton, 2009.

[149] D.J. Begley, Brain superhighways, Sci Transl Med, 4 (2012) 147fs129.

[150] D.J. Wolak, R.G. Thorne, Diffusion of macromolecules in the brain: implications for drug delivery, Mol Pharm, 10 (2013) 1492-1504.

[151] W.A. Hall, E. Rustamzadeh, A.L. Asher, Convection-enhanced delivery in clinical trials, Neurosurg Focus, 14 (2003) e2.

[152] N.G. Rainov, K. Gorbatyuk, V. Heidecke, Clinical trials with intracerebral convection-enhanced delivery of targeted toxins in malignant glioma, Rev Recent Clin Trials, 3 (2008) 2-9.

[153] E.A. Neuwelt, P.A. Barnett, C.I. McCormick, E.P. Frenkel, J.D. Minna, Osmotic blood-brain barrier modification: monoclonal antibody, albumin, and methotrexate delivery to cerebrospinal fluid and brain, Neurosurgery, 17 (1985) 419-423.

[154] A. Hdeib, A.E. Sloan, Convection-enhanced delivery of 131I-chTNT-1/B mAB for treatment of high-grade adult gliomas, Expert Opin Biol Ther, 11 (2011) 799-806.

[155] C. Buonerba, G. Di Lorenzo, A. Marinelli, P. Federico, G. Palmieri, M. Imbimbo, P. Conti, G. Peluso, S. De Placido, J.H. Sampson, A comprehensive outlook on intracerebral therapy of malignant gliomas, Crit Rev Oncol Hematol, 80 (2011) 54-68.

[156] A.I. Mehta, B.D. Choi, R. Raghavan, M. Brady, A.H. Friedman, D.D. Bigner, I. Pastan, J.H. Sampson, Imaging of convection enhanced delivery of toxins in humans, Toxins (Basel), 3 (2011) 201-206.

[157] S. Kunwar, M.D. Prados, S.M. Chang, M.S. Berger, F.F. Lang, J.M. Piepmeier, J.H. Sampson, Z. Ram, P.H. Gutin, R.D. Gibbons, K.D. Aldape, D.J. Croteau, J.W. Sherman, R.K. Puri, G. Cintredekin Besudotox Intraparenchymal Study, Direct intracerebral delivery of cintredekin besudotox (IL13-PE38QQR) in recurrent malignant glioma: a report by the Cintredekin Besudotox Intraparenchymal Study Group, J Clin Oncol, 25 (2007) 837-844.

[158] T.J. McCarthy, W.A. Banks, C.L. Farrell, S. Adamu, C.P. Derdeyn, A.Z. Snyder, R. Laforest, D.C. Litzinger, D. Martin, C.P. LeBel, M.J. Welch, Positron emission tomography shows that intrathecal leptin reaches the hypothalamus in baboons, J Pharmacol Exp Ther, 301 (2002) 878-883.

[159] C. LeBel, A. Bourdeau, D. Lau, P. Hunt, Biologic response to peripheral and central administration of recombinant human leptin in dogs, Obes Res, 7 (1999) 577-585.

[160] T.N. Nagaraja, P. Patel, M. Gorski, P.D. Gorevic, C.S. Patlak, J.D. Fenstermacher, In normal rat, intraventricularly administered insulin-like growth factor-1 is rapidly cleared from CSF with limited distribution into brain, Cerebrospinal Fluid Res, 2 (2005) 5.

[161] J.G. Nutt, K.J. Burchiel, C.L. Comella, J. Jankovic, A.E. Lang, E.R. Laws, Jr., A.M. Lozano, R.D. Penn, R.K. Simpson, Jr., M. Stacy, G.F. Wooten, I.G.S.G.I.i.G.c.l.-d.n. factor, Randomized, double-blind trial of glial cell line-derived neurotrophic factor (GDNF) in PD, Neurology, 60 (2003) 69-73.

[162] C.D. Chapman, W.H. Frey, 2nd, S. Craft, L. Danielyan, M. Hallschmid, H.B. Schioth, C. Benedict, Intranasal treatment of central nervous system dysfunction in humans, Pharm Res, 30 (2013) 2475-2484.

[163] M.J. Ruigrok, E.C. de Lange, Emerging Insights for Translational Pharmacokinetic and Pharmacokinetic-Pharmacodynamic Studies: Towards Prediction of Nose-to-Brain Transport in Humans, AAPS J, 17 (2015) 493-505.

[164] R.G. Thorne, G.J. Pronk, V. Padmanabhan, W.H. Frey, 2nd, Delivery of insulin-like growth factor-I to the rat brain and spinal cord along olfactory and trigeminal pathways following intranasal administration, Neuroscience, 127 (2004) 481-496.

[165] R.G. Thorne, C.R. Emory, T.A. Ala, W.H. Frey, 2nd, Quantitative analysis of the olfactory pathway for drug delivery to the brain, Brain Res, 692 (1995) 278-282.

[166] J.J. Lochhead, R.G. Thorne, Intranasal delivery of biologics to the central nervous system, Adv Drug Deliv Rev, 64 (2012) 614-628.

[167] J.H. Lee, E.H. Kam, J.M. Kim, S.Y. Kim, E.J. Kim, S.Y. Cheon, B.N. Koo, Intranasal Administration of Interleukin-1 Receptor Antagonist in a Transient Focal Cerebral Ischemia Rat Model, Biomol Ther (Seoul), (2016).

[168] R.D. Broadwell, B.J. Balin, Endocytic and exocytic pathways of the neuronal secretory process and trans-synaptic transfer of wheat germ agglutinin-horseradish peroxidase in vivo, J Comp Neurol, 242 (1985) 632-650.

[169] J.J. Lochhead, D.J. Wolak, M.E. Pizzo, R.G. Thorne, Rapid transport within cerebral perivascular spaces underlies widespread tracer distribution in the brain after intranasal administration, J Cereb Blood Flow Metab, 35 (2015) 371-381.

[170] C. Xiao, F.J. Davis, B.C. Chauhan, K.L. Viola, P.N. Lacor, P.T. Velasco, W.L. Klein, N.B. Chauhan, Brain transit and ameliorative effects of intranasally delivered anti-amyloid-beta oligomer antibody in 5XFAD mice, J Alzheimers Dis, 35 (2013) 777-788.

[171] R.A. Scranton, L. Fletcher, S. Sprague, D.F. Jimenez, M. Digicaylioglu, The rostral migratory stream plays a key role in intranasal delivery of drugs into the CNS, PLoS One, 6 (2011) e18711.

[172] S.A. Deadwyler, L. Porrino, J.M. Siegel, R.E. Hampson, Systemic and nasal delivery of orexin-A (Hypocretin-1) reduces the effects of sleep deprivation on cognitive performance in nonhuman primates, J Neurosci, 27 (2007) 14239-14247.

[173] J.P. Yang, H.J. Liu, S.M. Cheng, Z.L. Wang, X. Cheng, H.X. Yu, X.F. Liu, Direct transport of VEGF from the nasal cavity to brain, Neurosci Lett, 449 (2009) 108-111.

[174] T.M. Ross, P.M. Martinez, J.C. Renner, R.G. Thorne, L.R. Hanson, W.H. Frey, 2nd, Intranasal administration of interferon beta bypasses the blood-brain barrier to target the central

nervous system and cervical lymph nodes: a non-invasive treatment strategy for multiple sclerosis, J Neuroimmunol, 151 (2004) 66-77.

[175] B.L. Sun, M.Q. He, X.Y. Han, J.Y. Sun, M.F. Yang, H. Yuan, C.D. Fan, S. Zhang, L.L. Mao, D.W. Li, Z.Y. Zhang, C.B. Zheng, X.Y. Yang, Y.V. Li, R.A. Stetler, J. Chen, F. Zhang, Intranasal Delivery of Granulocyte Colony-Stimulating Factor Enhances Its Neuroprotective Effects Against Ischemic Brain Injury in Rats, Mol Neurobiol, 53 (2016) 320-330.

[176] Y.P. Yu, Q.Q. Xu, Q. Zhang, W.P. Zhang, L.H. Zhang, E.Q. Wei, Intranasal recombinant human erythropoietin protects rats against focal cerebral ischemia, Neurosci Lett, 387 (2005) 5-10.

[177] Q. Lv, X. Fan, G. Xu, Q. Liu, L. Tian, X. Cai, W. Sun, X. Wang, Q. Cai, Y. Bao, L. Zhou, Y. Zhang, L. Ge, R. Guo, X. Liu, Intranasal delivery of nerve growth factor attenuates aquaporins-4-induced edema following traumatic brain injury in rats, Brain Res, 1493 (2013) 80-89.

[178] B.C. Topkoru, O. Altay, K. Duris, P.R. Krafft, J. Yan, J.H. Zhang, Nasal administration of recombinant osteopontin attenuates early brain injury after subarachnoid hemorrhage, Stroke, 44 (2013) 3189-3194.

[179] S.M. Hearst, Q. Shao, M. Lopez, D. Raucher, P.J. Vig, The design and delivery of a PKA inhibitory polypeptide to treat SCA1, Journal of neurochemistry, 131 (2014) 101-114.

[180] J.R. Thornton-Manning, A.R. Dahl, Metabolic capacity of nasal tissue interspecies comparisons of xenobiotic-metabolizing enzymes, Mutat Res, 380 (1997) 43-59.

[181] M.A. Reger, G.S. Watson, P.S. Green, L.D. Baker, B. Cholerton, M.A. Fishel, S.R. Plymate, M.M. Cherrier, G.D. Schellenberg, W.H. Frey, 2nd, S. Craft, Intranasal insulin administration dose-dependently modulates verbal memory and plasma amyloid-beta in memory-impaired older adults, J Alzheimers Dis, 13 (2008) 323-331.

[182] C. Benedict, M. Hallschmid, A. Hatke, B. Schultes, H.L. Fehm, J. Born, W. Kern, Intranasal insulin improves memory in humans, Psychoneuroendocrinology, 29 (2004) 1326-1334.

[183] C. Benedict, M. Hallschmid, K. Schmitz, B. Schultes, F. Ratter, H.L. Fehm, J. Born, W. Kern, Intranasal insulin improves memory in humans: superiority of insulin aspart, Neuropsychopharmacology, 32 (2007) 239-243.

[184] W. Kern, J. Born, H. Schreiber, H.L. Fehm, Central nervous system effects of intranasally administered insulin during euglycemia in men, Diabetes, 48 (1999) 557-563.

[185] C. Schulz, K. Paulus, O. Johren, H. Lehnert, Intranasal leptin reduces appetite and induces weight loss in rats with diet-induced obesity (DIO), Endocrinology, 153 (2012) 143-153.

[186] W.A. Banks, C.R. Lebel, Strategies for the delivery of leptin to the CNS, J Drug Target, 10 (2002) 297-308.

[187] M.J. Kubek, A.J. Domb, M.C. Veronesi, Attenuation of kindled seizures by intranasal delivery of neuropeptide-loaded nanoparticles, Neurotherapeutics, 6 (2009) 359-371.

[188] X. Zhang, L. Liu, G. Chai, X. Zhang, F. Li, Brain pharmacokinetics of neurotoxin-loaded PLA nanoparticles modified with chitosan after intranasal administration in awake rats, Drug Dev Ind Pharm, 39 (2013) 1618-1624.

[189] X. Gao, B. Wu, Q. Zhang, J. Chen, J. Zhu, W. Zhang, Z. Rong, H. Chen, X. Jiang, Brain delivery of vasoactive intestinal peptide enhanced with the nanoparticles conjugated with wheat germ agglutinin following intranasal administration, J Control Release, 121 (2007) 156-167.

[190] A.P. Appu, P. Arun, J.K. Krishnan, J.R. Moffett, A.M. Namboodiri, Rapid intranasal delivery of chloramphenicol acetyltransferase in the active form to different brain regions as a model for enzyme therapy in the CNS, J Neurosci Methods, 259 (2016) 129-134.

[191] D. Hackel, S.M. Krug, R.S. Sauer, S.A. Mousa, A. Bocker, D. Pflucke, E.J. Wrede, K. Kistner, T. Hoffmann, B. Niedermirtl, C. Sommer, L. Bloch, O. Huber, I.E. Blasig, S. Amasheh, P.W. Reeh, M. Fromm, A. Brack, H.L. Rittner, Transient opening of the perineurial barrier for analgesic drug delivery, Proc Natl Acad Sci U S A, 109 (2012) E2018-2027.

[192] H.R. Costantino, L. Illum, G. Brandt, P.H. Johnson, S.C. Quay, Intranasal delivery: physicochemical and therapeutic aspects, Int J Pharm, 337 (2007) 1-24.

[193] L. Kozlovskaya, M. Abou-Kaoud, D. Stepensky, Quantitative analysis of drug delivery to the brain via nasal route, J Control Release, 189 (2014) 133-140.

[194] T. Lin, E. Liu, H. He, M.C. Shin, C. Moon, V.C. Yang, Y. Huang, Nose-to-brain delivery of macromolecules mediated by cell-penetrating peptides, Acta Pharm Sin B, 6 (2016) 352-358.

[195] J. Xu, Q. Xiang, J. Su, P. Yang, Q. Zhang, Z. Su, F. Xiao, Y. Huang, Evaluation of the safety and brain-related tissues distribution characteristics of TAT-HaFGF via intranasal administration, Biol Pharm Bull, 37 (2014) 1149-1157.

[196] N. Kamei, M. Takeda-Morishita, Brain delivery of insulin boosted by intranasal coadministration with cell-penetrating peptides, J Control Release, 197 (2015) 105-110.

[197] S. Sasaki-Hamada, R. Nakamura, Y. Nakao, T. Akimoto, E. Sanai, M. Nagai, M. Horiguchi, C. Yamashita, J.I. Oka, Antidepressant-like effects exerted by the intranasal administration of a glucagon-like peptide-2 derivative containing cell-penetrating peptides and a penetration-accelerating sequence in mice, Peptides, 87 (2016) 64-70.

[198] N. Kamei, T. Shingaki, Y. Kanayama, M. Tanaka, R. Zochi, K. Hasegawa, Y. Watanabe, M. Takeda-Morishita, Visualization and Quantitative Assessment of the Brain Distribution of Insulin through Nose-to-Brain Delivery Based on the Cell-Penetrating Peptide Noncovalent Strategy, Mol Pharm, 13 (2016) 1004-1011.

[199] N. Kamei, M. Morishita, K. Takayama, Importance of intermolecular interaction on the improvement of intestinal therapeutic peptide/protein absorption using cell-penetrating peptides, J Control Release, 136 (2009) 179-186.

[200] S. Khafagy el, N. Kamei, E.J. Nielsen, R. Nishio, M. Takeda-Morishita, One-month subchronic toxicity study of cell-penetrating peptides for insulin nasal delivery in rats, Eur J Pharm Biopharm, 85 (2013) 736-743.

[201] V.D. Romeo, J.C. deMeireles, W.J. Gries, W.J. Xia, A.P. Sileno, H.K. Pimplaskar, C.R. Behl, Optimization of systemic nasal drug delivery with pharmaceutical excipients, Adv Drug Deliv Rev, 29 (1998) 117-133.

[202] S. Khafagy el, M. Morishita, N. Kamei, Y. Eda, Y. Ikeno, K. Takayama, Efficiency of cell-penetrating peptides on the nasal and intestinal absorption of therapeutic peptides and proteins, Int J Pharm, 381 (2009) 49-55.

[203] H. Shimizu, I.S. Oh, S. Okada, M. Mori, Inhibition of appetite by nasal leptin administration in rats, Int J Obes (Lond), 29 (2005) 858-863.

[204] S.V. Dhuria, L.R. Hanson, W.H. Frey, 2nd, Novel vasoconstrictor formulation to enhance intranasal targeting of neuropeptide therapeutics to the central nervous system, J Pharmacol Exp Ther, 328 (2009) 312-320.

[205] J.A. Falcone, T.S. Salameh, X. Yi, B.J. Cordy, W.G. Mortell, A.V. Kabanov, W.A. Banks, Intranasal administration as a route for drug delivery to the brain: evidence for a unique pathway for albumin, J Pharmacol Exp Ther, 351 (2014) 54-60.

[206] N. Nonaka, S.A. Farr, T. Nakamachi, J.E. Morley, M. Nakamura, S. Shioda, W.A. Banks, Intranasal administration of PACAP: uptake by brain and regional brain targeting with cyclodextrins, Peptides, 36 (2012) 168-175.

[207] N. Nonaka, S.A. Farr, H. Kageyama, S. Shioda, W.A. Banks, Delivery of galanin-like peptide to the brain: targeting with intranasal delivery and cyclodextrins, J Pharmacol Exp Ther, 325 (2008) 513-519.

[208] A. Fortuna, G. Alves, A. Serralheiro, J. Sousa, A. Falcao, Intranasal delivery of systemic-acting drugs: small-molecules and biomacromolecules, Eur J Pharm Biopharm, 88 (2014) 8-27.

[209] D. Yang, Y.Y. Sun, X. Lin, J.M. Baumann, M. Warnock, D.A. Lawrence, C.Y. Kuan, Taming neonatal hypoxic-ischemic brain injury by intranasal delivery of plasminogen activator inhibitor-1, Stroke, 44 (2013) 2623-2627.

[210] S.T. Charlton, S.S. Davis, L. Illum, Nasal administration of an angiotensin antagonist in the rat model: effect of bioadhesive formulations on the distribution of drugs to the systemic and central nervous systems, Int J Pharm, 338 (2007) 94-103.

[211] M.P. van den Berg, S.G. Romeijn, J.C. Verhoef, F.W. Merkus, Serial cerebrospinal fluid sampling in a rat model to study drug uptake from the nasal cavity, J Neurosci Methods, 116 (2002) 99-107.

[212] H. Wu, K. Hu, X. Jiang, From nose to brain: understanding transport capacity and transport rate of drugs, Expert Opin Drug Deliv, 5 (2008) 1159-1168.

[213] S.H. Mayor, L. Illum, Investigation of the effect of anaesthesia on nasal absorption of insulin in rats, International Journal of Pharmaceutics, 149 (1997) 123-129.

[214] S. Wharton, Current Perspectives on Long-term Obesity Pharmacotherapy, Can J Diabetes, 40 (2016) 184-191.

[215] D. Wong, K. Sullivan, G. Heap, The pharmaceutical market for obesity therapies, Nat Rev Drug Discov, 11 (2012) 669-670.

[216] W. Rankin, G. Wittert, Anti-obesity drugs, Curr Opin Lipidol, 26 (2015) 536-543.

[217] F. Colon-Gonzalez, G.W. Kim, J.E. Lin, M.A. Valentino, S.A. Waldman, Obesity pharmacotherapy: what is next?, Molecular aspects of medicine, 34 (2013) 71-83.

[218] E. Ravussin, S.R. Smith, J.A. Mitchell, R. Shringarpure, K. Shan, H. Maier, J.E. Koda, C. Weyer, Enhanced weight loss with pramlintide/metreleptin: an integrated neurohormonal approach to obesity pharmacotherapy, Obesity (Silver Spring), 17 (2009) 1736-1743.

[219] J.D. Roth, B.L. Roland, R.L. Cole, J.L. Trevaskis, C. Weyer, J.E. Koda, C.M. Anderson, D.G. Parkes, A.D. Baron, Leptin responsiveness restored by amylin agonism in diet-induced obesity: evidence from nonclinical and clinical studies, Proc Natl Acad Sci U S A, 105 (2008) 7257-7262.

[220] N. Sainz, J. Barrenetxe, M.J. Moreno-Aliaga, J.A. Martinez, Leptin resistance and diet-induced obesity: central and peripheral actions of leptin, Metabolism, 64 (2015) 35-46.

[221] R.S. Ahima, S.Y. Osei, Leptin signaling, Physiology & behavior, 81 (2004) 223-241.

[222] H. Munzberg, C.D. Morrison, Structure, production and signaling of leptin, Metabolism, 64 (2015) 13-23.

[223] A.M. DePaoli, 20 years of leptin: leptin in common obesity and associated disorders of metabolism, J Endocrinol, 223 (2014) T71-81.

[224] C.S. Mantzoros, J.S. Flier, Editorial: leptin as a therapeutic agent--trials and tribulations, The Journal of clinical endocrinology and metabolism, 85 (2000) 4000-4002.

[225] M.W. Schwartz, S.C. Woods, D. Porte, Jr., R.J. Seeley, D.G. Baskin, Central nervous system control of food intake, Nature, 404 (2000) 661-671.

[226] B.E. Levin, A.A. Dunn-Meynell, W.A. Banks, Obesity-prone rats have normal blood-brain barrier transport but defective central leptin signaling before obesity onset, American journal of physiology. Regulatory, integrative and comparative physiology, 286 (2004) R143-150.

[227] X.S. Wu-Peng, S.C. Chua, Jr., N. Okada, S.M. Liu, M. Nicolson, R.L. Leibel, Phenotype of the obese Koletsky (f) rat due to Tyr763Stop mutation in the extracellular domain of the leptin

receptor (Lepr): evidence for deficient plasma-to-CSF transport of leptin in both the Zucker and Koletsky obese rat, Diabetes, 46 (1997) 513-518.

[228] W.A. Banks, Is obesity a disease of the blood-brain barrier? Physiological, pathological, and evolutionary considerations, Current pharmaceutical design, 9 (2003) 801-809.

[229] M. Van Heek, D.S. Compton, C.F. France, R.P. Tedesco, A.B. Fawzi, M.P. Graziano, E.J. Sybertz, C.D. Strader, H.R. Davis, Jr., Diet-induced obese mice develop peripheral, but not central, resistance to leptin, The Journal of clinical investigation, 99 (1997) 385-390.

[230] J.L. Halaas, C. Boozer, J. Blair-West, N. Fidahusein, D.A. Denton, J.M. Friedman, Physiological response to long-term peripheral and central leptin infusion in lean and obese mice, Proc Natl Acad Sci U S A, 94 (1997) 8878-8883.

[231] S.B. Heymsfield, A.S. Greenberg, K. Fujioka, R.M. Dixon, R. Kushner, T. Hunt, J.A. Lubina, J. Patane, B. Self, P. Hunt, M. McCamish, Recombinant leptin for weight loss in obese and lean adults: a randomized, controlled, dose-escalation trial, JAMA : the journal of the American Medical Association, 282 (1999) 1568-1575.

[232] A. Kahler, N. Geary, L.A. Eckel, L.A. Campfield, F.J. Smith, W. Langhans, Chronic administration of OB protein decreases food intake by selectively reducing meal size in male rats, The American journal of physiology, 275 (1998) R180-185.

[233] I. Kovalszky, E. Surmacz, L. Scolaro, M. Cassone, R. Ferla, A. Sztodola, J. Olah, M.P. Hatfield, S. Lovas, L. Otvos, Jr., Leptin-based glycopeptide induces weight loss and simultaneously restores fertility in animal models, Diabetes, obesity & metabolism, 12 (2010) 393-402.

[234] W.A. Banks, C.L. Farrell, Impaired transport of leptin across the blood-brain barrier in obesity is acquired and reversible, American journal of physiology. Endocrinology and metabolism, 285 (2003) E10-15.

[235] The Practical Guide: Identification, Evaluation, and Treatment of Overweight and Obesity in Adults. 00-4084. , in: L. American Association for the Study of Obesity (NAASO) and the National Heart, and Blood Institute (NHLBI). (Ed.), October 2000.

[236] T.O. Price, S.A. Farr, X. Yi, S. Vinogradov, E. Batrakova, W.A. Banks, A.V. Kabanov, Transport across the blood-brain barrier of pluronic leptin, J Pharmacol Exp Ther, 333 (2010) 253-263.

[237] X. Yi, E. Batrakova, W.A. Banks, S. Vinogradov, A.V. Kabanov, Protein conjugation with amphiphilic block copolymers for enhanced cellular delivery, Bioconjug Chem, 19 (2008) 1071-1077.

[238] J.I. MacDonald, H.K. Munch, T. Moore, M.B. Francis, One-step site-specific modification of native proteins with 2-pyridinecarboxyaldehydes, Nat Chem Biol, 11 (2015) 326-331.

[239] J. Tong, X. Yi, R. Luxenhofer, W.A. Banks, R. Jordan, M.C. Zimmerman, A.V. Kabanov, Conjugates of superoxide dismutase 1 with amphiphilic poly(2-oxazoline) block copolymers for enhanced brain delivery: synthesis, characterization and evaluation in vitro and in vivo, Mol Pharm, 10 (2013) 360-377.

[240] D.H.A. Corrêa, C.H.I. Ramos, The use of circular dichroism spectroscopy to study protein folding, form and function, African Journal of Biochemistry Research, 3 (2009) 164-173.

[241] L. Whitmore, B.A. Wallace, Protein secondary structure analyses from circular dichroism spectroscopy: methods and reference databases, Biopolymers, 89 (2008) 392-400.

[242] L. Whitmore, B.A. Wallace, DICHROWEB, an online server for protein secondary structure analyses from circular dichroism spectroscopic data, Nucleic acids research, 32 (2004) W668-673.

[243] P. Mistrik, F. Moreau, J.M. Allen, BiaCore analysis of leptin-leptin receptor interaction: evidence for 1:1 stoichiometry, Anal Biochem, 327 (2004) 271-277.

[244] J. Glowinski, L.L. Iversen, Regional studies of catecholamines in the rat brain. I. The disposition of [3H]norepinephrine, [3H]dopamine and [3H]dopa in various regions of the brain, Journal of neurochemistry, 13 (1966) 655-669.

[245] W.A. Banks, A.J. Kastin, W. Huang, J.B. Jaspan, L.M. Maness, Leptin enters the brain by a saturable system independent of insulin, Peptides, 17 (1996) 305-311.

[246] C.S. Patlak, R.G. Blasberg, J.D. Fenstermacher, Graphical evaluation of blood-to-brain transfer constants from multiple-time uptake data, J Cereb Blood Flow Metab, 3 (1983) 1-7.

[247] S. Fliedner, C. Schulz, H. Lehnert, Brain uptake of intranasally applied radioiodinated leptin in Wistar rats, Endocrinology, 147 (2006) 2088-2094.

[248] Z. Zhou, J. Zhang, L. Sun, G. Ma, Z. Su, Comparison of site-specific PEGylations of the N-terminus of interferon beta-1b: selectivity, efficiency, and in vivo/vitro activity, Bioconjug Chem, 25 (2014) 138-146.

[249] C. Zheng, G. Ma, Z. Su, Native PAGE eliminates the problem of PEG-SDS interaction in SDS-PAGE and provides an alternative to HPLC in characterization of protein PEGylation, Electrophoresis, 28 (2007) 2801-2807.

[250] K. Mortensen, W. Batsberg, S. Hvidt, Effects of PEO−PPO Diblock Impurities on the Cubic Structure of Aqueous PEO−PPO−PEO Pluronics Micelles: fcc and bcc Ordered Structures in F127, Macromolecules, 41 (2008) 1720-1727.

[251] L.M. Churgay, S. Kovacevic, F.C. Tinsley, C.M. Kussow, R.L. Millican, J.R. Miller, J.E. Hale, Purification and characterization of secreted human leptin produced in baculovirus-infected insect cells, Gene, 190 (1997) 131-137.

[252] L. Niv-Spector, D. Gonen-Berger, I. Gourdou, E. Biener, E.E. Gussakovsky, Y. Benomar, K.V. Ramanujan, M. Taouis, B. Herman, I. Callebaut, J. Djiane, A. Gertler, Identification of the hydrophobic strand in the A-B loop of leptin as major binding site III: implications for large-scale preparation of potent recombinant human and ovine leptin antagonists, Biochem J, 391 (2005) 221-230.

[253] S.M. Kelly, T.J. Jess, N.C. Price, How to study proteins by circular dichroism, Biochim Biophys Acta, 1751 (2005) 119-139.

[254] B. Bharatiya, V.K. Aswal, P.A. Hassan, P. Bahadur, Influence of a hydrophobic diol on the micellar transitions of Pluronic P85 in aqueous solution, J Colloid Interface Sci, 320 (2008) 452-459.

[255] D.L. Morris, L. Rui, Recent advances in understanding leptin signaling and leptin resistance, American journal of physiology. Endocrinology and metabolism, 297 (2009) E1247-1259.

[256] M. Faouzi, R. Leshan, M. Bjornholm, T. Hennessey, J. Jones, H. Munzberg, Differential accessibility of circulating leptin to individual hypothalamic sites, Endocrinology, 148 (2007) 5414-5423.

[257] L.M. Maness, A.J. Kastin, C.L. Farrell, W.A. Banks, Fate of leptin after intracerebroventricular injection into the mouse brain, Endocrinology, 139 (1998) 4556-4562.

[258] W.A. Banks, M.L. Niehoff, D. Martin, C.L. Farrell, Leptin transport across the blood-brain barrier of the Koletsky rat is not mediated by a product of the leptin receptor gene, Brain Res, 950 (2002) 130-136.

[259] H.H. Zhang, S. Kumar, A.H. Barnett, M.C. Eggo, Intrinsic site-specific differences in the expression of leptin in human adipocytes and its autocrine effects on glucose uptake, The Journal of clinical endocrinology and metabolism, 84 (1999) 2550-2556.

[260] F. Peelman, K. Van Beneden, L. Zabeau, H. Iserentant, P. Ulrichts, D. Defeau, A. Verhee, D. Catteeuw, D. Elewaut, J. Tavernier, Mapping of the leptin binding sites and design of a leptin antagonist, J Biol Chem, 279 (2004) 41038-41046.

[261] C.J. Hukshorn, W.H. Saris, M.S. Westerterp-Plantenga, A.R. Farid, F.J. Smith, L.A. Campfield, Weekly subcutaneous pegylated recombinant native human leptin (PEG-OB) administration in obese men, The Journal of clinical endocrinology and metabolism, 85 (2000) 4003-4009.

[262] L. Xu, N. Rensing, X.F. Yang, H.X. Zhang, L.L. Thio, S.M. Rothman, A.E. Weisenfeld, M. Wong, K.A. Yamada, Leptin inhibits 4-aminopyridine- and pentylenetetrazole-induced seizures and AMPAR-mediated synaptic transmission in rodents, The Journal of clinical investigation, 118 (2008) 272-280.

[263] C. Schulz, K. Paulus, H. Lehnert, Central nervous and metabolic effects of intranasally applied leptin, Endocrinology, 145 (2004) 2696-2701.

[264] H.R. Kissileff, J.C. Thornton, M.I. Torres, K. Pavlovich, L.S. Mayer, V. Kalari, R.L. Leibel, M. Rosenbaum, Leptin reverses declines in satiation in weight-reduced obese humans, The American journal of clinical nutrition, 95 (2012) 309-317.

[265] X. Yi, M.C. Zimmerman, R. Yang, J. Tong, S. Vinogradov, A.V. Kabanov, Pluronic-modified superoxide dismutase 1 attenuates angiotensin II-induced increase in intracellular superoxide in neurons, Free radical biology & medicine, 49 (2010) 548-558.

[266] J. Harvey, Leptin regulation of neuronal morphology and hippocampal synaptic function, Front Synaptic Neurosci, 5 (2013) 3.

[267] A.A. Miller, S.J. Spencer, Obesity and neuroinflammation: a pathway to cognitive impairment, Brain Behav Immun, 42 (2014) 10-21.

[268] G. Marwarha, O. Ghribi, Leptin signaling and Alzheimer's disease, Am J Neurodegener Dis, 1 (2012) 245-265.

[269] J. Taildeman, P. Demetter, I. Rottiers, G. Holtappels, C. Bachert, C.A. Cuvelier, C.A. Perez-Novo, Identification of the nasal mucosa as a new target for leptin action, Histopathology, 56 (2010) 789-798.

[270] S.Y. Song, H.J. Woo, C.H. Bae, Y.W. Kim, Y.D. Kim, Expression of leptin receptor in nasal polyps: leptin as a mucosecretagogue, Laryngoscope, 120 (2010) 1046-1050.

[271] A. Bruno, S. Gerbino, M. Ferraro, L. Siena, A. Bonura, P. Colombo, S. La Grutta, S. Gallina, A. Ballacchino, M. Giammanco, M. Gjomarkaj, E. Pace, Fluticasone furoate maintains epithelial homeostasis via leptin/leptin receptor pathway in nasal cells, Mol Cell Biochem, 396 (2014) 55-65.

[272] C. Baly, J. Aioun, K. Badonnel, M.C. Lacroix, D. Durieux, C. Schlegel, R. Salesse, M. Caillol, Leptin and its receptors are present in the rat olfactory mucosa and modulated by the nutritional status, Brain Res, 1129 (2007) 130-141.

[273] E.V. Batrakova, A.V. Kabanov, Pluronic block copolymers: evolution of drug delivery concept from inert nanocarriers to biological response modifiers, J Control Release, 130 (2008) 98-106.

[274] S.M. de la Monte, Intranasal insulin therapy for cognitive impairment and neurodegeneration: current state of the art, Expert Opin Drug Deliv, 10 (2013) 1699-1709.

[275] M.J. Haney, N.L. Klyachko, Y.L. Zhaoa, R. Gupta, E.G. Plotnikova, Z.J. He, T. Patel, A. Piroyan, M. Sokolsky, A.V. Kabanov, E.V. Batrakova, Exosomes as drug delivery vehicles for Parkinson's disease therapy, Journal of Controlled Release, 207 (2015) 18-30.

[276] P.G. Djupesland, Nasal drug delivery devices: characteristics and performance in a clinical perspective-a review, Drug Deliv Transl Res, 3 (2013) 42-62.

[277] P.D. Robbins, A.E. Morelli, Regulation of immune responses by extracellular vesicles, Nat Rev Immunol, 14 (2014) 195-208.

[278] C. Thery, L. Zitvogel, S. Amigorena, Exosomes: composition, biogenesis and function, Nat Rev Immunol, 2 (2002) 569-579.

[279] B. Obermeier, R. Daneman, R.M. Ransohoff, Development, maintenance and disruption of the blood-brain barrier, Nat Med, 19 (2013) 1584-1596.

[280] C. Shi, E.G. Pamer, Monocyte recruitment during infection and inflammation, Nat Rev Immunol, 11 (2011) 762-774.

[281] A. Gupta, L. Pulliam, Exosomes as mediators of neuroinflammation, Journal of Neuroinflammation, 11 (2014) 68.

[282] C. Thery, S. Amigorena, G. Raposo, A. Clayton, Isolation and characterization of exosomes from cell culture supernatants and biological fluids, Current protocols in cell biology / editorial board, Juan S. Bonifacino ... [et al.], Chapter 3 (2006) Unit 3 22.

[283] C.A. Schneider, W.S. Rasband, K.W. Eliceiri, NIH Image to ImageJ: 25 years of image analysis, Nature methods, 9 (2012) 671-675.

[284] S. Bolte, F.P. Cordelieres, A guided tour into subcellular colocalization analysis in light microscopy, J Microsc-Oxford, 224 (2006) 213-232.

[285] W.A. Banks, S.M. Robinson, Minimal penetration of lipopolysaccharide across the murine blood-brain barrier, Brain Behav Immun, 24 (2010) 102-109.

[286] P.P. Singh, V.L. Smith, P.C. Karakousis, J.S. Schorey, Exosomes isolated from mycobacteria-infected mice or cultured macrophages can recruit and activate immune cells in vitro and in vivo, J Immunol, 189 (2012) 777-785.

[287] C.L. Chen, W.H. Hou, I.H. Liu, G. Hsiao, S.S. Huang, J.S. Huang, Inhibitors of clathrin-dependent endocytosis enhance TGFbeta signaling and responses, J Cell Sci, 122 (2009) 1863-1871.

[288] D. Feng, W.L. Zhao, Y.Y. Ye, X.C. Bai, R.Q. Liu, L.F. Chang, Q. Zhou, S.F. Sui, Cellular Internalization of Exosomes Occurs Through Phagocytosis, Traffic, 11 (2010) 675-687.

[289] S. Guo, X. Zhang, M. Zheng, X. Zhang, C. Min, Z. Wang, S.H. Cheon, M.H. Oak, S.Y. Nah, K.M. Kim, Selectivity of commonly used inhibitors of clathrin-mediated and caveolae-dependent endocytosis of G protein-coupled receptors, Biochim Biophys Acta, 1848 (2015) 2101-2110.

[290] D. Dutta, J.G. Donaldson, Search for inhibitors of endocytosis: Intended specificity and unintended consequences, Cell Logist, 2 (2012) 203-208.

[291] L.A. Mulcahy, R.C. Pink, D.R. Carter, Routes and mechanisms of extracellular vesicle uptake, J Extracell Vesicles, 3 (2014).

[292] H.C. Christianson, K.J. Svensson, T.H. van Kuppevelt, J.P. Li, M. Belting, Cancer cell exosomes depend on cell-surface heparan sulfate proteoglycans for their internalization and functional activity, Proc Natl Acad Sci U S A, 110 (2013) 17380-17385.

[293] J. Li, L. Ye, X. Wang, J. Liu, Y. Wang, Y. Zhou, W. Ho, (-)-Epigallocatechin gallate inhibits endotoxin-induced expression of inflammatory cytokines in human cerebral microvascular endothelial cells, J Neuroinflammation, 9 (2012) 161.

[294] S. Hao, O. Bai, F. Li, J. Yuan, S. Laferte, J. Xiang, Mature dendritic cells pulsed with exosomes stimulate efficient cytotoxic T-lymphocyte responses and antitumour immunity, Immunology, 120 (2007) 90-102.

[295] J.A. Oka, M.D. Christensen, P.H. Weigel, Hyperosmolarity inhibits galactosyl receptor-mediated but not fluid phase endocytosis in isolated rat hepatocytes, J Biol Chem, 264 (1989) 12016-12024.

[296] L. Zou, S. Yang, V. Champattanachai, S. Hu, I.H. Chaudry, R.B. Marchase, J.C. Chatham, Glucosamine improves cardiac function following trauma-hemorrhage by increased protein O-GlcNAcylation and attenuation of NF-{kappa}B signaling, American journal of physiology. Heart and circulatory physiology, 296 (2009) H515-523.

[297] C.L. Chen, C.M. Liang, Y.H. Chen, M.C. Tai, D.W. Lu, J.T. Chen, Glucosamine modulates TNF-alpha-induced ICAM-1 expression and function through O-linked and N-linked glycosylation in human retinal pigment epithelial cells, Investigative ophthalmology & visual science, 53 (2012) 2281-2291.

[298] W.A. Banks, M.L. Niehoff, N.M. Ponzio, M.A. Erickson, S.S. Zalcman, Pharmacokinetics and modeling of immune cell trafficking: quantifying differential influences of target tissues versus lymphocytes in SJL and lipopolysaccharide-treated mice, J Neuroinflammation, 9 (2012) 231.

[299] D.A. Hume, The mononuclear phagocyte system, Curr Opin Immunol, 18 (2006) 49-53.

[300] T. Shinoda, A. Takagi, A. Maeda, S. Kagatani, Y. Konno, M. Hashida, In vivo fate of folate-BSA in non-tumor- and tumor-bearing mice, J Pharm Sci, 87 (1998) 1521-1526.

[301] Y. Zhao, M.J. Haney, V. Mahajan, B.C. Reiner, A. Dunaevsky, R.L. Mosley, A.V. Kabanov, H.E. Gendelman, E.V. Batrakova, Active Targeted Macrophage-mediated Delivery of Catalase to Affected Brain Regions in Models of Parkinson's Disease, J Nanomed Nanotechnol, S4 (2011).

[302] A.M. Dickens, S. Vainio, P. Marjamaki, J. Johansson, P. Lehtiniemi, J. Rokka, J. Rinne, O. Solin, M. Haaparanta-Solin, P.A. Jones, W. Trigg, D.C. Anthony, L. Airas, Detection of microglial activation in an acute model of neuroinflammation using PET and radiotracers 11C-(R)-PK11195 and 18F-GE-180, J Nucl Med, 55 (2014) 466-472.

[303] H. Zhou, B.M. Lapointe, S.R. Clark, L. Zbytnuik, P. Kubes, A requirement for microglial TLR4 in leukocyte recruitment into brain in response to lipopolysaccharide, J Immunol, 177 (2006) 8103-8110.

[304] S.L. Patterson, T. Abel, T.A. Deuel, K.C. Martin, J.C. Rose, E.R. Kandel, Recombinant BDNF rescues deficits in basal synaptic transmission and hippocampal LTP in BDNF knockout mice, Neuron, 16 (1996) 1137-1145.

[305] Y. Kanato, K. Kitajima, C. Sato, Direct binding of polysialic acid to a brain-derived neurotrophic factor depends on the degree of polymerization, Glycobiology, 18 (2008) 1044-1053.

[306] Y. Kanato, S. Ono, K. Kitajima, C. Sato, Complex formation of a brain-derived neurotrophic factor and glycosaminoglycans, Biosci Biotechnol Biochem, 73 (2009) 2735-2741.

[307] C.C. Chen, L. Liu, F. Ma, C.W. Wong, X.E. Guo, J.V. Chacko, H.P. Farhoodi, S.X. Zhang, J. Zimak, A. Segaliny, M. Riazifar, V. Pham, M.A. Digman, E.J. Pone, W. Zhao, Elucidation of Exosome Migration across the Blood-Brain Barrier Model In Vitro, Cell Mol Bioeng, 9 (2016) 509-529.

[308] G.J. Casimir, J. Duchateau, Gender differences in inflammatory processes could explain poorer prognosis for males, J Clin Microbiol, 49 (2011) 478; author reply 478-479.

[309] C.A. Maguire, M.H. Crommentuijn, D. Mu, E. Hudry, A. Serrano-Pozo, B.T. Hyman, B.A. Tannous, Mouse gender influences brain transduction by intravascularly administered AAV9, Mol Ther, 21 (2013) 1470-1471.

[310] S.B. Weisser, N. van Rooijen, L.M. Sly, Depletion and reconstitution of macrophages in mice, J Vis Exp, (2012) 4105.